Modeling and simulation of the initial state of a thermoplastic matrix composite structure manufactured by laser assisted tape placement

Livio Di Gennaro

université
PARIS-SACLAY

Modeling and simulation of the initial state of a thermoplastic matrix composite structure manufactured by laser assisted tape placement

Modélisation et simulation de l'état initial d'une structure en composite à matrice thermoplastique fabriquée par placement de tape automatisé et consolidation laser

Thèse de doctorat de l'université Paris-Saclay

École doctorale n°579 : sciences mécaniques et énergétiques, matériaux et géosciences (SMEMaG)
Spécialité de doctorat: Mécanique des matériaux
Graduate School : Sciences de l'ingénierie et des systèmes, Référent : ENS Paris-Saclay

Thèse préparée dans l'unité de recherche **LMPS - Laboratoire de Mécanique Paris-Saclay** (Université Paris-Saclay, CentraleSupélec, ENS Paris-Saclay, CNRS) sous la direction de Federica DAGHIA, directrice de thèse, la co-direction de Frédéric JACQUEMIN, co-directeur de thèse et le co-encadrement de Christophe CLUZEL.

Thèse soutenue à Paris-Saclay, le 6 mai 2022, par

Livio DI GENNARO

Composition du jury

Xiaojing Gong Professeure des Universités, Institut Universitaire de Technologie de Tarbes, ICA	Présidente
Christophe Bois Professeur des Universités, Université de Bordeaux, I2M	Rapporteur
Damien Halm Professeur des Universités, Ecole Nationale Supérieure de Mécanique et d'Aérotechnique, PPrime	Rapporteur
Federica Daghia Maître de Conférences HDR, ENS Paris-Saclay, LMPS	Directrice de thèse

THESE DE DOCTORAT

NNT : 2022UPAST055

This work is dedicated to my girlfriend Alisia.

If you want to understand it,
write it down.

Acknowledgements

Those who, like me, have completed or are completing their PhD at this time certainly worked during the dark period of the Covid pandemic.

The PhD, despite any collaborations with other people or institutions, by its nature, is a personal endeavor. For this reason, the PhD during the Covid was undoubtedly an extraordinary experience but, above all, a difficult one. The two years of quarantine exacerbated its characteristics by making the work solitary, selfish, and almost an end in itself. Video-calls have been the primary communication tool during the quarantine period since in person was impossible. Scientific and technical exchanges with supervisors and other doctoral students occurred in this manner. Almost all scientific conferences were cancelled or turned into video-conferences reducing the possibility of meeting people drastically and making the scientific exchange extremely cold.

Not to mention the pleasure calls with friends/colleagues, relatives and girlfriend/boyfriend that always took place via video-call among the thousands of technical problems of audio, video, internet or simply the difficulties encountered by the interlocutor not being accustomed to technology (I refer especially to relatives of course). I met my girlfriend Alisia just before the covid came, and I'm not going to talk about all the difficulties and problems related to a long-distance relationship during the covid...

Anyway, putting one of my mother's teachings into practice, I want to emphasize the positive aspects of this complex challenge. One of them is that what I am writing now is the last thing I will write about my doctoral thesis because, after these acknowledgements, my work will be complete. I am incredibly proud and satisfied with the work I have achieved, not only because of the content but also because, as someone said, "The harder the battle, the sweeter the victory." In addition, during this chapter of my life, I have had the opportunity to meet and get to know many fantastic and exceptional people with whom I have shared experiences and who have taught me a lot of things. For these reasons, I want to thank them.

I achieved this work in collaboration and under the supervision of Federica Daghia, Christophe Cluzel, Frederic Jacquemin, and Denis Espinassou, and for this I sincerely thank them. A special thanks go to my thesis director Federica Daghia who followed me from the first day of work and trained me on specific knowledge and all the different aspects that characterized the PhD, i.e., presentations and writing scientific papers, to name a few. The advice, suggestions, and teachings that Federica gave me day by day were the reasons for my significant progress made in these three years and why I am proud of the PhD work

we did.

Aya, Pascale, Ariane, and Sebastian, my friends, and colleagues at the University. Thank you!!! We shared a lot, especially before and after Covid. The scientific exchanges with Sebastian, the laughs with Aya and Pascale, and Ariane talking all the time. I thank you so much also because with you I learned to speak French and for this I was fortunate to meet you. A special thanks to Ariane, the most selfless, generous, and helpful person I have ever met. Keep up the excellent work and never change.

Thanks to my friend Serena especially for the regular appointment with the daily voice messages in the morning. She is always available and ready to help and, above all, very empathetic and sensitive. I should learn more from you. With Serena, we have known each other since before PhD, and we have shared a lot, and I hope we will continue to do so after my PhD

I want to thank my friend, Ph.D. Daniel Andres Odens Mora Paiba (lol). He has been my roommate for a year, with whom I have shared many Friday and Saturday nights at home in quarantine. Andres takes every minute of his life to do something productive, and because of that, he has been a great motivator while living with me, especially during the darkest periods of my PhD. Thank you.

Thanks also to my brother and my family, who have always been present and ready to support me even from a distance. It was also complicated for them because they couldn't help me and share this experience in the first person. In any case, they did a great job.

The person I will be grateful to all my life is my girlfriend, Alisia. She has always been supportive and put up with me throughout my PhD. She has always been a great source of inspiration and motivation and has always been there in all the most difficult moments to push me through and help me overcome them. Meeting her just before the pandemic (under particular circumstances that I won't tell you about) was a bit unfortunate because we spent most of our relationship at a distance. However, only thanks to her I overcome these difficult times and I have happily made it to my destination. Thank you for making me the best version of myself. I love you.

That said, I still renew my thanks to everyone (even the people I didn't mention) because they directly or indirectly contributed to the realization and writing of this work.

Thank you.

Contents

List of Figures

List of Tables

Introduction

Motivation and goal

Unidirectional continuous fibers reinforced polymer matrix composite materials are characterized by long stiff fibers (glass or carbon fibers for instance) embedded in a polymeric matrix (thermoplastic or thermoset). In general, the fibers are the principal load carrying constituent of the composite materials, while the polymeric matrix acts as a load transfer medium and keeps the fibers in place, maintaining their position and orientation (Mallick, 2008). The mechanical properties of unidirectional composite materials are strongly direction dependent and their density is very low, making their strength-to-weight ratio extremely high compared to metals for example (Mallick, 2008; Campbell, 2010). These characteristics make composite materials perfectly suited for industrial application where the aim is to reduce the overall structural weight, maintaining high performances. In particular, since the material parameters are direction dependent (due to the microscopic organization of the constituents), designing a composite structure means that the fibers (which sustain most of the load) are oriented depending on the set of structural loads (Ghiasi et al., 2009, 2010; Dai et al., 2017).

Nowadays, composites materials are widely used in the most important industrial sectors, such as aerospace (Jeff Sloan, 2021a), automotive (Jeff Sloan, 2021b) and in the renewable energies (Hannah Mason, 2021b).

In the automotive sector (Macke et al., 2013), many structural components are made of composite materials. Tubes and plates, driveshafts, springs and brake discs are just a few examples (more can be found in Macke et al. (2013)).

Regarding the application of composites in the high performance automotive industry, the teams of the Formula 1, which is the pinnacle of the racing motor-sports, make an intensive use of composites in their cars (Ben Skuse, 2020). Indeed, 80% of a Formula 1 car's volume is made of carbon fibers reinforced polymeric matrix composite materials.

An interesting example in the automotive sector proposed by Williams Advanced Engineering (2021) is the carbon fibers reinforced composite battery case for the FW-EVX electric vehicle. According to Williams Advanced Engineering (2021), the chassis designed in this way turns out to be 40% lighter with respect to the classical electrical vehicle chassis.

The Tucana project developed by Jaguar and Land Rover et al. (2021) aims to reduce the overall weight of the vehicle and to increase its stiffness at the same time, replacing aluminium and steel alloys with composite materials in order to reduce fuel and energy consumption.

Composites have also become part of the commercial car market, even if they have still quite high end costs. The composite-intensive cars proposed by BMW are discussed in Ginger Gardiner (2016) and Hannah Mason (2021a).

The most common example of intense composite use in the renewable energy sector are the wind turbine blades. The rotor blades can reach over 100 m in length, therefore composite materials in this application are mandatory (Mishnaevsky et al., 2017). Composites are also largely used in energy storage tanks (Ginger Gardiner, 2021). Hydrogen pressure vessels are especially used for space applications, but also in the automotive sector for hydrogen cars. Currently, the Type-V pressure vessels made entirely of composite material is a developing technology used for hydrogen storage (Grace Nehls, 2021).

The most famous companies in the aerospace sector are Airbus and Boeing. The Airbus A350-XWB (Airbus, 2017) and the Boeing 787 (Justin Hale, 2008) are two remarkable examples of composite-intensive commercial aircraft. In particular, more than 50% of the A350-XWB weight is made of composite materials. Also, it is worth to mention the Airbus A400M (Jeff Sloan, 2012), a composite-intensive military aircraft. The parts and components of an aircraft where composites find their applications are: the wings and the fuselage, but also galleys and interiors (Collins Aerospace, 2020a,b). Other composites applications in the aerospace industry can be found in Dutton et al. (2004).

Following the IEA-COP26 Net Zero Summit (IEA, 2021), the reduction of the environmental impact in general, and in particular of the carbon-dioxide (CO_2) emissions for aircraft and vehicles, became a fundamental goal that must be achieved. In this scenario, composite materials play a game-changing role, this is why they are so widely used across all industrial sectors. Indeed, as we mentioned earlier, replacing metals alloys with composite materials (Campbell, 2010) leads to a lower weight structures, and therefore a relevant reduction of fuel consumption. In this sense, the industrialization of composites would help significantly the transition towards zero emissions by 2050, as established at the Summit. In particular, in order to increase the production rate and to improve the quality and the repeatability of composite structures, companies are moving towards automated manufacturing processes, like for instance: the thermoforming process, the automated tape placement, and many others (Campbell, 2004).

Automated manufacturing processes are very cost-effective, and the costs can be reduced even more if the manufacturing processes are performed out-of-autoclave (Lukaszewicz et al., 2012). The autoclave oven is used for the curing process of fibers reinforced thermoset matrix composite structures. The curing process requires long cycle times (of the order of hours) under controlled temperature and pressure conditions, compared to the few minutes associated to the out-of-autoclave processes which can be developed for thermoplastic matrix composite structures, and the size of the manufactured parts are dictated by the dimensions of the oven. Moreover, another not negligible aspect in terms of environmental impact reduction is that thermoplastic composites have the capability to be recycled in a simple fashion, compared with the recycling process of the thermoset composites which is way more difficult.

Currently, automated manufacturing processes coupled with thermoplastic matrix composite materials are used in several industrial sectors, like automotive and aerospace sectors (Friedrich and Almajid, 2013; Björnsson et al., 2015). Advantages and drawbacks of automated manufacturing processes are well highlighted in Schledjewski (2009); Lukaszewicz et al. (2012); de Kruijk (2018); Martin et al. (2020).

The Centre technique des industries mécaniques (CETIM), the company which is funding the present thesis work, develops in particular two manufacturing process: the Laser Assisted Tape Placement (LATP) and the Quilted Stratum Process (QSP). Both of these manufacturing processes are used in order to achieve an high production rate, and their building block are the unidirectional fibers reinforced thermoplastic composite materials. The QSP manufacturing process, invented by CETIM, is similar to a thermoforming process (Campbell, 2004), where the machine uses thermoplastic composite materials patches including different fibers orientations, enabling to manufacture composites parts in just a few minutes (Ginger Gardiner, 2017; Irisarri et al., 2019). In our discussion, we focus on the LATP manufacturing process, which is an automated lay-up process with in-situ consolidation by means of a laser heat source (Lamontia et al., 2003; Schlottermüller et al., 2003). CETIM, specifically, uses the LATP manufacturing process in order to manufacture tubes and pressure vessels made of thermoplastic composite materials. The machine winds-up and consolidates around a turning mandrel, or applies over a mold, a unidirectional (UD) fibers reinforced thermoplastic matrix composite tape. Placing tapes side by side, the machine builds-up a composite layer of the structure. Manufacturing and laying layer over layer, the LATP machine builds up the whole structure. Many phenomena involved in the LATP manufactur-

ing process contribute to generate a complex initial state in the manufactured structure. For example, during the consolidation process, severe temperature gradients within the structure are induced by the laser, locally generating residual stresses and strains distributions.

One of the most important advantages of the LATP manufacturing process, and of the in-situ consolidation processes for thermoplastic matrix composites in general, is that an out-of-autoclave consolidation process is achievable (Schledjewski, 2009), which is not generally possible with the thermoset matrix composites manufacturing processes. For this reason, due to the great potential of the LATP, mastering the manufacturing process is paramount and still an open topic (Martin et al., 2020).

The LATP manufacturing process, due to its high velocity consolidation process (the placement process can reaches 10 m/min and the cooling rates can exceed 1000°C/s), induces locally high temperature gradients, which contribute to generate a complex and non-negligible initial state within the manufactured composite structure (Barnes and Byerly, 1994; Parlevliet et al., 2006; Baran et al., 2017; Schäkel et al., 2019; Hosseini et al., 2021). This needs to be taken into account in the design and sizing of the structures.

In this scenario, the main goal of the present thesis work is to understand the principal physical mechanisms ruling the LATP manufacturing process, in order to develop and implement a model which is able to predict the residual stresses and strains induced by the LATP within the composite structure. The developed model is implemented on the commercial finite element software Abaqus and then transferred to the CETIM for the prediction of the mechanical properties of the manufactured composite structure. The mechanical properties influenced by the initial state (residual stresses and strains induced by the LATP) of the manufactured structure are, for example, the static and fatigue resistance and the durability. Knowing the residual stresses distribution, it is possible to understand the loads carried by the constituents of the composite material (the fibers and the thermoplastic matrix), and therefore the hazard and the potential defects within the manufactured structure. Due to the extreme complexity related to the LATP, and since the developed models need to be transferred to CETIM for industrial applications, another key factor of this work was to use an approach that would allow us to describe the physical phenomena involved in the LATP manufacturing process as simply as possible, in order to achieve a faster resolution.

A detailed descriptions of the thesis contents and structure is presented in the next Section.

Outline of the manuscript

The core of the present thesis work consists in five chapters.

The first two chapters represent the state of the art of this work: they describe the principal physical phenomena involved in the Laser Assisted Tape Placement manufacturing process of a thermoplastic matrix composite structure, and how these phenomena build-up the initial state in the manufactured structure. In particular, Chapter 1 discusses the different sources of residual stresses and strains within composite structures, while Chapter 2 details the specific role of geometry and anisotropy, already addressed in the literature.

The following three chapters present the original contributions of this work, enabling us to account for the complex role of the thermal history seen by the part. In particular, a temperature-dependent viscoelastic constitutive model and a simple unidirectional thermal model for the LATP are discussed in Chapters 3 and 4, while the finite element simulations performed on tubular structures are presented and discussed in Chapter 5.

In Chapter 1, a state of the art is presented, concerning the main sources of residual stresses and strains, which characterize the initial state of the manufactured composite structure. The machine, during the manufacturing process, mechanically and thermally loads the structure inducing stresses and strains. In particular, thermal and crystallization strains, if incompatible with the system, generate residual stresses within the structure and the sources of incompatibility are addressed. Once all sources of residual stresses and strains are defined, the major ones are modelled to understand the role of each.

One of the most important source of residual stress and strain found at the macro-scale is the combined effect of the curved geometry of the structure and the anisotropy of the composite material, which is analyzed in Chapter 2. A structural model, already proposed in the literature, is implemented in order to assess the residual stresses in composite tubes with different stacking sequences. Experimental residual strains measured on tubes, provided by the CETIM, are compared with the results assessed through the structural model. From the experimental results, it was found that some tubes had a different response than that predicted by the structural model, demonstrating the important role of the thermal history induced by the LATP manufacturing process.

In order to be able to address the effects of the thermal history induced in the manufactured structure by the LATP, a new mechanism based temperature-dependent viscoelastic constitutive model suited for unidirectional fibers reinforced composite matrix is presented in

Chapter 3. Many viscoelastic models can be found in the literature, where viscoelastic parameters are introduced through complex relaxation tensors (Pettermann and DeSimone, 2018). Here, a decomposition of the stress and strain tensors was proposed, which makes it easier to distinguish the contribution of the fibers and the matrix to the constitutive behavior of the composite material. Supposing that the deviatoric response of the matrix is viscoelastic and that the fibers are elastic, the linear viscoelastic model is applied only on certain terms of the composite's response. The proposed model is implemented in a UMAT Abaqus user subroutine for numerical simulations.

The thermal history induced by the LATP is extremely complex (Hassan et al., 2005) and very expensive from the point of view of the computation time. Consequently, in Chapter 4, a one-dimensional heat transfer transient equation is used to describe in a simplified way the thermal history induced by the consolidation phase of the LATP manufacturing process. The thermal model includes the heat flux between the substrate and the mandrel and the heat flux between the incoming layer and the environment. Particular attention is paid to the initial condition to be used in the thermal model, which is the temperature distribution in the structure thickness generated by the heating phase of the LATP. The analytical solution of this simple thermal model is presented, then implemented in a UTEMP Abaqus user subroutine for numerical simulations.

New thermo-mechanical simulations are performed in Chapter 5 on tubes using the commercial finite element software Abaqus. Following the additive manufacturing modelling technique presented in Michaleris (2014), a similar approach was used here to achieve a simplified model of the automated lay-up process of the LATP. In this scenario, residual stresses are assessed and then released by simulating a cut along the axial direction of the tubes. The numerical residual strains are compared again with the experimental results provided by CETIM.

The overall conclusions and perspectives are presented at the end of the thesis.

1 - Initial state of the manufactured structure: sources of residual stresses and strains

1.1 . Laser Assisted Tape Placement manufacturing process

Automated manufacturing processes for composite materials have been extensively used in the last years in order to increase the production rate of composite structures (Campbell, 2004). Until recently (see the Introduction for details), the manufacturing of composite structures was relatively slow, especially due to the autoclave curing process needed by the thermoset matrix, which was the most commonly used for structural applications. On the other hand, thermoplastic matrix composites can be melted and cooled freely, making them the best candidate for fast and automated out-of-autoclave processing like the Laser Assisted Tape Placement (Schledjewski, 2009).

The Laser Assisted Tape Placement (LATP) is an automated technique used to fabricate composite structure like plates, tubes and pressure vessels. The basic building block employed by the LATP is the preimpregnated unidirectional continuous fibers reinforced thermoplastic tape.

In the LATP manufacturing process (see Figure (1.1)) the composite structure is manufactured following three steps that occur at the same time:

- following particular trajectories, the placement head applies over a mold, or winds up over a turning mandrel, the composite tape;
- during the placement process, in order to weld the incoming tape on the substrate, a laser heat source heats up the inner surface of the incoming tape and the outer surface of the previously consolidated substrate, which cool down together after the laser is removed;
- in order to achieve a better consolidation between the tape being placed and the substrate, a deformable silicone roller (called also compaction roller) applies a pressure transversely to the tape.

The LATP machine fabricates the single layer of the composite structure by placing tapes side by side over the mandrel, or over the previously consolidated substrate. Laying layer over layer, the whole composite structure is manufactured.

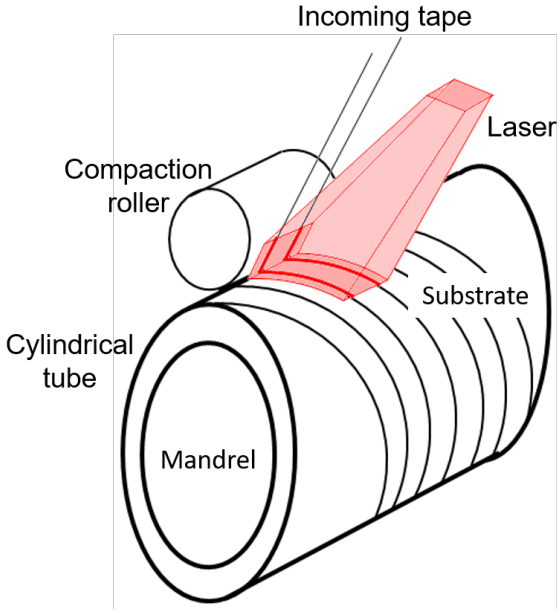

Figure 1.1: Schematic image of the laser assisted tape placement manufacturing process. The key LATP elements represented in the present Figure are: the laser heat source, the incoming tape and the previously consolidated substrate, the compaction roller and the cylindrical mandrel.

During the LATP manufacturing process, the composite structure locally undergoes numerous heating and cooling cycles, characterized by high and complex temperature gradients, making the LATP thermal history extremely complex and difficult to model (Sonmez et al., 2002; Grouve, 2012; Kok, 2018). Specifically, in the heating process the laser heats the incoming tape and the substrate almost instantaneously, making them locally reach and exceed the melting temperature of the thermoplastic matrix. After the heating source is removed, the placed tape and the substrate cool down, bonding together and reaching the room temperature (or the mandrel temperature) in a few seconds. During these rapid heating and cooling phases, the thermoplastic matrix undergoes many modifications, such as melting, crystallisation, solidification, thermal dilatation and contraction. The mandrel, on which the LATP machine manufactures the composite structure, can be heated or left at room temperature. This means that the heating and cooling process can significantly change with the mandrel temperature, changing the thermal history experienced by the manufactured structure.

The main goal of the present PhD thesis work is to model and simulate the initial state of a thermoplastic matrix composite structure

manufactured by the Laser Assisted Tape Placement. As it was just illustrated, the physical phenomena involved in the LATP manufacturing process are numerous and inherently multi-physics (thermal, mechanical and chemical problems for instance), leading to extreme complexity in terms of modelling and simulations. In addition to the complexity, modelling the whole LATP manufacturing process would certainly lead to computational times that are too high and not applicable for industrial use. Therefore, the approach retained here is to analyze and address the main physical mechanisms generating the residual stresses and strains distributions within the manufactured structure. Modeling each of the key mechanisms should enable us to predict the initial state of the structure in a reasonably accurate fashion. Furthermore, it should enable us to understand the role of each mechanism in determining the overall initial state, thus gaining an insight on which process parameters can be acted upon to control or mitigate it.

In the following Sections of the present Chapter, a state of the art on the main sources of process-induced residual stresses and strains within the composite structure is presented. The aim here is to discuss the main physical mechanisms underlying the generation of residual stresses and strains within a composite structure manufactured by LATP. More details about the process-induced residual stresses and strains in general can be found in Nairn and Zoller (1985); Barnes and Byerly (1994); Parlevliet et al. (2006); Baran et al. (2017).

It should be noted that the state of the art discussed in this Chapter does not cover all of the topics discussed in the manuscript, but only the specific question of the origins of residual stresses and strains in composite structures. The state of the art related to other aspects of this work, such as viscoelastic models for composites and thermal models for LATP manufacturing process, are discussed directly in the appropriate Chapters later in the manuscript.

1.2 . Geometrical distortions and residual stresses induced by the manufacturing process

The manufacturing processes of composite structures (Campbell, 2004), and in particular the LATP manufacturing process, which subjects the structure to several thermal cycles characterized by high temperature gradients (Sonmez et al., 2002), generate an initial state within the structure (Parlevliet et al., 2006, 2007a,b). This initial state manifests itself in the form of residual stresses and/or geometric distortions.

Geometric distortions and residual stresses are two sides of the same coin. They both develop due to the presence of non-elastic strains,

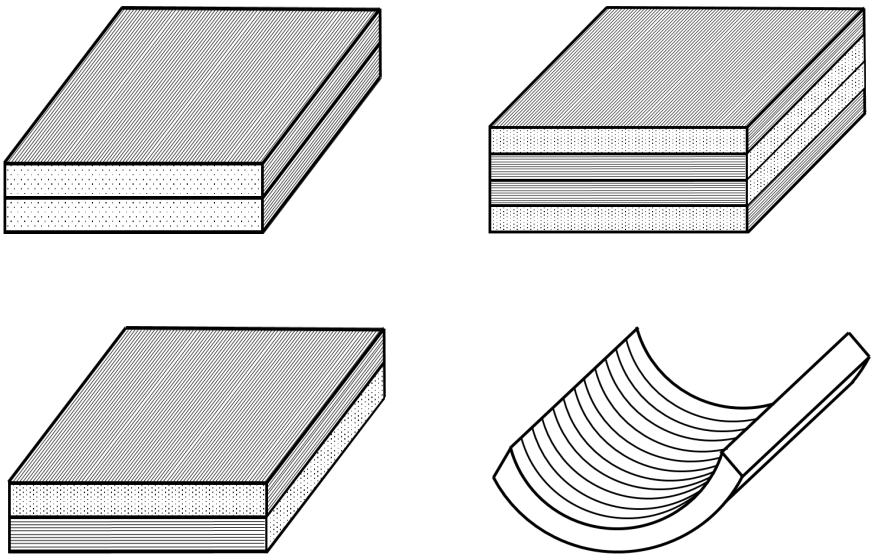

Figure 1.2: Laminate with open surface geometries: flat plates with different stacking sequences (unidirectional, symmetric, unbalanced); curved laminate.

such as thermal dilatation/contraction or crystallisation strain, within the structure. In particular, geometric distortions occur when the structure is not constrained (externally or internally), thus they generally become visible after the mold, or the mandrel, is removed, whereas residual stresses develop as a reaction to an (external or internal) constraint and they are not easy to detect, unless they are released and the associated geometric distortions are observed.

In structures with a slender aspect ratio, such as many laminated composite structures, a distinction can be made between in-plane distortions and out-of-plane, or bending, distortions. The second ones are much more visible, since relatively small strains can bring about significant, and potentially problematic, shape changes of a structural part. In-plane distortions, on the other hand, become significant only for very large parts, and they are often of little concern.

Bending distortions can be exhibited by structures characterized by an open surface geometry, such as flat or curved laminates (see Figure (1.2)) (Hahn and Pagano, 1975; Hyer, 1981). In particular, flat laminates can develop bending distortions due to a loss of symmetry with respect to the midplane, associated with an unbalanced stack or with an unsymmetric thermal history. On the other hand, composite structures characterized by a closed surface geometry, like tubes and pressure vessels (see Figure (1.3), tend to minimize the bending distortions induced by the manufacturing process, and to develop residual stresses

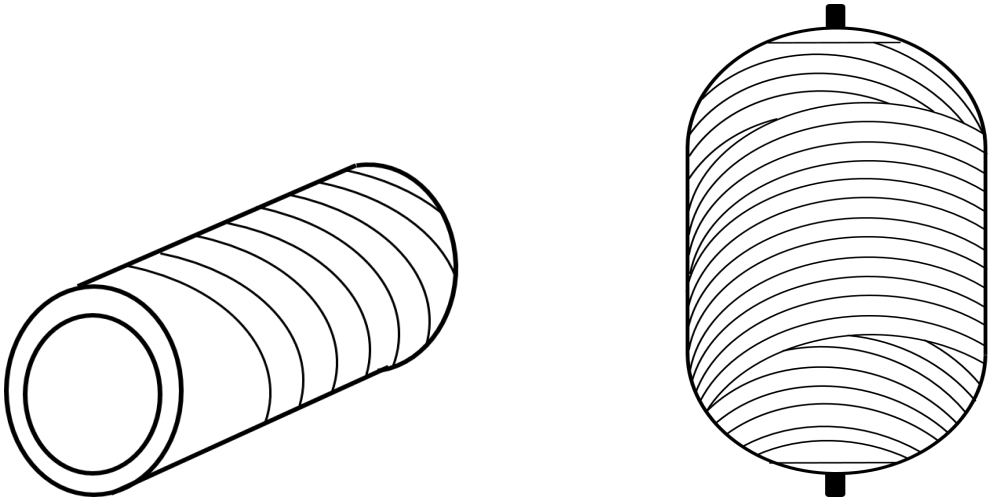

Figure 1.3: Laminates with closed surface geometries: composite tube (left) and composite pressure vessel (right).

instead.

The mandrel (Figure (1.1)), the closed surface geometry of the composite structure (Figure (1.3)), and the stacking of layers with different fibers orientations (Figure (1.2) right) constitute external or internal constraints which inhibit (or significantly restrict) the shape distortions induced during the manufacturing process. For this reason, process-induced residual stresses can be locked within the composite structure. It should be noted that residual stresses and geometric distortions can coexist within the same structure, related to different imposed or liberated constraints.

The sources of non-elastic strains and the (internal) constraints within composite structures at different scales are discussed in the following.

1.3 . Sources of incompatibility

The non-elastic strains (such as thermal dilatation/contraction or crystallisation strain) which develop within a structure during manufacturing may be incompatible. An incompatible strain field cannot be derived from a displacement field, therefore an elastic stress/strain field is needed in order to accommodate it. Incompatibilities can occur at different scales. For composite materials, we can consider three scales: the micro-scale, which is the scale of the composite constituents, that is the fibers and the matrix, the meso-scale, which is the scale of the laminate with its own stacking sequence, and the macro-scale, which is the scale of the complete structure, characterized by its own geom-

etry. It is important to note that phenomena occurring at the micro-scale will also have an effect (relevant or not) at the higher scales (the meso-scale and the macro-scale), whereas phenomena occurring at the higher scales will have no effect at the lower scales.

The unidirectional fibers reinforced polymeric matrix composite is an anisotropic and heterogeneous material which consists of long and continuous parallel fibers embedded in a polymeric matrix.

1.3.1 . Micro-scale

At the micro-scale, the different behavior between the fibers (carbon or glass for instance) and the polymeric matrix generates an incompatibility (see Figure (1.4)). In particular, considering a uniform cooling during manufacturing, the induced matrix thermal strain will be bigger than the thermal strain of the fiber. Indeed, the coefficient of thermal expansion (CTE) of the matrix is roughly $30(10^{-6})/°$C, which is two order of magnitude bigger than the CTE of the carbon fiber ($\sim 0.2(10^{-6})/°$C), and one order of magnitude bigger than the CTE of the glass fiber ($\sim 5(10^{-6})/°$C). Moreover, when the matrix temperature remains for a sufficient time above its glass transition temperature, crystallization of the polymeric matrix can occur, which can also be associated to a non-elastic strain (Cogswell, 1992). In order to accommodate the incompatibilities generated by the mismatch of CTEs and by the crystallization strain, residual stresses arise. In this specific case, the fiber will be in compression while the matrix will be in traction (Parlevliet et al., 2006).

In this work, we choose to describe the material at the scale of the ply, so residual stresses and strains at the micro-scale are not the object of the present study. They are better detailed in Parlevliet et al. (2006, 2007a,b).

1.3.2 . Meso-scale

At the meso-scale, the homogenized composite ply has an anisotropic behavior, which means that its material properties are strongly direction-dependent. In particular, the composite material ply can be considered transversely isotropic. The composite ply behavior in the fibers' direction (1) is dominated by the fibers' behavior while the behavior in the transverse plane $(2, 3)$ is dominated by the matrix behavior (see Figure (1.5)).

The composite laminate, on the other hand, is an heterogeneous material, because it is constituted of several layers stacked on top of each other, and in each layer the fibers are generally oriented in a different direction. Therefore, the stacking sequence of the composite laminate generates an incompatibility, since the direction dominated

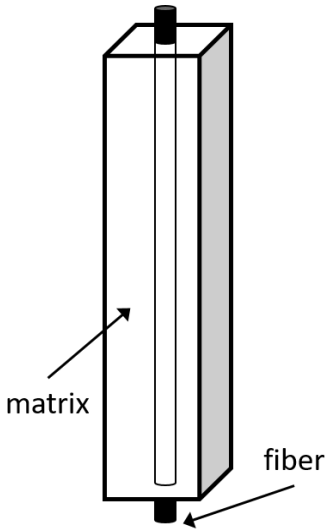

Figure 1.4: Fiber embedded in the polymeric matrix.

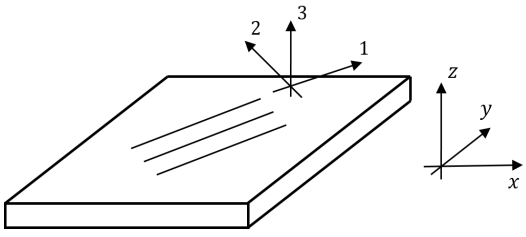

Figure 1.5: Material coordinates for the composite ply (1,2,3) and global coordinates for the composite plate (x,y,z).

by the fibers' behavior of one ply could correspond to the direction dominated by the matrix's behavior of the adjacent ply (Jeronimidis and Parkyn, 1988; Barnes and Byerly, 1994; Parlevliet et al., 2006). In order to accommodate the incompatibility generated by the mismatch between CTEs of adjacent plies, residual stresses arise at the meso-scale.

Let us consider a non-symmetric cross-ply laminate, $[0^\circ_n/90^\circ_n]$, subjected to a homogeneous temperature difference. According to the above discussion, the direction dominated by the fibers' behavior in one ply imposes a constraint on the direction dominated by the matrix behavior in the adjacent ply, and vice-versa. This heterogeneous thermal shrinkage induces thermal stresses, that can result in bending geometric distortions of the composite laminate if the external constraint imposed for example by the mandrel is removed. In this particular case, before the mandrel removal, the fibers dominated direction (1) of each ply is in compression, while the matrix dominated direction (2) is in traction (Parlevliet et al., 2006).

Another important source of incompatibility that can be found at the meso-scale are the temperature gradients (Manson and Seferis, 1992; Parlevliet et al., 2006). High temperature gradients appear in rapid cooling processes, such as the well known quenching process for metals, or in manufacturing process characterized by a localized consolidation, like the LATP for manufacturing composite materials. High temperature gradients generate a heterogeneous thermal strain field, which requires residual stresses in order to be accommodated. Let us consider a unidirectional composite plate at a temperature above the melting temperature of the polymeric matrix, and subjected to a non uniform cooling process through the thickness of the laminate. The external surfaces of the laminate, subjected to the heat exchange with the air of the room, cool down faster than the core of the plate. For temperatures above the glass transition temperature of the polymer matrix (Nicholson, 2002; Melo and Radford, 2003; Grogan et al., 2015), viscous stress relaxation occurs at different rates due to the high cooling rates involved on the outer surfaces compared to the laminate core. Therefore, the laminate core is able to relax stresses more than the external surfaces, generating a residual stress distribution in the thickness of the structure. In other words, during the cooling process, the solidified material close to the external surfaces of the laminate imposes a constraint to the still melted material inside generating a residual stress distribution (Chapman et al., 1990; Manson and Seferis, 1992; Parlevliet et al., 2006). The residual stresses distribution will be most significant in the matrix dominated direction (2), as it is the polymer matrix that can relax at temperatures above the glass transition. The

phenomenon just explained is found in the literature as the skin/core effect (Parlevliet et al., 2006).

The skin/core effect caused by high temperature gradients is linked with the residual stresses induced by the numerous and fast thermal cycles (fast heating and cooling processes) that characterized the thermal history of a layup manufacturing process like the LATP. The mechanisms underlying the generation of thermal stresses during the composite layup process are well illustrated in Barnes and Byerly (1994); Eduljee and Gillespie (1996). The LATP machine sequentially places composite tapes one on top of each other to build and consolidate the whole structure. In the placement process, the machine applies each new tape, at high temperature, over the previously consolidated substrate, at low temperature. Therefore, each incoming tape shrinks over the substrate, putting it in compression, while the substrate puts the tape under tension. In particular, a unidirectional fibers reinforced matrix composite plate (Figure 1.2, top left) manufactured through the LATP technique, bends upwards after the mandrel removal.

In the placement process, the LATP machine heats the thermoplastic matrix composite above the melting temperature of the polymeric matrix, inducing the crystallization of the matrix (the crystallization starts when the semi-crystalline thermoplastic matrix exceeds the glass transition temperature (Ward and Sweeney, 2004)). When the crystallization process occurs, in addition to the thermal strains, matrix strains due to the crystallized portion of the matrix arise. The high temperature gradients, generated by the LATP manufacturing process, could induce crystallization gradients within the composite structure (Cogswell, 1992; Sonmez and Hahn, 1997a; Tierney and Gillespie, 2004) and their effect in terms of residual stresses can be treated in a similar way as the thermal gradients (Tierney and Gillespie, 2004).

1.3.3 . Macro-scale

The composite structure manufactured (at the macro-scale) is characterized by its own, generally non-flat, geometry (see Figure (1.2), bottom right, or Figure (1.3)) and by its stacking sequence. In Section 1.2, the closed surface geometry (Figure (1.3)) and the stacking sequence (Figure (1.2) top right, bottom left) are presented as constraints. At the macro-scale, the combined effect of the geometry of the part and the stacking sequence, especially the anisotropy of the single composite ply, is a source of incompatibility, and it was presented the first time by Nairn and Zoller (1985). Considering, for instance, a composite tube subjected to a constant temperature difference, the external curved geometry of the structure couples the in-plane kinematics (defined by

the circumferential direction of the tube) with the out-plane kinematics (defined by the radial direction of the tube). Because of the anisotropy of the composite layer, the induced thermal in-plane strains are different with respect to the thermal out-of-plane strains, requiring residual stresses to accommodate the incompatible strain fields. This particular case is detailed in Chapter 2.

All of the phenomena already discussed at the mesoscale, that is the stacking sequence of the composite structure, the temperature gradients and the thermal history of the manufacturing process, must also be considered at the macroscale.

1.4 . LATP Residual stresses and strains

Based on the previous discussion on the possible sources of residual stresses and geometric distortions, the physical phenomena involved in LATP manufacturing process are presented in this Section.

Firstly, we consider the loads directly applied to the structure during the manufacturing process, which constitute stresses and strains directly and locally applied to the structure. These loads are:

- the winding tension applied by the machine on the composite tape during the placement process, which is an elastic stress directly applied on the tape (Eduljee and Gillespie, 1996);
- the transversely pressure imposed on the tape is a stress applied by the compaction roller in order to achieve a better bonding between the incoming ply and the previously consolidated substrate (Colton and Leach, 1992);
- the thermal load, imposed firstly by the laser heating source and secondly by the subsequent cooling process, which causes a local non-homogeneous temperature field within the structure hence a local non-homogeneous thermal and crystallization strain (Manson and Seferis, 1992).

According to what we said in Sections 1.2 and 1.3, internal and external constraints are:

- the closed geometry;
- the stacking sequence of the composite structure;
- the mandrel on which the LATP machine welds the composite tapes, which does not allow the relative motion between the mandrel and the structure during the manufacturing process

Consequently, thermal strains and crystallization strains induced during the manufacturing process are non-elastic deformations that can be incompatible with external and internal constraints, and are therefore accommodated by residual stresses.

1.5 . Modeling approach

The laser assisted tape placement generates an initial state within the manufactured structure in two ways: directly and indirectly. The LATP directly induces residual stresses and strains distributions through the loads applied within the structure during the manufacturing process, such as the winding tension and the roller pressure (seen in Section 1.4). The thermal load applied by the laser heat source induces non-elastic strains such as thermal and crystallization strains. Non-elastic deformations that are incompatible with external and internal constraints present at different scales (as discussed in Section 1.3), are accommodated by residual stresses which are indirectly generated by the manufacturing process.

At the micro-scale, the internal constraint is represented by the fiber matrix interaction. At the meso-scale and at the macro-scale, the internal constraints are the stacking sequence of the laminate and the geometry of the manufactured part, while the external constraint is the mandrel. At these scales, the high temperature gradients induced by the LATP during manufacturing generate a heterogeneous thermal strain field, accommodated by residual stresses. In this context, viscous stresses relaxation occurs at different rates, inducing a residual stresses distribution within the structure. The fast and numerous thermal cycles to which the manufactured structure is subjected by the automated layup process of the LATP makes the thermal history particularly complex to track.

Our goal is to model and simulate the initial state of a composite structure manufactured by the LATP. Therefore, in our discussion we are focused on the modeling at the meso- and macro-scale. It is important to note that aspects addressed at the micro-scale could also affects the following meso-scale and macro-scale, leading to a high number of physical phenomena to consider and making numerical modeling extremely complex and costly in terms of computational time. For this reason, in the present thesis work, the main physical mechanisms underlying the residual stresses and strains buildup within the composite structure manufactured by the LATP are addressed. In order to accomplish the goal, several assumptions are also made along the discussion.

At first, we suppose that one of the most important source of resid-

ual stresses and strains is the combined effect of the geometry of the manufactured structure and the anisotropy of the composite, which is addressed in Chapter 2. This aspect was already pointed out previously in the literature, and the main consequences are analyzed in Chapter 2 using a structural model for a composite tube to quantify this phenomenon. From the comparison between the results of the structural model and the experimental measurements, it can be noticed the significant effect of the geometry and anisotropy in terms of initial state. However, it turns out not to be enough to justify the experimental responses of the tubes.

In order to take into account the complex thermal history induced by the LATP, a temperature-dependent visco-elastic constitutive model is developed in Chapter 3. A stress/strain tensors decomposition is used to separate the contributions of fibers and matrix on the constitutive behavior of the unidirectional fibers reinforced composite material. Under this rigorous geometrical and mechanical framework, and assuming a viscoelastic behavior only on the deviatoric response of the matrix, a linear viscoelastic model is applied only on the affected decomposition terms.

Assuming dominant temperature gradients in the thickness direction of the manufactured structure, a one-dimensional thermal model is used in Chapter 4 to describe the consolidation process induced by the LATP during manufacturing. The initial condition is the temperature distribution induced by the heating phase of the LATP, which is taken from results proposed in the literature. In order to take into account the thermal effects of the mandrel and the environment, mixed boundary conditions are used. The analytical solution of the thermal model is also developed in Chapter 4.

The LATP manufacturing process is simulated, in Chapter 5, on composite tubes using the typical modeling strategy of the additive manufacturing process. No adjustment of the model parameters, which were taken from the litterature, or of any other hypothesis made along the way, was considered in this Chapter. The numerical results are then compared with the experimental results provided by CETIM, proving that the main physical mechanisms underlying the process-induce initial state were addressed. A gap between experimental and numerical results remains, and the analysis of the sources of this gap, related most probably to the description of the thermal history and to the lack of modeling of the crystallisation effects, constitutes the perspectives of this work.

2 - Structural modelling: the effect of geometry and anisotropy

2.1 . Introduction

In Chapter 1, a state of the art of the sources of the residual stresses and strains directly related to the manufacturing process and the incompatibilities at different scales was presented. In this Chapter, an element that we think plays a key role in our discussion (as it is shown in the following) is presented. The combined effect of the curved geometry of the manufactured structure and the anisotropy of the composite material is discussed in the present Chapter, while the other residual stresses/strains sources like the temperature gradients are addressed later on in the discussion.

This Chapter explores how the curved geometry of a composite structure generates residual stresses. In particular, these considerations already known in the literature (Hyer and Rousseau, 1987; Nelson and Cairns, 1989; Tutuncu and Winckler, 1993) are used to calculate residual stresses in tubes with different stacking sequences. The analytical results are then compared with experimental results provided by the CETIM. The attempt here is to show how relevant residual stresses generated by the geometry and anisotropy are. In this scenario, the cumbersome effect of the out-of-plane kinematics will deeply affect the choice of kinematics in modelling.

In Section 2.2, the kinematic compatibility equations in cylindrical coordinates are given to highlight how the curved geometry couples the in-plane kinematics with the out-of-plane kinematics. The mechanical behavior of the composite material is strongly direction-dependent, and in particular the in-plane behavior is generally different with respect to the out-of-plane behavior. Specifically (see Figure (1.5)), the material direction (1) is dominated by the fibers' behavior, while the material directions (2) and (3) are dominated by the matrix behavior. The material direction (3) corresponds to the structure's thickness, while the plane identified by the material directions $(1, 2)$ is the laminate plane. The laminate plane and the thickness direction are coupled by the curved geometry of the structure, consequently an incompatibility is generated.

In order to address the combined effect of the geometry and the anisotropy, a structural analytical model presented by Hyer et al. (1986); Hyer and Rousseau (1987); Tutuncu and Winckler (1993) is studied in

Section 2.3. Under the hypothesis of transverse isotropy for the composite ply, the generalized plane strain and the continuity along the circumferential direction, the thermo-mechanical equations for a composite tube are derived in Section 2.3.1. The circumferential stress distribution induced in a closed tube, assessed with the structural model, generates a bending moment, which results in an opening or closing displacement when the tube is cut. In Section 2.3.2, the bending moment is applied on a curved beam model representing the cross-section of a cut tube, in order to assess the theoretical opening or closing displacement resulting from a cut along the tube's length, which releases the thermal residual stresses. The through-thickness stresses distribution and the displacement associated to a longitudinal cut are shown in Section 2.3.3 for an unconstrained $[90°]$ tube subjected to a uniform temperature difference.

In order to measure the residual stress distribution within the tube, the experiments performed by the CETIM on several tubes made of thermoplastic matrix composite material (carbon/PEEK) are shown in Section 2.4.1. The specimens were manufactured with different processing conditions (specifically, cold or hot mandrel). After manufacturing, a cut along the axial direction of the tube was performed (Barnes and Byerly, 1994; Eduljee and Gillespie, 1996; Casari et al., 2006) in order to measure the geometric distortions that appear after the cut, which are the results of the (partial) release of residual stresses trapped in the tubes. The same tubes are modeled with the approach presented in Section 2.3, and the comparison between the experimental and the analytical displacements is performed in Section 2.4.3.

The combined effect of the geometry and the anisotropy deeply affects the choice of the continuum model, and thus of the Finite Element Model (FEM), to be adopted. Indeed, the conventional shell theory has no out-of-plane kinematics, therefore it cannot be used to predict the effects discussed in this Chapter. A complete 3D description has to be used instead, which leads to the choice of 3D volumetric elements with quadratic shape functions for the FEM model (see Section 2.5). In order to describe the composite stacking sequence, two FEM approaches proposed by the Abaqus software are explored in Section 2.5.1. The first strategy analyzed is the Composite Layup Abaqus option, which enables us to use only one 3D mesh element in the thickness of the whole laminate, and the second strategy analyzed is to use one 3D mesh element for each composite layer of the laminate.

In Section 2.6 some comments are presented.

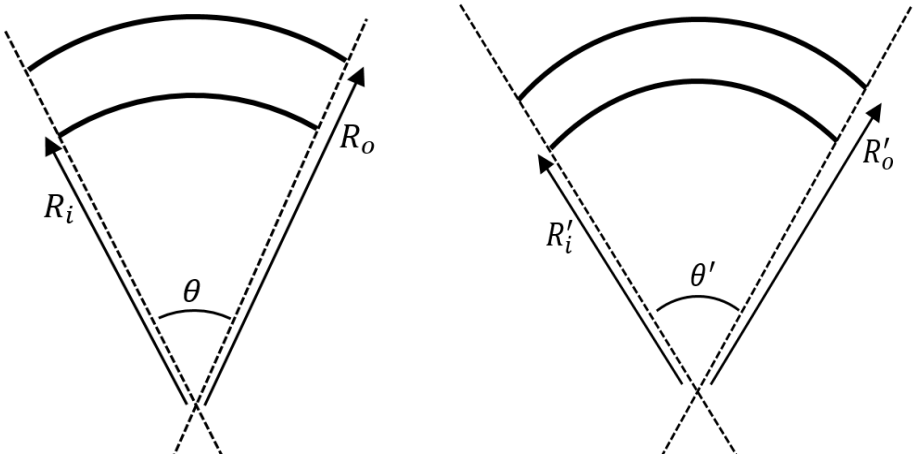

Figure 2.1: Curved geometry: initial configuration (left), deformed configuration (right). The inner radius, the outer radius and the angle of the initial configuration are R_i, R_o and θ. The same parameters but for the deformed configurations are R'_i, R'_o and θ'.

2.2 . Curved geometry and anisotropy

The effect of the curved geometry was studied in the nineties by Nelson and Cairns (1989). In their work, they studied the dimensional changes of a composite laminates during the curing process for thermoset matrix composites.

The effect of coupling the curved geometry and the anisotropy of the composite layer is simply explained here. In Figure (2.1 left) is represented the initial configuration of a curved composite structure with an open surface. The angle θ is the angle enclosed by the circular arc, while R_i and R_o are respectively the inner and the outer radius. In Figure (2.1 right), the deformed configuration is depicted and the deformed geometry parameters are θ', R'_i and R'_o.

If C_i and C_o are respectively the lengths of the inner and outer circular arcs, the enclosed angle θ can be written as a function of the structure thickness h as:

$$\theta = \frac{C_o - C_i}{h}, \quad \text{where} \quad h = R_o - R_i. \tag{2.1}$$

The $(\hat{e}_r, \hat{e}_\theta, \hat{e}_z)$ cylindrical coordinate system of Figure 2.2 is used in the analysis. Introducing a uniform normal strain in the circumferential direction $\varepsilon_{\theta\theta}$ and a uniform normal strain in the thickness direction ε_{rr}, the lengths of the inner and outer circular arcs, respectively C'_i and C'_o, and the thickness h' in the deformed configuration are:

$$C'_o = (1 + \varepsilon_{\theta\theta})\, C_o, \quad C'_i = (1 + \varepsilon_{\theta\theta})\, C_i, \quad h' = (1 + \varepsilon_{rr})\, h. \tag{2.2}$$

The enclosed angle θ' in the deformed configuration can be then written as follows:

$$\theta' = \frac{C'_o - C'_i}{h'} = \frac{(1+\varepsilon_{\theta\theta})\,C_o - (1+\varepsilon_{\theta\theta})\,C_i}{(1+\varepsilon_{rr})\,h} = \frac{(1+\varepsilon_{\theta\theta})}{(1+\varepsilon_{rr})}\frac{(C_o - C_i)}{h}. \quad (2.3)$$

In Equation (2.3), the enclosed angle in the final configuration θ' is a function of the strains in the thickness direction and in the circumferential direction. Thus, the angle variation between the final and the initial configuration ($\Delta\theta = \theta' - \theta$) is written as (Baran et al., 2017):

$$\Delta\theta = \frac{(1+\varepsilon_{\theta\theta})}{(1+\varepsilon_{rr})}\theta - \theta \quad \text{from which follows} \quad \frac{\Delta\theta}{\theta} = \frac{\varepsilon_{\theta\theta} - \varepsilon_{rr}}{1+\varepsilon_{rr}}. \quad (2.4)$$

A difference between the circumferential and the radial strains, $\varepsilon_{\theta\theta}$ and ε_{rr}, results therefore in a change of angle between the original and the deformed configurations.

The uniform strains $\varepsilon_{\theta\theta}$ and ε_{rr}, introduced in the previous equations, can be generated for instance by a uniform and slow cooling process (where temperature gradients can be neglected, such as in a autoclave curing process). In this case, we can describe the thermal strains with respect to a reference configuration $\boldsymbol{\varepsilon}_0 = \mathbf{0}$ at $T = T_0$ as $\boldsymbol{\varepsilon} = \boldsymbol{\alpha}\,(T - T_0) = \boldsymbol{\alpha}\Delta T$, where ΔT is a uniform temperature difference and $\boldsymbol{\alpha}$ contains the Coefficients of Thermal Expansion (CTEs). This can lead to two situations, depending on the CTEs in the directions θ and r:

- either $\alpha_\theta = \alpha_r$, thus $\varepsilon_{\theta\theta} = \varepsilon_{rr}$, in which case $\Delta\theta = 0$;
- or $\alpha_\theta \neq \alpha_r$, thus $\varepsilon_{\theta\theta} \neq \varepsilon_{rr}$, in which case $\Delta\theta \neq 0$.

The first case corresponds to isotropic materials, or to anisotropic materials with specific orientations with respect to the cylindrical coordinates (for instance, to a transversely isotropic composite ply whose fibers are orthogonal to the (r, θ) plane). The second case corresponds to a more general anisotropic material, and in particular to a composite ply whose fibers are not orthogonal to the (r, θ) plane.

Let us consider now a closed surface geometry, such as a tube or a pressure vessel, as discussed in Chapter 1. In this case, the closed geometry of the tube generates a kinematic constraint whereby $\Delta\theta = 0$, and the uniform thermal strains $\varepsilon_{\theta\theta} = \alpha_\theta \Delta T \neq \varepsilon_{rr} = \alpha_r \Delta T$ are no longer compatible. The incompatibility generated needs to be accommodated by elastic strain distributions $\varepsilon^{el}_{rr}(r)$ and $\varepsilon^{el}_{\theta\theta}(r)$, which are respectively the radial and circumferential elastic strains.

In the next Section, a structural analytical model for a composite circular section tube is presented in order to quantitatively evaluate the residual stresses distribution associated to the phenomenon just described.

2.3 . Geometry and anisotropy: analytical structural model

2.3.1 . Residual stresses in the tubes: three dimensional model

A first modeling approach is proposed here for a layered composite cylinder (see Figure (2.2)). The continuum mechanics problem equations are formulated in 3D, then suitably simplified to yield a one-dimensional model in the thickness coordinate. In particular, the model takes into account the effects of the anisotropy and of the geometry at the meso-scale and macro-scale briefly described in Section 2.2, but it neglects the effect of the complex and heterogeneous thermal history of the part. The aim here is to predict the residual stress within a tube of composite subjected to a uniform temperature difference (ΔT). The structural analytical model was first presented by Pagano et al. (1968) and then was further developed in the works Pagano et al. (1970); Hyer et al. (1986); Hyer and Rousseau (1987); Tutuncu and Winckler (1993); Casari et al. (2006). The assumption made are:

- generalized plane strain conditions (Cheng et al., 1995; Zhenye and Shiping, 1990): all the strains, and through the stress-strain relation all of the stresses, are independent from the axial coordinate z;
- due to the material continuity of the tube in the circumferential direction and the invariance with respect to rotation around the axis $\hat{e}_z$, all of the problem quantities are independent from the circumferential coordinate θ;
- the thermal input $\Delta T = T - T_0$ is uniform and so it is the reference temperature T_0.

Problem equations

Initially, the analytical expressions for the radial, circumferential and axial displacements of the problem, are derived for the homogenized transversely isotropic k^{th} ply of the tube (see Figure (2.2)). Then, applying the boundary and continuity conditions, the displacements for the whole layered tube are found.

Following the hypotheses, the radial, circumferential and the axial displacements for a homogeneous layer take the form (Hyer and Rousseau, 1987; Tutuncu and Winckler, 1993):

$$\begin{aligned} u_r(r,\theta,z) &= u(r), \\ u_\theta(r,\theta,z) &= v(r,z), \\ u_z(r,\theta,z) &= w(r,z). \end{aligned} \tag{2.5}$$

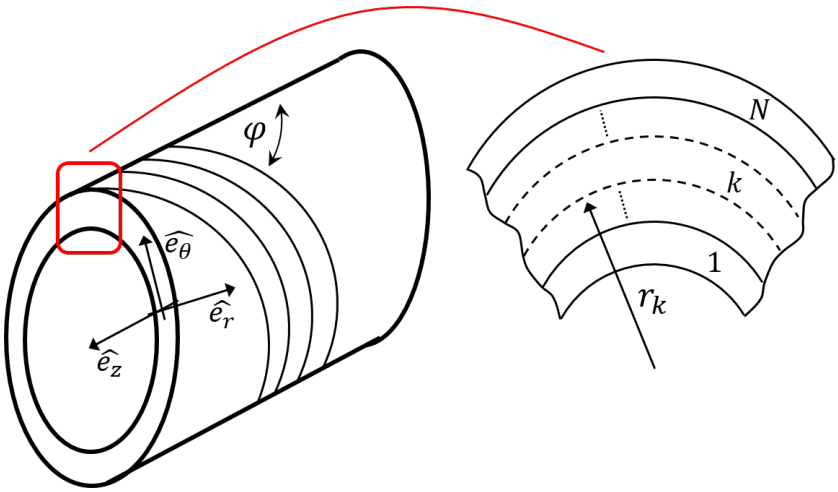

Figure 2.2: Layered composite tube: the angle φ represents the orientation angle of the fibers with respect to the axial direction z. The first and the last layer of the tube are denoted respectively with 1 and N.

The linear Green-Lagrange strain tensor reads:

$$\boldsymbol{\varepsilon} = \frac{1}{2}[\nabla \boldsymbol{u} + (\nabla \boldsymbol{u})^T], \tag{2.6}$$

and in cylindrical coordinates the following strains are obtained:

$$\begin{aligned} \varepsilon_{rr} &= \frac{du}{dr}, & \varepsilon_{\theta\theta} &= \frac{u}{r}, & \varepsilon_{zz} &= \frac{\partial w}{\partial z}, \\ 2\varepsilon_{r\theta} = \gamma_{r\theta} &= \frac{\partial v}{\partial r} - \frac{v}{r}, & 2\varepsilon_{rz} = \gamma_{rz} &= \frac{\partial w}{\partial r}, & 2\varepsilon_{\theta z} = \gamma_{\theta z} &= \frac{\partial v}{\partial z}. \end{aligned} \tag{2.7}$$

Following the assumptions on the displacement field, three compatibility equations are satisfied. The remaining equations are recalled here, as they can be used to determine the form of the displacement components $v(r, z)$ and $w(r, z)$ (Hyer and Rousseau, 1987; Tutuncu and Winckler, 1993):

$$\frac{d^2\varepsilon_{zz}}{dr^2} = 0, \qquad \frac{1}{r}\frac{d\varepsilon_{zz}}{dr} = 0, \qquad \frac{d}{dr}\left[\frac{1}{r}\frac{d}{dr}(r\gamma_{\theta z})\right] = 0. \tag{2.8}$$

The constitutive equations for a general orthotropic k^{th} layer of the

laminate take the following form:

$$\begin{Bmatrix} \sigma_{rr} \\ \sigma_{\theta\theta} \\ \sigma_{zz} \\ \sigma_{r\theta} \\ \sigma_{rz} \\ \sigma_{\theta z} \end{Bmatrix} = \begin{bmatrix} C_{rrrr} & C_{rr\theta\theta} & C_{rrzz} & 0 & 0 & C_{rr\theta z} \\ C_{rr\theta\theta} & C_{\theta\theta\theta\theta} & C_{\theta\theta zz} & 0 & 0 & C_{\theta\theta\theta z} \\ C_{rrzz} & C_{\theta\theta zz} & C_{zzzz} & 0 & 0 & C_{zz\theta z} \\ 0 & 0 & 0 & C_{r\theta r\theta} & C_{r\theta rz} & 0 \\ 0 & 0 & 0 & C_{r\theta rz} & C_{rzrz} & 0 \\ C_{rr\theta z} & C_{\theta\theta\theta z} & C_{zz\theta z} & 0 & 0 & C_{\theta z\theta z} \end{bmatrix} \begin{Bmatrix} \varepsilon_{rr} - \alpha_{rr}\Delta T \\ \varepsilon_{\theta\theta} - \alpha_{\theta\theta}\Delta T \\ \varepsilon_{zz} - \alpha_{zz}\Delta T \\ \gamma_{r\theta} \\ \gamma_{rz} \\ \gamma_{\theta z} - \alpha_{\theta z}\Delta T \end{Bmatrix}. \tag{2.9}$$

The C_{ijkl} define the terms of the stiffness matrix in the cylindrical basis $(\hat{e}_r, \hat{e}_\theta, \hat{e}_z)$ associated to the structure, hence they are function of the behavior in the material basis $(\hat{e}_1, \hat{e}_2, \hat{e}_3)$, as well as of the orientation angle of the fibers (the angle φ in Figure (2.2)). The α_{ij} are the coefficients of thermal expansion of the material in the cylindrical basis.

The equilibrium equations without body forces read:

$$\nabla \cdot \boldsymbol{\sigma} = \mathbf{0}, \tag{2.10}$$

and in cylindrical coordinates, taking into account the assumptions (Hyer and Rousseau, 1987; Lubarda and Lubarda, 2020):

$$\begin{aligned} \frac{d\sigma_{rr}}{dr} + \frac{\sigma_{rr} - \sigma_{\theta\theta}}{r} &= 0, \\ \frac{d\sigma_{r\theta}}{dr} + \frac{2\sigma_{r\theta}}{r} &= 0, \\ \frac{d\sigma_{rz}}{dr} + \frac{\sigma_{rz}}{r} &= 0. \end{aligned} \tag{2.11}$$

Assuming a composite tube with unloaded inner (R_{in}) and outer (R_{out}) surfaces (with no mandrel at the inner surface of the tube), we have the following boundary conditions:

$$\begin{aligned} \sigma^1_{rr}(R_{in}) = \sigma^1_{r\theta}(R_{in}) = \sigma^1_{rz}(R_{in}) = 0 \\ \sigma^N_{rr}(R_{out}) = \sigma^N_{r\theta}(R_{out}) = \sigma^N_{rz}(R_{out}) = 0, \end{aligned} \tag{2.12}$$

where 1 is the first (innermost) layer and N is the last (outermost) layer (see Figure (2.2)).

Assuming an axially and torque unloaded tube, the remaining boundary conditions can be written in integral form as follows:

$$\begin{aligned} 2\pi \sum_{k=1}^{N} \int_{r_k}^{r_{k+1}} \sigma^{(k)}_{zz}(r) r dr = 0 \\ 2\pi \sum_{k=1}^{N} \int_{r_k}^{r_{k+1}} \sigma^{(k)}_{\theta z}(r) r^2 dr = 0. \end{aligned} \tag{2.13}$$

To reestablish continuity and equilibrium between layers, further conditions must be satisfied at the interfaces between layers. For the stresses:

$$\left.\begin{aligned}\sigma_{rr}^{(k)}(r_k) &= \sigma_{rr}^{(k+1)}(r_k)\\ \sigma_{r\theta}^{(k)}(r_k) &= \sigma_{r\theta}^{(k+1)}(r_k)\\ \sigma_{rz}^{(k)}(r_k) &= \sigma_{rz}^{(k+1)}(r_k)\end{aligned}\right\} k = 1, 2, ..., N-1, \tag{2.14}$$

and for the displacements:

$$\left.\begin{aligned}u^{(k)}(r_k) &= u^{(k+1)}(r_k)\\ v^{(k)}(r_k, z) &= v^{(k+1)}(r_k, z)\\ w^{(k)}(r_k, z) &= w^{(k+1)}(r_k, z)\end{aligned}\right\} k = 1, 2, ..., N-1, \tag{2.15}$$

where r_k is the radial coordinate of the interface between layers k and $k+1$ (see Figure (2.2)).

Solution: displacement field for each layer

The main points of the solution are recalled here, for more details see the papers by (Hyer et al., 1986; Tutuncu and Winckler, 1993).

The second and third equilibrium equations, from Eq. (2.11), together with the associated boundary and continuity conditions, from Eqs. (2.12) and (2.14), lead to $\sigma_{r\theta} = \sigma_{rz} = 0$ everywhere in the laminate.

Compatibility relations, Eq. (2.8), together with the associated continuity conditions, from Eq. (2.15), enable us to find the following form of the displacement components $v(r, z)$ and $w(r, z)$:

$$\begin{aligned}v(r, z) &= A_1 z r,\\ w(z) &= A_2 z,\end{aligned} \tag{2.16}$$

where A_1 and A_2 are two integration constants.

Finally, the first of the equilibrium equations (2.11) can be integrated to determine $u(r)$:

$$\begin{aligned}u^{(k)}(r) = &\frac{\left(C_{\theta\theta z}^{(k)} - 2C_{rr\theta z}^{(k)}\right) A_1}{4C_{rrrr}^{(k)} - C_{\theta\theta\theta\theta}^{(k)}} r^{2(k)} + \frac{\left(C_{\theta\theta zz}^{(k)} - C_{rrzz}^{(k)}\right) A_2}{C_{rrrr}^{(k)} - C_{\theta\theta\theta\theta}^{(k)}} r^{(k)} +\\ &+ \frac{\Sigma^{(k)}}{C_{rrrr}^{(k)} - C_{\theta\theta\theta\theta}^{(k)}} r^{(k)} + B_2^{(k)} r^{-\lambda(k)} + B_1^{(k)} r^{\lambda(k)},\end{aligned} \tag{2.17}$$

where the following constants have been redefined to simplify the ex-

pressions (Hyer and Rousseau, 1987):

$$\Sigma^{(k)} = \Bigg[\left(C^{(k)}_{rrzz} - C^{(k)}_{\theta\theta zz}\right)\alpha^{(k)}_{zz} + \left(C^{(k)}_{rr\theta\theta} - C^{(k)}_{\theta\theta\theta\theta}\right)\alpha^{(k)}_{\theta\theta} + \\ + \left(C^{(k)}_{rrrr} - C^{(k)}_{rr\theta\theta}\right)\alpha^{(k)}_{rr} + \left(C^{(k)}_{rr\theta z} - C^{(k)}_{\theta\theta\theta z}\right)\alpha^{(k)}_{\theta z}\Bigg]\Delta T, \tag{2.18}$$

$$\lambda^{(k)} = \sqrt{\frac{C^{(k)}_{\theta\theta\theta\theta}}{C^{(k)}_{rrrr}}}.$$

For a single composite cylinder layer, the number of unknown constants that have to be found are: A_1, A_2, B_1 and B_2. In general, for an N-layer cylinder there are $2N+2$ constants to be determined, which are: A_1, A_2, $B^{(1)}_1$, ..., $B^{(k)}_1$, ..., $B^{(N)}_1$ and $B^{(1)}_2$, ..., $B^{(k)}_2$, ..., $B^{(N)}_2$. The $2N+2$ constants can be determined using the 2 boundary and the $(N-1)$ continuity conditions on σ_{rr}, from Eqs. (2.12) and (2.14), as well as the $(N-1)$ continuity conditions on u_r, from Eq. (2.15), and the 2 integral boundary conditions, Eq. (2.13).

In particular, assuming a single composite layer cylindrical tube with the fibers oriented along the axial direction ($\varphi = 0°$ in Figure (2.2)), the constant $\lambda = 1$ and the radial displacement can be written as follows:

$$u^{(1)}(r) = B_1 r + \frac{B_2}{r}. \tag{2.19}$$

In this particular case, the thermal strain in the radial direction and the thermal strain in the circumferential direction are equal, since the circumferential direction is dominated by the matrix behavior. Therefore, residual thermal stresses do not appear in the tube.

Once the displacements solution is known, the strains and stresses everywhere in the tube can be computed from Eqs. (2.7) and (2.9). In particular, the circumferential stress $\sigma_{\theta\theta}$ distribution evaluated with the model can be used to assess its associated bending moment per unit width around the z-axis, with respect to the midsurface of the laminate at $R_m = (R_{in} + R_{out})/2$, as follows:

$$M_{\theta\theta} = \int_{-\frac{h_{tot}}{2}}^{+\frac{h_{tot}}{2}} \sigma_{\theta\theta} h dh, \tag{2.20}$$

where $h = r - R_m$ is the thickness coordinate and $h_{tot} = R_{out} - R_{in}$ is the total thickness of the tube. The bending moment $M_{\theta\theta}$ represents the constraint reaction in the circumferential direction of the tube due to the material continuity. Therefore, interrupting the material continuity,

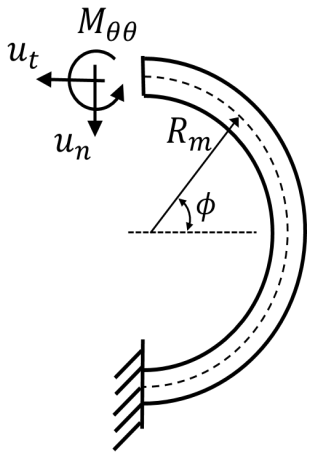

Figure 2.3: Curved beam model. The mean radius R_m and the angle ϕ indicate a general point along the curved beam. The normal and the tangent displacements are indicated respectively with u_n and u_t. The concentrated bending moment $M_{\theta\theta}$ is applied on the free edge of the curved beam. The other edge of the curved beam is clamped.

for example cutting the tube axially (Eduljee and Gillespie, 1996; Casari et al., 2006; Di Gennaro et al., 2021), results in releasing residual stresses and inducing geometrical distortions. The deformation induced in the tube after axial cut by the bending moment in the circumferential direction is either closure or an opening, and it enables us to quantify indirectly the residual stresses trapped in the tube.

2.3.2 . Opening and closing of tubes: curved beam model

A curved beam model, representing half of the cross-section of the tube after the cut, was used to assess analytically the displacements induced by the bending moments associated to the residual stresses. The curved beam modelled is shown in Figure (2.3). One end of the beam is clamped to simulate the material continuity of the tube, and on the other one a concentrated bending moment is applied.

Indicating with s the curvilinear abscissa, with u_n and u_t respectively the normal and the tangent displacements, ω the rotation and the R_m mean radius, the strains can be written as follows:

$$\begin{cases} \varepsilon = \dfrac{du_t}{ds} - \dfrac{u_n}{R_m} = u_t' - \dfrac{u_n}{R_m} \\ \gamma = \dfrac{du_n}{ds} + \dfrac{u_t}{R_m} - \omega = u_n' + \dfrac{u_t}{R_m} - \omega \\ \chi = \dfrac{d\omega}{ds} = \omega' \end{cases} \tag{2.21}$$

where ε is the axial strain of the beam, γ is the shear strain, χ is the bending strain and $\frac{d\bullet}{ds} = \bullet'$ is the derivative with respect the curvilinear abscissa.

Since the curvature of the curved beam is low ($\frac{1}{R_m} << 1$), then the constitutive equation of the layered plate can be considered as follows (Reddy, 2004):

$$\boldsymbol{D} = \sum_{k=1}^{N} \int_{h_k}^{h_{k+1}} h^2 \boldsymbol{C}_p dh, \tag{2.22}$$

where h is the thickness coordinate and $\boldsymbol{C}_p$ is the stiffness matrix of the laminate plate in plane stress in the cylindrical frame. Since the curved beam represents half of the tube cross-section after cutting, based on the generalized plane strain hypothesis in the $\hat{e}_z$ direction the curvatures $\chi_{zz} = \chi_{rz} = 0$. The constitutive relation linking the moment and the curvature in the $\theta\theta$ direction is therefore

$$M = D_{\theta\theta\theta\theta}\chi. \tag{2.23}$$

The equilibrium equations are:

$$\begin{cases} N' - \dfrac{T}{R_m} + q^* = 0 \\ T' + \dfrac{N}{R_m} + p^* = 0 \\ M' + T + m^* = 0 \end{cases} \tag{2.24}$$

In the present case q^*, p^* and m^* are respectively the normal, tangent and bending distributed loads which are null.

Following the slender beam hypothesis (Euler-Bernoulli hypothesis) where the shear deformation is $\gamma = 0$, and the inextensibility hypothesis $\varepsilon = 0$, we have:

$$\omega' = u_n'' + \frac{u_t'}{R_m} = R_m u_t''' + \frac{u_t'}{R_m} \tag{2.25}$$

Applying Equation (2.23) to Equation (2.25), we have:

$$R_m u_t''' + \frac{u_t'}{R_m} = \frac{M}{D_{\theta\theta\theta\theta}}. \tag{2.26}$$

The third of Equation 2.24 can be solved imposing as boundary condition on the free edge of the curved beam (see Figure (2.3)) the bending moment assessed analytically with Equation (2.20) in Section 2.4.1, with the sign inverted. The displacements are then found solving Equation (2.26).

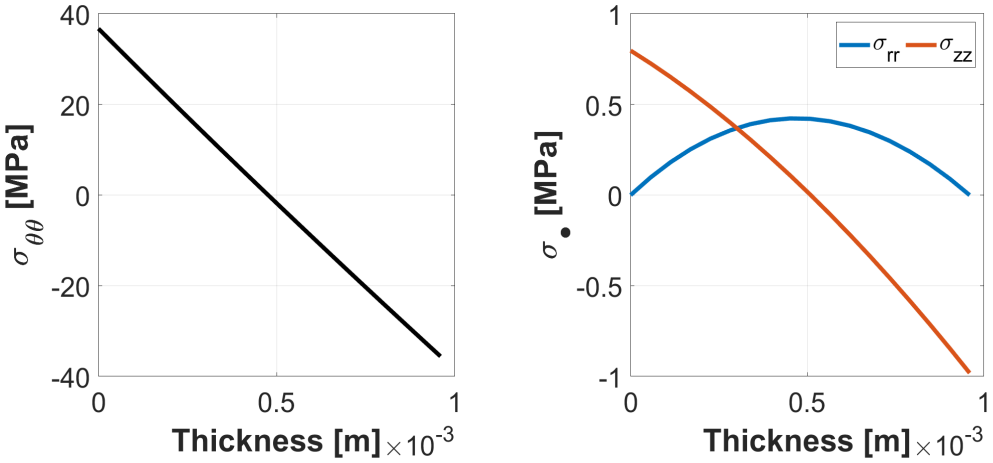

Figure 2.4: Circumferential (left), radial and axial stresses distributions (right) through the thickness of a unconstrained $[90°]$ tube subjected to a uniform temperature difference ($\Delta T = -400°$C) assessed by the analytical structural model. Thickness$= 0$ m is the innermost layer of the tube.

2.3.3 . Residual stresses and geometrical distortion in a unconstrained unidirectional composite tube

In the present Section, we used the analytical model presented in Section 2.3.1 to assess the thermal stresses induced in a unconstrained unidirectional composite tube of internal radius R_{in} and total thickness h_{tot} with stacking sequence $[90°]$, that is the fibers oriented along the circumferential direction, subjected to a uniform temperature difference ΔT. The resultant bending moment is used in the curved beam model, presented in Section 2.3.2, to assess the opening or closure of the tube.

The geometrical and loading parameters are: $R_{in} = 20$ mm, $h_{tot} = 0.96$ mm and $\Delta T = -400°$C.

The material considered is Carbon/PEEK and the elastic material parameters are the following (Grogan et al., 2015):

$$E_L = 134 \text{ GPa}, \quad E_T = 10.3 \text{ GPa}, \quad \mu_L = 6 \text{ GPa}, \quad \nu_{LT} = 0.32, \quad \nu_{TT} = 0.4.$$

The coefficients of thermal expansion used are (Grogan et al., 2015):

$$\alpha_1 = 0.2(10^{-6})/°\text{C}, \quad \alpha_2 = 28.8(10^{-6})/°\text{C}.$$

The radial (σ_{rr}), circumferential ($\sigma_{\theta\theta}$) and axial (σ_{zz}) stresses along the thickness of the tube are depicted in Figure (2.4), while the shear stress ($\sigma_{\theta z}$) is obviously null.

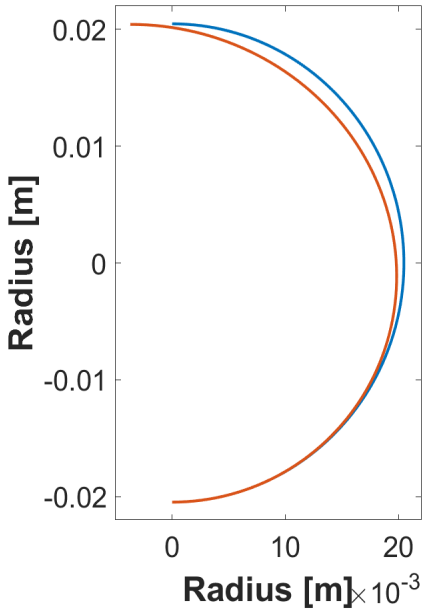

Figure 2.5: Curved beam of the $[90°]$ tube subjected to a constant temperature difference $\Delta T = -400°$C. The blue line represents the initial configurations and the red line the deformed configuration. A deformation scale factor of 5 is used.

The radial and the axial stresses induced in the tube by the constant temperature difference input are negligible compared to the circumferential stress. Specifically, the radial stresses at the inner and at the outer surfaces of the tube are null based on Equation (2.12) (the two external surfaces of the tube are unloaded). The bending moment associated to $\sigma_{\theta\theta}$ is reported in Table (2.1).

Applying the bending moment in Table (2.1) with the opposite sign to the curved beam model induces the deformation depicted in Figure (2.5). The free end of the curved beam where the bending moment was applied (see Figure (2.3)) represents the point where the tube was cut. Thus, the deformation in Figure (2.5) shows that the tube is closing. The displacement that would be measured on the tube, reported in Table (2.1), is obtained multiplying by two the tangent displacement u_t on the free edge of the beam where the concentrated bending moment is applied (see Figure (2.3)).

The structural model presented here addressed the combined effect of the geometry and the anisotropy of the composite tube subjected to a uniform temperature difference, neglecting the effects of the temperature gradients. In this scenario, the circumferential stress assessed with this model induces the closure of the tube.

Table 2.1: Bending moments associated to the circumferential stresses distributions assessed through the analytical structural model, and the circumferential relative displacements assessed using the curved beam model for the $[90°]$ stacking sequence.

Tube	ΔT [°C]	Bending moment [N m/m]	Analytical circ. rel. disp. [mm]
$[90°]$	-400	-5.5864	-1.48

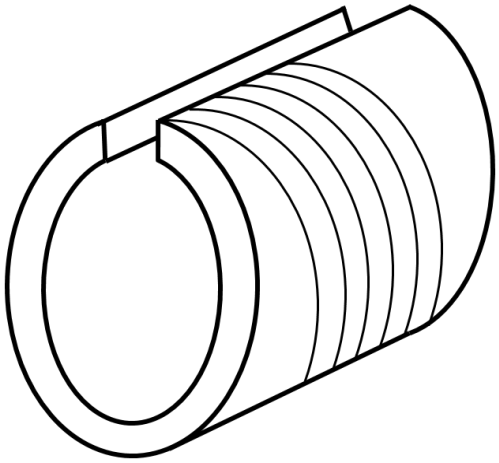

Figure 2.6: Axially cut tube before deformation occurs.

2.4 . Evaluation of residual stresses in tubes with different stacking sequences

2.4.1 . Experimental results

The CETIM manufactured several tubes of thermoplastic matrix composite material (carbon/PEEK) using the LATP manufacturing process with two different mandrel temperatures. In one case tubes were manufactured winding the composite tapes around a cold mandrel ($T^{mand} = 20°$C), in the other case tubes were manufactured using a hot mandrel ($T^{mand} = 180°$C). The main consequence of the two different mandrel temperatures lies on the induced temperature gradients within the structure during the manufacturing process, therefore in the overall temperature history experienced by the composite structure. In particular, higher thermal gradients are expected in the manufacturing process with the cold mandrel.

The manufactured tubes are 0.96 mm thick, with an inner radius of $R_{in} = 20$ mm and 6 layers (each layer is 0.16 mm thick) with different stacking sequence: $[\pm 85°]_3$ and $[\pm 55°]_3$. After the specimens were manufactured, a cut along the axial direction was performed (see Fig-

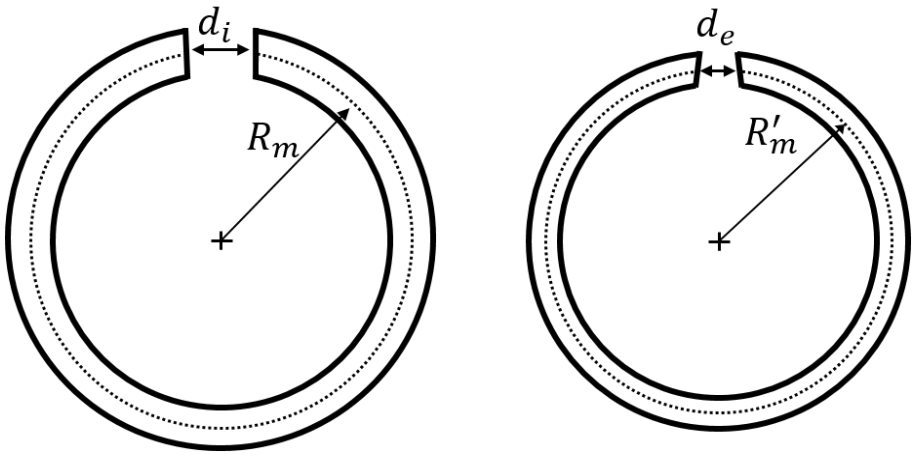

Figure 2.7: Cross-section of the cut tube before deformation occurs (left) where R_m is the mean radius and d_i is the initial circumferential width of the cut. Cross-section of the cut tube after deformation occurs (right) (closure of the tube) where $R_m^{'}$ is the new mean radius and d_e is the final circumferential width of the cut.

Table 2.2: Experimental measurements of the circumferential relative displacements for the $[\pm 85^\circ]_3$ and $[\pm 55^\circ]_3$ tubes manufactured using hot and cold mandrels. The initial axial cut width is $d_i = 3.4$ mm. The initial offset is 0 mm.

Tube	Manufacturing process	Circ. rel. disp. [mm]	Twist offset [mm]
$[\pm 85^\circ]_3$	Hot mandrel	-2.70	1.35
$[\pm 85^\circ]_3$	Cold mandrel	-2.86	0.21
$[\pm 55^\circ]_3$	Hot mandrel	-0.95	2.93
$[\pm 55^\circ]_3$	Cold mandrel	1.81	1.50

ure (2.6)) and the opening/closure (see Figure (2.7) right) and twisting (see Figure (2.8) right) displacements were measured in order to indirectly quantify the residual stresses due to manufacturing.

The initial cut width is $d_{in} = 3.4$ mm (see Figure (2.7) left) and the experimental measurements are detailed in Table (2.2). The circumferential relative displacements reported in the tables are the differences between the final cut widths and the initial cut width ($d_e - d_i$, see Figure (2.7)).

A negative experimental result for the circumferential relative displacement (see Table (2.2)) corresponds to the closing of the tube, while a positive one corresponds to the opening of the tube. The experimental twist offset is measured through the axial offset between the free edges of the tube after the axial cut (see Figure (2.8) right).

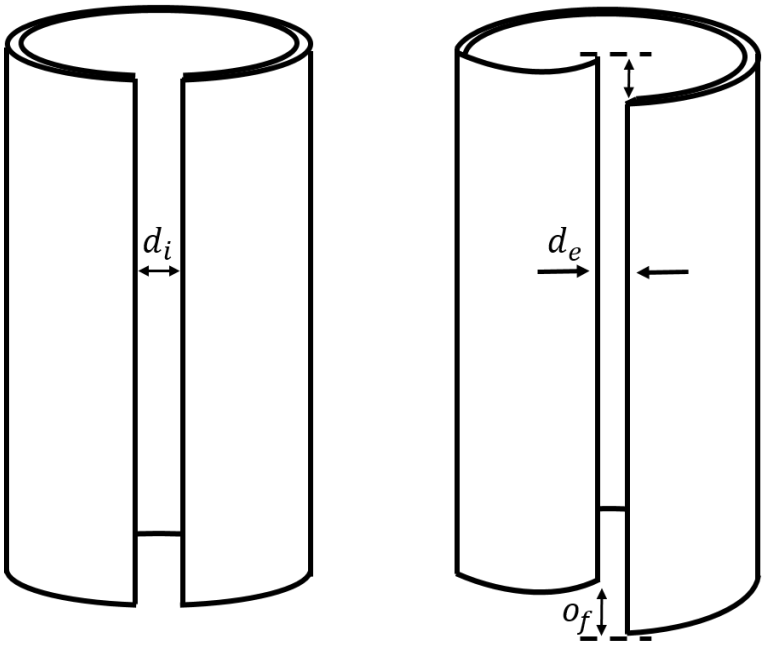

Figure 2.8: Initial configuration of the cut tube, where d_i is the initial circumferential width of the cut (left). Final configuration of the tube after deformation occurs, where d_e is the final circumferential width of the cut and o_f is the twist offset (right).

In the present Section, we focused on the tubes responses in the circumferential direction. As can be noticed from Table (2.2), the $[\pm 85°]_3$ tubes manufactured using both hot and cold mandrel, after the axial cutting process, experience a closure. On the other hand, the $[\pm 55°]_3$ tube manufactured using hot mandrel shows a closure, while the same tube using the cold mandrel shows an opening. The completely different thermal histories induced by the hot and cold mandrel seem to have little, if no influence on the $[\pm 85°]_3$ tubes responses, while in the $[\pm 55°]_3$ the sign of the displacement and that of the bending moment associated to the residual stress, was inverted. This is related to the stacking sequence of the tubes: in $[\pm 85°]_3$ the circumferential direction is dominated by the fibers behavior while $[\pm 55°]_3$ is not, hence it is affected by the effects of the temperature gradients.

In the following Section, the residual stresses assessed with the structural model and the displacements assessed with the curved beam model for the $[\pm 85°]_3$ and $[\pm 55°]_3$ tubes are presented.

2.4.2 . Analytical results

The residual stresses distribution and the opening/closure of the tubes manufactured by CETIM were predicted here using the analyti-

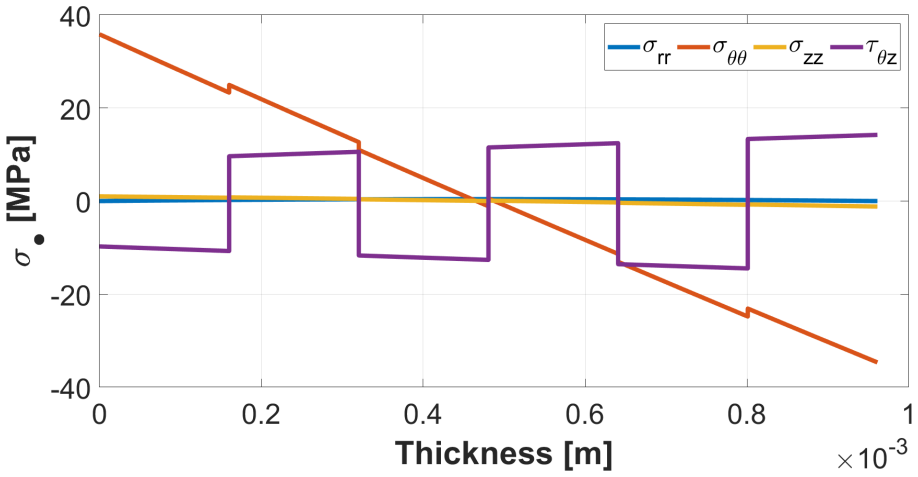

Figure 2.9: Radial, circumferential, axial and shear stresses distributions through the thickness of a unconstrained $[\pm 85°]_3$ tube subjected to a uniform cooling process ($\Delta T = -400°$C) assessed by the analytical structural model.

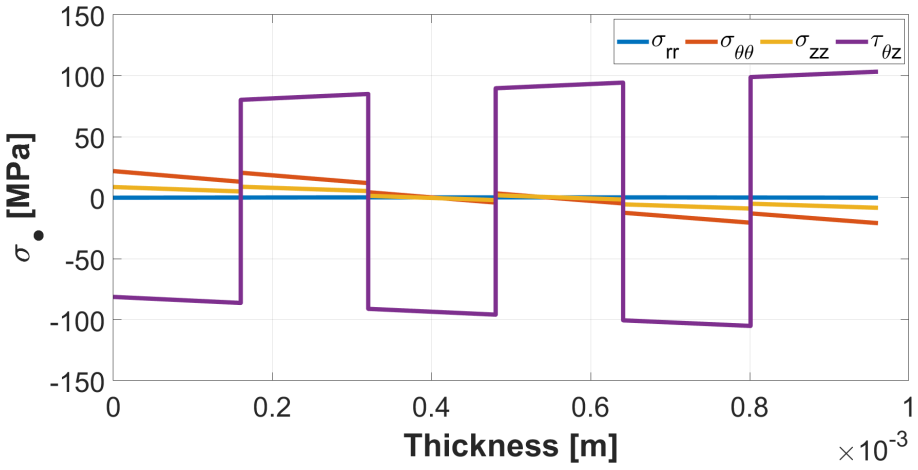

Figure 2.10: Radial, circumferential, axial and shear stresses distributions through the thickness of a unconstrained $[\pm 55°]_3$ tube subjected to a uniform cooling process ($\Delta T = -400°$C) assessed by the analytical structural model.

Table 2.3: Bending moments associated to the circumferential stresses distributions assessed through the analytical structural model for the $[90°]$, $[\pm 85°]_3$ and $[\pm 55°]_3$ tubes.

Tube	ΔT [°C]	Bending moment [N m/m]
$[90°]$	-400	-5.5864
$[\pm 85°]_3$	-400	-5.5683
$[\pm 55°]_3$	-400	-3.6284

cal model presented in Section 2.3 with a uniform temperature distribution $\Delta T = -400$°C. The results are depicted respectively in Figure (2.9) and in Figure (2.10).

As can be noticed, the circumferential stress $\sigma_{\theta\theta}$ in Figure (2.9) for the $[\pm 85°]_3$ tube is quite similar to the one presented in Figure (2.4) for the $[90°]$ tube, and it is the dominant term. Because of the stacking sequence of the $[\pm 85°]_3$ tube, a shear stress distribution ($\sigma_{\theta z}$) also appears. For the $[\pm 55°]_3$ tube, the shear stress distribution is the dominant one (see Figure (2.10)). The shear stress distribution justifies the presence of the twist offset after the axial cut of the tubes observed experimentally (see Table (2.2)).

The bending moments associated to the circumferential stress distributions in Figure (2.9) and in Figure (2.10) are assessed through Equation (2.20) and reported in Table (2.3).

After the suppression of the material continuity in the circumferential direction, the residual circumferential stresses are released and the bending moment causes the tube to close on itself. Based on the same principle, the shear stresses depicted in Figure (2.9) and in Figure (2.10) explain the twist offsets experienced by the tubes experimentally after the axial cut (see Table(2.2)).

The deformed configuration of the curved beams for the $[\pm 85°]_3$ and $[\pm 55°]_3$ tubes are depicted in Figure (2.11) left and right respectively. The bending moments applied (in Table (2.3)) are associated to the circumferential stress depicted in Figure (2.9) and in Figure (2.10) for the $[\pm 85°]_3$ and $[\pm 55°]_3$ respectively. The displacements are detailed in Table (2.4), where it appears evident that the analytical prediction in both cases is the tube closure. The structural model presented in Section 2.3 accounts for the combined effect of the geometry and the anisotropy using a uniform temperature difference as input. Therefore, we can conclude that the geometry and anisotropy of a composite tube under a uniform temperature difference induce closure after the axial cut.

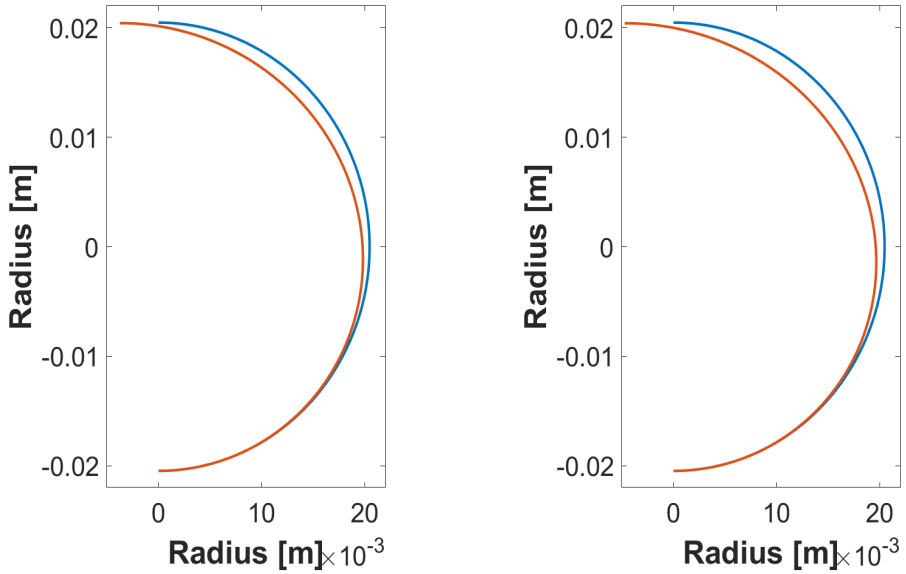

Figure 2.11: Curved beam model of the $[\pm 85°]_3$ (left) and $[\pm 55°]_3$ (right) cylindrical tubes subjected to a constant temperature difference $\Delta T = -400°$C. The blue line represents the initial configurations and the red line the deformed configuration. A deformation scale factor of 5 is used.

2.4.3 . Comparison between experimental and analytical results

Analytical results of the relative circumferential displacements were compared with experimental measurements for $[\pm 85°]_3$ and $[\pm 55°]_3$ tubes. Since in our discussion (up to now) the temperature gradients were neglected, the comparison was made between the curved beam results and the experimental measurements on the $[\pm 85°]_3$ and $[\pm 55°]_3$ tubes manufactured using a hot mandrel, where less severe thermal gradients are expected. The experimental and the analytical results are detailed in Table (2.4).

The combined effect of the geometry and anisotropy, presented in

Table 2.4: The circumferential relative displacements assessed using the curved beam model for the $[\pm 85°]_3$ and $[\pm 55°]_3$ tubes. The experimental circumferential displacements for the $[\pm 85°]_3$ and $[\pm 55°]_3$ tubes were also reported in the Table. The initial experimental axial cut width is $d_i = 3.4$ mm.

Tube	Analytical circ. rel. disp. [mm]	Exp. circ. rel. disp. [mm]
$[\pm 85°]_3$	-1.49	-2.70
$[\pm 55°]_3$	-1.89	-0.95

Section 2.2, with a uniform temperature difference $\Delta T = -400°$C induces the circumferential residual stress distributions depicted in Figure (2.9) for the $[\pm 85°]_3$ tube and in Figure (2.10) for the $[\pm 55°]_3$ tube which, when released by axial cutting of the tube tend to close the tube. Analytical results show the same trend (tubes closure) compared to experimental results in Table (2.4) for the $[\pm 85°]_3$ and $[\pm 55°]_3$ tubes manufactured using a hot mandrel.

The analytical displacement for the $[\pm 55°]_3$ in Table (2.4) shows that the tube closes more with respect to the experimental displacement. Here, the $[\pm 55°]_3$ tube is manufactured using a hot mandrel, where less severe temperature gradients are expected with respect to the cold mandrel processing. Therefore, the mismatch between the analytical and the experimental displacements for the $[\pm 55°]_3$ tube could be due to the visco-elastic constitutive behavior of the polymer matrix composite, that enables stresses relaxation at high temperature during manufacturing.

Experimental results (see Table (2.2)) show that the thermal gradients and the temperature history induced by the LATP manufacturing process with cold and hot mandrel have a not negligible effect on the resulting geometric distortions, and they need to be addressed in our discussion for a correct prediction of residual stresses and strains within the manufactured composite structure.

In order to consider the effect of temperature gradients, a temperature-dependent viscoelastic constitutive model was developed in Di Gennaro et al. (2021) and it is discussed in Chapter 3.

2.5 . Finite element composites modeling

The mechanism of the combined effect of the curved geometry of the structure and the anisotropy of the composite material on residual stresses, explained in Section 2.2, has important consequences in terms of finite element modeling.

The same simulation performed on the unidirectional composite tube with fibers oriented along the circumferential direction in Section 2.3.3 with the structural model is performed using the commercial finite element software Abaqus. The uniform temperature difference used is $\Delta T = -400°$C.

Two types of elements were used: solid shell elements (called Continuum Shell elements in Abaqus) and 3D volumetric elements (called 3D Stress elements in Abaqus). The results of these simulations are depicted in Figure (2.12) and in Figure (2.13) for the Abaqus color map.

As can be noticed from the results depicted in Figure (2.12) and in

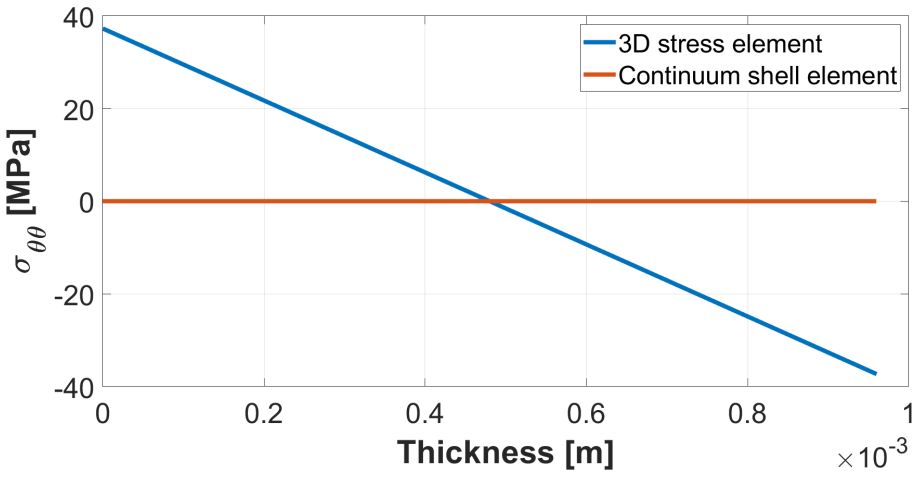

Figure 2.12: Circumferential stress distribution through the thickness of a unconstrained $[90°]$ tube subjected to a constant temperature difference ($\Delta T = -400°$C) assessed by the commercial Finite Element software Abaqus using 3D volumetric elements with quadratic shape functions (blue curve) and Continuum Shell elements (red curve).

Figure (2.13), the solid shell element, which is formulated on a volumetric support with only displacement degrees of freedom, but with underlying classical shell kinematics, is not able to assess residual stresses in this scenario. This is because one of the assumptions of the classical shell theory is that the transverse normal strain is null ($\varepsilon_{33} = 0$ with respect to the material basis), therefore the solid shell element is not able to take into account the effect of the curved geometry, which couples the in-plane kinematics with the out-plane kinematics of the tube (Section 2.2). Since the only cause which generates residual stresses in the unidirectional $[90°]$ tube subjected to a uniform temperature difference $\Delta T = -400°$C is the combined effect of the geometry and the anisotropy, the Abaqus finite element simulation performed with the solid shell element gives null residual stresses (see Figure (2.12) and Figure (2.13) left for the circumferential stress). The circumferential stress obtained by the FEM simulation with the 3D volumetric elements, depicted in Figure (2.12), is the same as the circumferential stress assessed with the structural model shown in Figure (2.4) left.

The inability of the shell model to correctly predict the stresses induced in a composite tube by free thermal expansion was initially highlighted by Whitney (1971). Other authors Reddy (1982); Barbero et al. (1990); Dicarlo et al. (2001) proposed solutions that provide an enrichment of the out-of-plane kinematics of the shell (modified shell model). These richer models are not available in Abaqus, and using them would

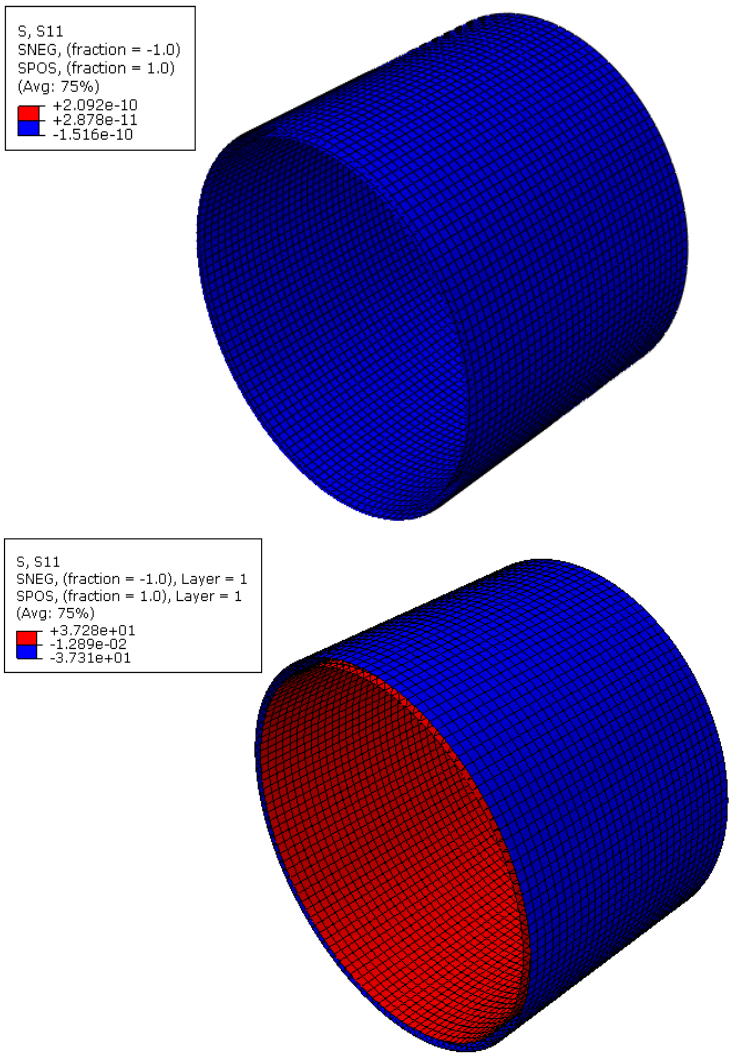

Figure 2.13: Abaqus color map of the circumferential stresses assessed on unconstrained $[90°]$ tube subjected to a uniform cooling process ($\Delta T = -400°$C) using a Continuum Shell element (left) and a 3D quadratic stress element (right).

require the implementation of a user element. As an alternative, the 3D volumetric elements predict correctly the stresses distributions (see Figure (2.12) and Figure (2.13) right), due to its complete kinematics description.

In other words, a uniform temperature difference is sufficient to rule out shell kinematics in this scenario. This is further justified in the presence of temperature gradients, therefore the 3D volumetric elements will be used in the following structural simulations.

Using one 3D volumetric element per ply may become too costly. Therefore, to overcome this problem, Abaqus proposes a way to model a composite laminate, called Composite Layup. In the next Section, this technique is explored.

2.5.1 . Abaqus composite modelling strategies

In the present Subsection, two composite laminate modelling strategies on Abaqus are addressed.

The first approach explored is to use one mesh element for each layer of the laminate, which is the classical modeling technique to describe composites in 3D. In order to do that, each layer of the composite laminate needs to be discretized, therefore the material parameters, the thickness and the fibers orientations need to be defined.

The second approach is the Abaqus Composite Layup option. This strategy, usually adopted in conjunction with shell elements, can also be applied to 3D volumetric elements as well within the Abaqus software. It enables us to use only one 3D volumetric element of the mesh in the structure's thickness, which contains all of the information about the stacking sequence of the laminate. Figure (2.14) shows the Abaqus Composite Layup option window, where the number of composite layers, the material, the relative thickness of each layer and the fibers angle can be defined. In particular, the whole composite laminate stacking sequence (shown here for a $[\pm 55°]_3$ composite tube) with its integration points is shown in Figure (2.15).

The two approaches discussed above were tested on a unconstrained $[\pm 55°]_3$ tube subjected to a uniform temperature difference ($\Delta T = -400°$C). The comparison between the two approaches is performed based on the shear stresses, since in this case are the dominant ones (see Figure (2.9) and Figure (2.10)). The shear stresses results for the simulation with the Composite Layup approach are depicted in Figure (2.16) left. The shear stresses results for the simulation with six 3D stress element in the thickness of the structure (one 3D stress element for each layer) are depicted in Figure (2.16) right. Results in both cases are exactly the same as those shown in Figure (2.10).

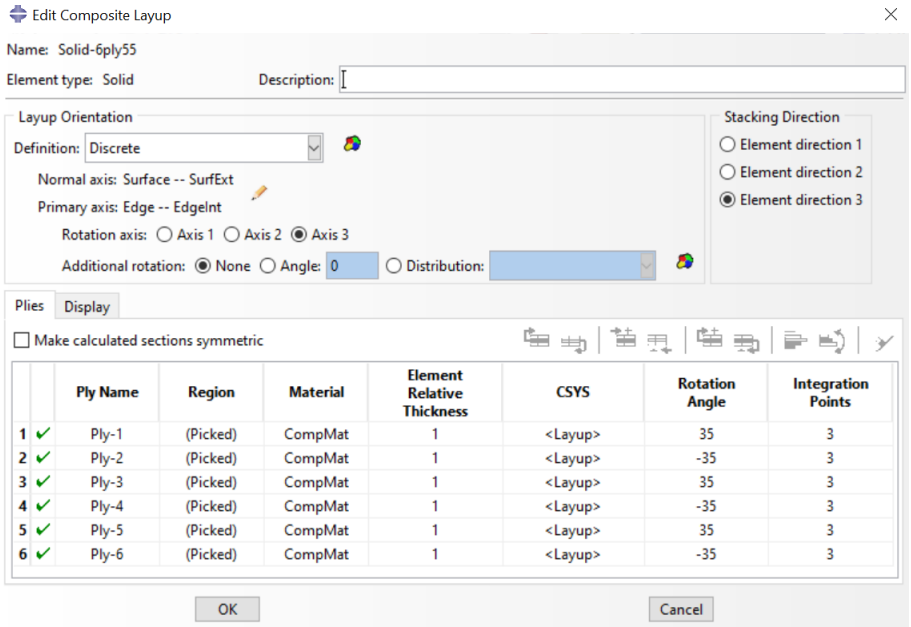

Figure 2.14: Abaqus composite layup window manager for the $[\pm 55°]_3$ tube. In the Material window are reported the elastic parameters of the composite material and its CTEs. The integration points for each structure layer is 3.

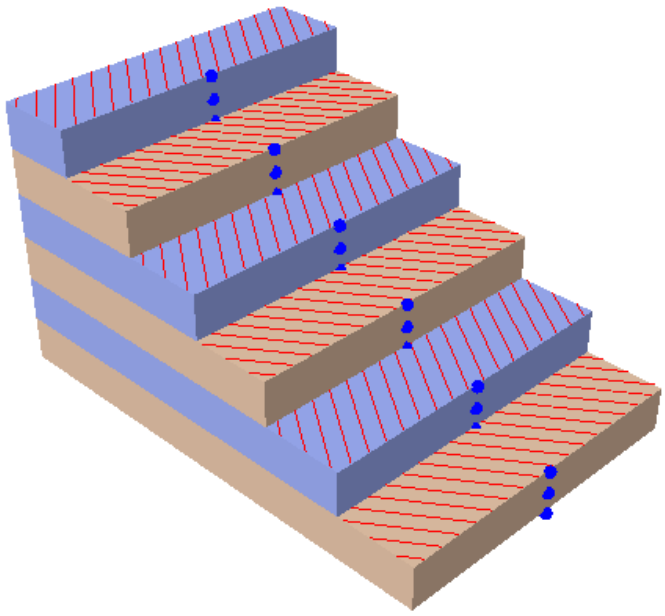

Figure 2.15: Abaqus Composite layup option orientations details. The integration points for each structure layer are highlighted.

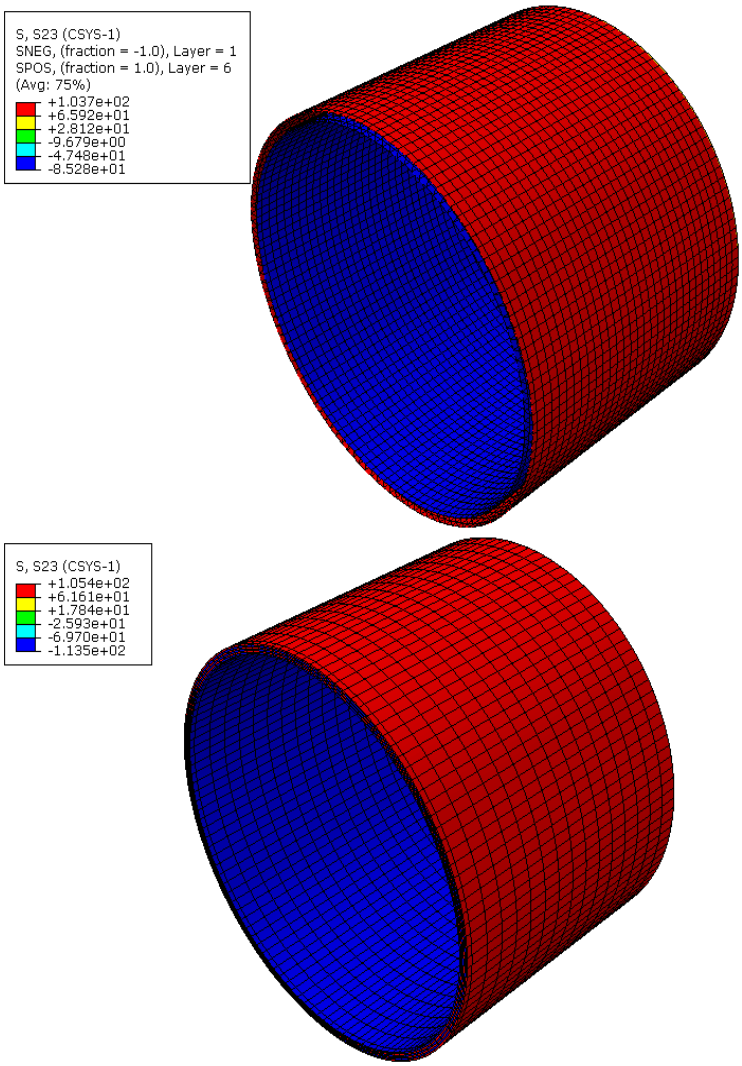

Figure 2.16: Abaqus color map of the shear stresses assessed on unconstrained $[\pm 55°]_3$ tube subjected to a uniform temperature difference ($\Delta T = -400°$C) using a single 3D quadratic Stress element in the structure thickness through a Composite Layup (left) and six 3D quadratic Stress elements (one element for each layer) in the structure thickness (right).

In this scenario, the two strategies give exactly the same results, therefore the most convenient choice in terms of calculation time and allocated space is the Composite Layup option, in which only one mesh element in the thickness is considered. One 3D volumetric mesh element in the structure thickness enables us to take into account the combined effect of the geometry and anisotropy presented in Section 2.2.

In the following discussion, a thermal model for the LATP manufacturing process is presented and used to perform thermo-mechanical structural simulations. Since the thermal model developed involves high temperature gradients, a better description in the thickness direction is required in order to predict correctly the thermal history effects on the simulated tubes. In principle, the problem could be solved using the Composite Layup option, which enables to control the number of integration points without changing the number of mesh elements in the structure. In this way, increasing the number of integration points and prescribing temperatures in each point would enable us to describe the high-temperature gradients involved in the LATP manufacturing. However, this strategy is not achievable since, according to the Abaqus Documentation (Aba, 2011), it does not seem possible to prescribe temperatures at the integration points. Hence, in the following thermo-mechanical structural simulations performed on Abaqus, one 3D volumetric element with quadratic shape functions for each composite layer is used.

2.6 . Conclusions

In the present Chapter, the combined effect of the curved geometry of the manufactured structure and the anisotropy of the composite material were taken into account for the prediction of residual stresses. The aim here was to evaluate and to show the relevancy of this particular incompatibility factor in terms of residual stresses and strains build-up in the composite structure. Furthermore, the consequences in terms of the composite modelling strategy on Abaqus were presented.

A non-plane structure subjected to a uniform temperature difference develops residual stresses since the curved geometry couples the in-plane kinematics with the out-of-plane kinematics. Indeed, in this scenario, the mismatch between the thermal strains in the two directions generates an incompatible thermal strain field, accommodated by residual stresses.

A structural model, already developed in the literature, was imple-

mented in order to assess residual stresses in a composite tube manufactured by the laser assisted tape placement. The complex thermal history and the temperature gradients were not taken into account in the present Chapter, therefore a simple constant temperature difference was used as input for the structural model. The CETIM manufactured several composite tubes with different stacking sequences using different process parameters: with a hot mandrel and with a cold mandrel. After the tubes were manufactured, the CETIM performed a cut along the axial direction of the tube in order to measure the residual strains, and from there find the residual stresses within the structure induced by the manufacturing process.

In order to assess the residual strains after the axial cut of the tube with the implemented model, the bending moment associated to the circumferential stress distribution induced by the constant temperature difference was computed. The deformations induced in the cut tube by the residual stresses were assessed by applying a concentrated bending moment on the free edge of a clamped curved beam.

The comparison between the experimental results and the model results showed the ability of the model in predicting tube closure after axial cutting of fabricated tubes with the hot mandrel. The $[\pm 55^\circ]_3$ tube manufactured by the LATP with the cold mandrel, on the other hand, opens instead of closing, showing the relevant effect of the thermal history and the temperature gradients induced by the manufacturing process, which needs to be take into account.

In order to take into account the combined effect of the geometry and the anisotropy in a finite element model, as pointed out also in the literature, solid shell elements cannot be used because of their lack of kinematics description in the out-of-plane direction, and the 3D volumetric elements are used here instead.

To conclude, two composite modelling strategies on the commercial finite element software Abaqus were addressed. The Composite Layup option allows to use one 3D volumetric element in the thickness direction of the structure, instead of one 3D volumetric element for each layer of the structure. In this sense, the first approach is convenient when only a constant temperature difference is used as input.

In the following Chapter, a mechanism-based temperature-dependent viscoelastic constitutive model suited for unidirectional fibers reinforced polymeric matrix composite is developed in order to take into account the severe temperature gradients induced in the structure thickness by the LATP manufacturing process. A transient thermal model for the LATP is developed in Chapter 4. For this reason, a better description of the temperature field in the thickness direction is mandatory,

and at least one 3D volumetric element with quadratic shape functions per layer is used in the following thermo-mechanical simulations on Abaqus presented in Chapter 5.

3 - A new mechanism-based temperature dependent viscoelastic model for unidirectional polymer matrix composites based on Cartan decomposition

A part of the present Chapter was published in Di Gennaro et al. (2021). As such, some of the text and figures are reproduced from that article.

3.1 . Introduction

The accurate prediction of residual stresses and strains in composite structures manufactured by modern and automated production techniques, like Laser Assisted Tape Placement (LATP), requires to properly account for the viscoelastic, temperature dependent behavior of the composite.

The Laser Assisted Tape Placement makes use of pre-impregnated tapes, containing long, oriented fibers embedded in a thermoplastic matrix: the basic building block of LATP structures is therefore a unidirectional fiber reinforced composite material. In particular, the fibers can be considered elastic and sustain most of the load, while the deviatoric response of the matrix is considered viscoelastic (Mallick, 2008; Ward and Sweeney, 2004; Simo and Hughes, 1998). Therefore, the mechanical properties are strongly direction dependent and, based on the material symmetries, a transversely isotropic behavior can be postulated. The goal of the present Chapter is to develop an original constitutive model for a viscoelastic, temperature dependent composite, in which the viscoelastic behavior of the composite is defined based on the underlying physical mechanism.

For isotropic material models, the viscoelastic relaxation is generally described with a set of scalar parameters, each associated to a different relaxation time (see for example Kaliske and Rothert (1997)). For anisotropic material models, and more specifically for fibre reinforced composites, a vast body of literature exists for both small strains (see for instance Zocher et al. (1997); Pettermann and DeSimone (2018); Kaliske (2000)) and finite strains regimes (for example Holzapfel and Gasser (2001); Nedjar (2007); Rajagopal and Wineman (2009); Balbi et al. (2018)). In many of these works, different relaxation functions (or a relaxation tensor) are introduced to describe the viscoelastic behavior

associated to each material parameter, without a clear link to the underlying physical mechanisms (as in Zocher et al. (1997); Pettermann and DeSimone (2018); Kaliske (2000)). In other approaches, in particular among the finite strains models, a formulation which aims at separating the fibers and the matrix contributions is introduced (Nedjar, 2007; Merodio and Ogden, 2005; Nedjar, 2011). The approach adopted in these references, however, is significantly different from the one proposed here, as it is discussed in the following.

The key element of the present work, discussed in Section 3.2, consists in defining an irreducible decomposition (Golubitsky et al., 1988) for the second order stress/strain tensors *before* defining the strain energy. An integrity basis for the energy function (Boehler, 1987) can then been extracted, yielding naturally uncoupled constitutive equations for each element of the decomposition. Thanks to this rigorous mathematical formulation, the contributions of two underlying constituents of the composite material (fibers and matrix) to each term of the constitutive behavior become easy to identify. In particular, the material parameters affected by the deviatoric response of the matrix are highlighted and assumed to be viscoelastic. This assumption is further justified in Section 3.3 through the analytical expressions presented by Hill (1964); Hashin and Rosen (1964); Hashin (1970a) of the elastic moduli for unidirectional fibers-reiforced composites.

A generalized Maxwell model can then be applied only to the appropriate terms of the stress/strain decomposition in order to describe the viscoelastic behavior of the composite in agreement with the underlying physical mechanism, as discussed in Section 3.4.

In order to account for the evolution of the viscoelastic behavior with temperature, the thermal strains and the time-temperature superposition principle are introduced in Section 3.5, under the hypothesis of thermorheologically simple materials (Lakes, 2009).

In Section 3.6, several numerical simulations are shown to highlight the key characteristics of the presented model. In particular, it is illustrated how the relaxation function associated to the transverse modulus of the composite is not an independent function, but it is related to the relaxation of the shear modulus in the plane of transverse isotropy. A user-material (UMAT) for the commercial finite element software Abaqus is developed in order to perform numerical simulations on structural parts.

Finally, in Section 3.7 conclusions and perspectives are discussed.

3.2 . Transversely isotropic elastic behavior based on Cartan decomposition

The key point of the proposed model consists in defining the transversely isotropic elastic behavior of a unidirectional composite ply in terms of elementary, uncoupled material parameters, which can be physically related to the material parameters of the two underlying constituents, the fibers and the matrix. As it is discussed in the following, these uncoupled parameters do not exactly correspond to the classically defined elastic constants E_L, E_T, μ_L, μ_T and ν_{LT}.

The key to the definition of such an uncoupled behavior is to derive the elastic fourth order tensor from a quadratic energy function, formulated in terms of an appropriate minimal integrity basis (Boehler, 1987). Such an integrity basis, in turn, is defined by finding an irreducible $\mathrm{O}(2)$ decomposition (Golubitsky et al., 1988) of the second order stress (and strain) tensor, where $\mathrm{O}(2)$ is the orthogonal group of the Euclidean plane, modeling the anisotropy.

The idea to use group representation theory (Fulton and Harris, 1991) and make an irreducible decomposition of the second order stress or strain tensor has already been used in the case of the cubic anisotropy (Desmorat and Marull, 2011; Desmorat et al., 2017; Mattiello et al., 2018; Bertram and Olschewski, 1996; Biegler and Mehrabadi, 1995). Furthermore, finding an explicit $\mathrm{O}(2)$ integrity basis can be straightforward using the recent publication (Desmorat et al., 2020), while some work was done in Ranaivomiarana (2019) about $\mathrm{O}(2)$ irreducible decomposition of strain tensor.

This rigorous mathematical formulation turns out to have deep physical significance, as it is discussed in the following. In particular, it enables us to clearly separate the material parameters which are influenced by the deviatoric response of the matrix and, as such, which should display a viscoelastic long term behavior, from those which should remain elastic throughout the analysis. This approach is radically different from the one adopted in many viscoelastic models for transversely isotropic materials (Zocher et al., 1997; Kaliske, 2000; Pettermann and DeSimone, 2018), which introduce different viscous relaxation functions for each of the classical elastic constants (E_L, E_T, μ_L, μ_T and ν_{LT}), with no clear link to the mechanical behavior of the underlying constituents. A similar, although not irreducible, decomposition of the stress (and strain) tensor, was proposed by Spencer (1984) and used to model the viscoelastic response of unidirectional plies by Nedjar (2011), but only partial uncoupling is achieved in that case.

Let us introduce the fibers' direction vector $\boldsymbol{v}_f$, defining the normal to the isotropic plane $(\boldsymbol{v}_2, \boldsymbol{v}_3)$. The transverse isotropy is then modelled

on the group generated by the rotations of axis $\boldsymbol{v}_f$, as well as the change of direction of $\boldsymbol{v}_f$ (equivalently the rotation of axis $\boldsymbol{v}_2$ and angle π). Such a group is in fact the group $\mathrm{O}(2)$ of orthogonal transformation of the plane $(\boldsymbol{v}_2, \boldsymbol{v}_3)$. An $\mathrm{O}(2)$ irreducible decomposition of the stress tensor, also known as a Cartan decomposition (Golubitsky et al., 1988), is for instance given as follows:

$$\boldsymbol{\sigma} = s_f \boldsymbol{M}_f + s_h \boldsymbol{M}_h + \boldsymbol{s}_{fs} + \boldsymbol{s}_d, \tag{3.1}$$

where

$$\begin{aligned} \boldsymbol{s}_{fs} &= s_{f2}\boldsymbol{M}_{f2} + s_{f3}\boldsymbol{M}_{f3}, \\ \boldsymbol{s}_d &= s_d \boldsymbol{M}_d + s_{23}\boldsymbol{M}_{23}, \end{aligned} \tag{3.2}$$

and the (unit) second order tensors $\boldsymbol{M}_\bullet$ are defined as

$$\begin{aligned} \boldsymbol{M}_f &= \boldsymbol{v}_f \otimes \boldsymbol{v}_f, \\ \boldsymbol{M}_h &= \frac{1}{\sqrt{2}} \left(\boldsymbol{v}_2 \otimes \boldsymbol{v}_2 + \boldsymbol{v}_3 \otimes \boldsymbol{v}_3 \right), \\ \boldsymbol{M}_{f2} &= \frac{1}{\sqrt{2}} \left(\boldsymbol{v}_f \otimes \boldsymbol{v}_2 + \boldsymbol{v}_2 \otimes \boldsymbol{v}_f \right), \\ \boldsymbol{M}_{f3} &= \frac{1}{\sqrt{2}} \left(\boldsymbol{v}_f \otimes \boldsymbol{v}_3 + \boldsymbol{v}_3 \otimes \boldsymbol{v}_f \right), \\ \boldsymbol{M}_d &= \frac{1}{\sqrt{2}} \left(\boldsymbol{v}_2 \otimes \boldsymbol{v}_2 - \boldsymbol{v}_3 \otimes \boldsymbol{v}_3 \right), \\ \boldsymbol{M}_{23} &= \frac{1}{\sqrt{2}} \left(\boldsymbol{v}_2 \otimes \boldsymbol{v}_3 + \boldsymbol{v}_3 \otimes \boldsymbol{v}_2 \right). \end{aligned} \tag{3.3}$$

These tensors are orthogonal and of unit length with respect to the scalar product $\boldsymbol{A} : \boldsymbol{B} = A_{ij}B_{ij}$, that is $\boldsymbol{M}_\bullet : \boldsymbol{M}_\circ = 0$ if $\boldsymbol{M}_\bullet \neq \boldsymbol{M}_\circ$, $\boldsymbol{M}_\bullet : \boldsymbol{M}_\bullet = 1$.

In the specific case when the vectors $\boldsymbol{v}_i$ are aligned with the standard basis vectors in Cartesian coordinates $\{\boldsymbol{v}_f = \boldsymbol{e}_1, \boldsymbol{v}_2 = \boldsymbol{e}_2, \boldsymbol{v}_3 = \boldsymbol{e}_3\}$, the stress components introduced in Eqs. (3.1) and (3.2) can be written as follows:

$$\begin{gathered} s_f = \sigma_{11}, \quad s_h = \frac{\sqrt{2}}{2} \left(\sigma_{22} + \sigma_{33} \right), \quad s_d = \frac{\sqrt{2}}{2} \left(\sigma_{22} - \sigma_{33} \right), \\ s_{f2} = \sqrt{2}\sigma_{12}, \quad s_{f3} = \sqrt{2}\sigma_{13}, \quad s_{23} = \sqrt{2}\sigma_{23}. \end{gathered} \tag{3.4}$$

It can be verified that the elements defined in the decomposition Eq. (3.1) are stable, that is they remain in the same space when subjected

to operations belonging to the group. Indeed, we have for a rotation of axis $\boldsymbol{v}_f$ and angle θ:

$$
\begin{aligned}
&s_f \boldsymbol{M}_f + s_h \boldsymbol{M}_h \mapsto s_f \boldsymbol{M}_f + s_h \boldsymbol{M}_h, \\
&s_{f2} \boldsymbol{M}_{f2} + s_{f3} \boldsymbol{M}_{f3} \mapsto (\cos(\theta) s_{f2} - \sin(\theta) s_{f3}) \boldsymbol{M}_{f2} + (\sin(\theta) s_{f2} + \cos(\theta) s_{f3}) \boldsymbol{M}_{f3}, \\
&s_d \boldsymbol{M}_d + s_{23} \boldsymbol{M}_{23} \mapsto (\cos(2\theta) s_d - \sin(2\theta) s_{23}) \boldsymbol{M}_d + (\sin(2\theta) s_d + \cos(2\theta) s_{23}) \boldsymbol{M}_{23}.
\end{aligned}
\tag{3.5}
$$

Such a decomposition of the stress tensor is far from being unique. Indeed, any invertible linear combination

$$
(\boldsymbol{M}_f, \boldsymbol{M}_h) \mapsto \alpha \boldsymbol{M}_f + \beta \boldsymbol{M}_h \tag{3.6}
$$

leads to another Cartan decomposition of $\boldsymbol{\sigma}$. The specific decomposition chosen here is related to the physical interpretation of the obtained components, which is quite straightforward. Two of the four terms involve the $\boldsymbol{v}_f$ direction, namely s_f (normal stress in the fibers' direction) and $\boldsymbol{s}_{fs}$ (longitudinal shear stresses s_{fi}). The other two, s_h and $\boldsymbol{s}_d$, involve only the plane of transverse isotropy, and they are analogous to the classical hydrostatic/deviatoric decomposition in two dimensions. Since the tensors $\boldsymbol{M}_\bullet$ are orthogonal and of unit length by construction, each term $s_\bullet$ of the decomposition can be extracted from the complete tensor $\boldsymbol{\sigma}$ as $s_\bullet = \boldsymbol{\sigma} : \boldsymbol{M}_\bullet$.

From a direct application of Desmorat et al. (2020), an $\mathrm{O}(2)$ integrity basis of $\boldsymbol{\sigma}$ is given by the 5 polynomials

$$
I_1 := s_f, \quad J_1 := s_h, \quad I_2 := \|\boldsymbol{s}_{fs}\|^2, \quad J_2 := \|\boldsymbol{s}_d\|^2, \quad I_3 := \mathrm{tr}\left(\boldsymbol{s}_{fs}^2 \boldsymbol{s}_d\right), \tag{3.7}
$$

meaning that any $\mathrm{O}(2)$ polynomial invariant I can be written as $I = p(I_1, J_1, I_2, J_2, I_3)$, with some polynomial p (see Boehler (1987) for more details on integrity bases). It is important to notice that the invariants obtained from the Cartan decomposition are significantly different from those classically considered in mechanics for transversely isotropic materials (Spencer, 1984; Kaliske, 2000; Holzapfel and Gasser, 2001; Merodio and Ogden, 2005; Nedjar, 2007):

$$
\begin{aligned}
&\bar{I}_1 = \mathrm{tr}\, \boldsymbol{\sigma}, \quad \bar{I}_2 = \frac{1}{2}\left(\bar{I}_1^2 - \mathrm{tr}\, \boldsymbol{\sigma}^2\right), \quad \bar{I}_3 = \det \boldsymbol{\sigma}, \\
&\bar{I}_4 = \mathrm{tr}\, \left(\boldsymbol{M}_f \boldsymbol{\sigma}\right), \quad \bar{I}_5 = \mathrm{tr}\, \left(\boldsymbol{M}_f \boldsymbol{\sigma}^2\right)
\end{aligned}
\tag{3.8}
$$

which are obtained by considering the set of isotropic invariants $\left(\bar{I}_1, \bar{I}_2, \bar{I}_3\right)$, and adding *a posteriori* the terms $\left(\bar{I}_4, \bar{I}_5\right)$ to account for transverse isotropy. Using a different set of invariants results in a different choice of elastic parameters, which constitutes the originality of this formulation

with respect to the existing literature. The relations between these two sets of invariants are given here:

$$
\begin{aligned}
&I_1 = \bar{I}_4, \quad J_1 = \frac{\bar{I}_1 - \bar{I}_4}{\sqrt{2}}, \\
&I_2 = 2\left(\bar{I}_5 - \bar{I}_4^2\right), \quad J_2 = \frac{1}{2}\left(\bar{I}_1^2 + 2\bar{I}_1\bar{I}_4 - 4\bar{I}_2 + \bar{I}_4^2 - 4\bar{I}_5\right) \\
&I_3 = \frac{1}{2}\left(2\bar{I}_3 - 2\bar{I}_2\bar{I}_4 + \bar{I}_1\bar{I}_4^2 + \bar{I}_4^3 + \bar{I}_1\bar{I}_5 - 3\bar{I}_4\bar{I}_5\right)
\end{aligned} \tag{3.9}
$$

The Gibbs free energy leading to linear elasticity can be defined using the 5 polynomial invariants introduced in Eq. (3.7):

$$
I_1^2 = s_f^2, \quad I_1 J_1 = s_f s_h, \quad J_1^2 = s_h^2, \quad I_2 = \|\boldsymbol{s}_{fs}\|^2, \quad J_2 = \|\boldsymbol{s}_d\|^2, \tag{3.10}
$$

so it can be written as:

$$
\begin{aligned}
\bar{w} &= \frac{1}{2}S_F s_f^2 + S_{FH} s_f s_h + \frac{1}{2}S_H s_h^2 + \frac{1}{2\mu_L}\left|\left|\boldsymbol{s}_{fs}\right|\right|^2 + \frac{1}{2\mu_T}\left|\left|\boldsymbol{s}_d\right|\right|^2 \\
&= \frac{1}{2}S_F s_f^2 + S_{FH} s_f s_h + \frac{1}{2}S_H s_h^2 + S_{FS}\left|\left|\boldsymbol{s}_{fs}\right|\right|^2 + S_D\left|\left|\boldsymbol{s}_d\right|\right|^2
\end{aligned} \tag{3.11}
$$

where S_F, S_{FH}, S_H, S_{FS} and S_D are the new five elementary material parameters which define the transversely isotropic elastic behavior.

Knowing the Gibbs free energy, the strain can be then computed as:

$$
\begin{aligned}
\boldsymbol{\varepsilon} = \frac{\partial \bar{w}}{\partial \boldsymbol{\sigma}} &= \left(S_F s_f + S_{FH} s_h\right)\boldsymbol{M}_f + \left(S_{FH} s_f + S_H s_h\right)\boldsymbol{M}_h + S_{FS}\boldsymbol{s}_{fs} + S_D\boldsymbol{s}_d \\
&= e_f \boldsymbol{M}_f + e_h \boldsymbol{M}_h + \boldsymbol{e}_{fs} + \boldsymbol{e}_d.
\end{aligned} \tag{3.12}
$$

As expected, the strain can also be set in terms of the Cartan decomposition.

The constitutive relations can finally be written as

$$
\begin{aligned}
\begin{bmatrix} e_f \\ e_h \end{bmatrix} &= \begin{bmatrix} S_F & S_{FH} \\ S_{FH} & S_H \end{bmatrix}\begin{bmatrix} s_f \\ s_h \end{bmatrix}, \\
\boldsymbol{e}_{fs} &= S_{FS}\boldsymbol{s}_{fs}, \\
\boldsymbol{e}_d &= S_D\boldsymbol{s}_d.
\end{aligned} \tag{3.13}
$$

The first of Eq. (3.13) involves the normal stresses/strains in the fibers' direction (s_f/e_f), as well as the hydrostatic part of the stresses and strains in the plane of transverse anisotropy (s_h/e_h). These terms are coupled by the material constant S_{FH}; while a different linear combination of s_f and s_h could be chosen to further uncouple these terms,

this is beyond the scope of this work. Physically, this part of the constitutive behavior is controlled by the fibers' elastic modulus, E_F, as well as by the bulk modulus of the polymer matrix, k_m. As E_f and k_m are generally considered elastic, the material constants S_F, S_{FH} and S_H are assumed as purely elastic in the following.

The second and third of Eq. (3.13) involve the longitudinal shear response of the composite, defined by the longitudinal shear modulus (indeed, we have $S_{FS} = 1/2\mu_L$), and its deviatoric response in the plane of transverse isotropy, defined by the transverse shear modulus (since $S_D = 1/2\mu_T$). These two parts of the composite's response are influenced by the deviatoric response of the polymer matrix, defined by its shear modulus μ_m. As the deviatoric response of the polymer is generally assumed to be viscoelastic, a viscoelastic model is introduced for S_{FD} and S_D in Section 3.4. In some sense, this approach is the generalization to transversely isotropic behavior of the hydrostatic/deviatoric decomposition for viscoelasticity, introduced for instance in J.C. Simo (1987). In principle, the viscoelastic behavior of the matrix could have different effects on the longitudinal and transverse shear behaviors of the composite, thus two different viscoelastic relaxation functions could be considered, to be identified via computational homogenization or via direct experimental testing on the composite. This will be the subject of further work.

If the full compliance tensor $\boldsymbol{S}$, defined as $\boldsymbol{\varepsilon} = \boldsymbol{S} : \boldsymbol{\sigma}$, is needed (such as for the implementation of a user material in a standard finite element code), it can be written as

$$\begin{aligned}\boldsymbol{S} =& S_F \boldsymbol{M}_f \otimes \boldsymbol{M}_f + S_H \boldsymbol{M}_h \otimes \boldsymbol{M}_h + S_{FH} \left(\boldsymbol{M}_f \otimes \boldsymbol{M}_h + \boldsymbol{M}_h \otimes \boldsymbol{M}_f\right) \\ &+ S_{FS} \left(\boldsymbol{M}_{f2} \otimes \boldsymbol{M}_{f2} + \boldsymbol{M}_{f3} \otimes \boldsymbol{M}_{f3}\right) + S_D \left(\boldsymbol{M}_d \otimes \boldsymbol{M}_d + \boldsymbol{M}_{23} \otimes \boldsymbol{M}_{23}\right).\end{aligned} \tag{3.14}$$

In practice, the inverse (stiffness) relations will be used in the implementation, but the compliance relations were derived here because of their easier physical interpretation.

3.2.1 . Remarks

- Considering again the particular case in which $\{\boldsymbol{v}_f = \boldsymbol{e}_1, \boldsymbol{v}_2 = \boldsymbol{e}_2, \boldsymbol{v}_3 = \boldsymbol{e}_3\}$, the values of the new elastic parameters S_F, S_{FH}, S_H, S_{FS} and S_D can be identified in terms of the classical elastic constants (E_L, E_T, μ_L, μ_T, ν_{LT}). In particular, the relations can be obtained comparing the compliance tensor written in the two

notations:

$$\boldsymbol{S} = \begin{pmatrix} S_F & \frac{S_{FH}}{\sqrt{2}} & \frac{S_{FH}}{\sqrt{2}} & 0 & 0 & 0 \\ \frac{S_{FH}}{\sqrt{2}} & \frac{S_H+S_D}{2} & \frac{S_H-S_D}{2} & 0 & 0 & 0 \\ \frac{S_{FH}}{\sqrt{2}} & \frac{S_H-S_D}{2} & \frac{S_H+S_D}{2} & 0 & 0 & 0 \\ 0 & 0 & 0 & S_D & 0 & 0 \\ 0 & 0 & 0 & 0 & S_{FS} & 0 \\ 0 & 0 & 0 & 0 & 0 & S_{FS} \end{pmatrix}, \tag{3.15}$$

$$\boldsymbol{S} = \begin{pmatrix} \frac{1}{\mathsf{E}_L} & -\frac{\nu_{LT}}{\mathsf{E}_L} & -\frac{\nu_{LT}}{\mathsf{E}_L} & 0 & 0 & 0 \\ -\frac{\nu_{LT}}{\mathsf{E}_L} & \frac{1}{\mathsf{E}_T} & -\frac{\nu_{TT}}{\mathsf{E}_T} & 0 & 0 & 0 \\ -\frac{\nu_{LT}}{\mathsf{E}_L} & -\frac{\nu_{TT}}{\mathsf{E}_T} & \frac{1}{\mathsf{E}_T} & 0 & 0 & 0 \\ 0 & 0 & 0 & \frac{1}{2\mu_T} & 0 & 0 \\ 0 & 0 & 0 & 0 & \frac{1}{2\mu_L} & 0 \\ 0 & 0 & 0 & 0 & 0 & \frac{1}{2\mu_L} \end{pmatrix}. \tag{3.16}$$

The longitudinal and transverse shear responses are immediately recognizable in both sets:

$$\begin{aligned} S_{FS} &= \frac{1}{2\mu_L}, \\ S_D &= \frac{1}{2\mu_T}. \end{aligned} \tag{3.17}$$

Furthermore we have, from terms (1,1), (1,2) and (2,2):

$$\begin{aligned} S_F &= \frac{1}{E_L}, \\ S_{FH} &= -\frac{\sqrt{2}\nu_{LT}}{E_L}, \\ S_H &= \frac{2}{E_T} - \frac{1}{2\mu_T}. \end{aligned} \tag{3.18}$$

It should be noticed that, since S_H is assumed as purely elastic in the following, the viscous relaxation of the transverse modulus E_T is directly related to the viscous relaxation of the transverse shear modulus μ_T, and not an independent function of time.

Finally, the fourth equation, term (2,3), yields the well-known transverse isotropy condition:

$$\mu_T = \frac{E_T}{2\left(1+\nu_{TT}\right)}. \tag{3.19}$$

- The decomposition proposed in Eq. (3.1) is similar to the one introduced in Spencer (1984) and used by Nedjar (2011) to model the viscoelastic response of unidirectional plies. The decomposition proposed in those works, however, is derived *a posteriori* from internal constraints, and not defined *a priori* in a rigorous mathematical fashion as it is the case here. As a result, the elastic parameters obtained by Spencer (1984); Nedjar (2011), although different from the classical set (E_L, E_T, μ_L, μ_T, ν_{LT}), are not fully uncoupled and they do not have a clear physical interpretation. As a consequence, the introduction of a viscoelastic behavior for a certain portion of the composite's response is less clear, since different combinations of the five elastic parameters intervene both in the elastic and viscoelastic responses, making it difficult to formulate a full tangent stiffness or compliance tensor, as well as to account for possibly different viscoelastic effects on the longitudinal shear and on the (2,3) plane deviatoric responses. This is the reason why the present approach was proposed here instead.

3.3 . Analytical homogenisation

In the previous Section, the Cartan decomposition was used for the stress and strain tensors in order to derive completely uncoupled material parameters in which the contributions of the composite constituents (fibers and matrix) are highlighted. The elastic parameters affected by the deviatoric response of the matrix are assumed to be viscoelastic, while the remaining parameters are fully elastic.

In the present Section, analytical solutions for the elastic moduli of a transversely isotropic medium, obtained from the homogenization of a unidirectional fiber-reinforced composite, derived by Hill (1964); Hashin and Rosen (1964), are used in order to justify the assumptions made in Section 3.2.

The analytical solutions were derived based on a cylindrical model (Hill (1964); Hashin and Rosen (1964)) and were later extended to viscoelasticity in Hashin (1970b). The extension to viscoelasticity is based on a correspondence principle, stating that the same formulas derived for the elastic moduli can be applied, simply replacing the elastic moduli of each phase with their complex moduli. Although they are based on some simplifying assumptions, these early results enable us to estimate the elastic and viscoelastic response of the transversely isotropic composite. In particular, the role of the matrix shear modulus in determining the different elastic parameters defined in Section 3.2 can be

highlighted.

Let us consider then the expressions of the elastic parameters, as given in Hashin (1970a):

$$\mu_L = \mu_m \left[1 + \frac{v_f}{\frac{\mu_m}{\mu_f - \mu_m} + \frac{v_m}{2}} \right] \tag{3.20}$$

$$\mu_T = \mu_m \frac{\left(1 + \alpha v_f^3\right)\left(\rho + \beta_m v_f\right) - 3 v_f v_m^2 \beta_m^2}{\left(1 + \alpha v_f^3\right)\left(\rho - \beta_f\right) - 3 v_f v_m^2 \beta_m^2} \tag{3.21}$$

$$E_L = E_m v_m + E_f v_f + \frac{4 v_m v_f \left(\nu_f - \nu_m\right)^2}{\frac{v_m}{k_f} + \frac{v_f}{k_m} + \frac{1}{\mu_m}} \tag{3.22}$$

$$\nu_{LT} = \nu_m v_m + \nu_f v_f + \frac{v_m v_f \left(\nu_f - \nu_m\right)\left(\frac{1}{k_m} - \frac{1}{k_f}\right)}{\frac{v_m}{k_f} + \frac{v_f}{k_m} + \frac{1}{\mu_m}} \tag{3.23}$$

$$k_T = k_m \left[1 + \frac{v_f}{\frac{k_m}{k_f - k_m} + \frac{k_m v_m}{k_m + \mu_m}} \right], \tag{3.24}$$

where k_i, μ_i and ν_i are the bulk and shear moduli and the Poisson's coefficient of the phases (fibres and matrix), supposed isotropic, v_i are the volume fractions, and the following relations are defined

$$\alpha = \frac{\beta_m - \gamma \beta_f}{1 + \beta_f}, \ \rho = \frac{\gamma + \beta_m}{\gamma - 1}, \ \beta_i = \frac{1}{3 - 4\nu_i}, \ \gamma = \frac{\mu_f}{\mu_m} \tag{3.25}$$

$$E_i = \frac{9 k_i \mu_i}{3 k_i + \mu_i}, \quad \nu_i = \frac{3 k_i - 2 \mu_i}{2\left(3 k_i + \mu_i\right)}. \tag{3.26}$$

It should be noted that four of the expressions are exact results from the cylindrical model. The results can be extended to transversely isotropic constituents, but it is not detailed further here.

Among the five independent parameters selected in Hashin (1970a) to describe the transversely isotropic behavior, μ_L, μ_T, E_L and ν_{LT}, are classical elastic constants already discussed, while k_T is the transverse bulk modulus. For a plane strain state in the $(2,3)$ plane ($\varepsilon_{11} = 0$), the definition of k_T reads

$$\boldsymbol{\sigma}_{(2,3)} = k_T \mathrm{tr}(\boldsymbol{\varepsilon}_{(2,3)}) \boldsymbol{I} + 2\mu_T \mathrm{dev}(\boldsymbol{\varepsilon}_{(2,3)}). \tag{3.27}$$

This choice is quite interesting, as this set of parameters is closely related to the set considered previously. Indeed, we can show that

$$S_{FS} = \frac{1}{2\mu_L}, \quad S_D = \frac{1}{2\mu_T} \tag{3.28}$$

$$S_F = \frac{1}{E_L}, \quad S_{FH} = -\frac{\sqrt{2}\nu_{LT}}{E_L}, \quad S_H = \frac{2\nu_{LT}^2}{E_L} + \frac{1}{2k_T}. \tag{3.29}$$

The two shear moduli are directly recognizable in both sets of parameters, while the three terms (S_F, S_{FH}, S_H) of the proposed model are related only to the longitudinal Young's modulus E_L, the Poisson's coefficient ν_{LT} and the transverse bulk modulus k_T. In Section 3.2, the three parameters (S_F, S_{FH}, S_H) were assumed to be mainly influenced by the properties of the fibers and by the bulk modulus of the matrix, which are elastic. Analyzing the role of μ_m in Equations (3.20) to (3.24) enables us to verify and test the limits of this assumption.

Considering Equations (3.20) and (3.21), it is easy to realize that the transverse and in-plane shear moduli of the composite, μ_L, and μ_T, show a direct dependence on the matrix shear modulus μ_m, and in particular they tend to zero as the matrix shear modulus tends to zero. The three remaining parameters, Equations (3.22) to (3.24), on the other end, are indeed affected by μ_m, but their dependence is less significant, and they will retain a non-zero value even for $\mu_m \to 0$. Given Equations (3.28) and (3.29), the elastic parameters of the proposed model can also be divided into two sets, according to their behavior as $\mu_m \to 0$:

- (S_{FS}, S_D) tend to infinity (no remaining stiffness);
- (S_F, S_{FH}, S_H) retain a finite value (finite remaining stiffness).

This fundamental difference between the two sets confirms the pertinence of choosing this set of parameters in order to make a clear link with the underlying constituents' response. For this reason, this constitutes the first justification for the assumption proposed in Section 3.2.

Since μ_m actually appears in Equations (3.22) to (3.24), considering that these parameters are not affected by the matrix shear modulus is indeed an approximation, whose pertinence depends on the values of the moduli and volume fractions of the two phases. The closed-form solutions provided by Hashin (1970a) enable us to evaluate the error introduced by this approximation.

In typical polymer matrix composites, which are considered in this study, the two constituents have similar volume fractions, the fibers are one (for the glass fibers) or two orders (for the carbon fibers) of magnitude stiffer than the matrix, and the polymer matrix behavior is generally moderately compressible, with a Poisson's coefficient close to 0.5. Figure 3.1 depicts the normalised composite parameters obtained from Equations (3.20)-(3.24) and (3.28)-(3.29) as a function of decreasing normalised matrix shear modulus, for typical constituents' properties. The direct influence of μ_m on the first two parameters is immediately noticeable, while the three remaining parameters display little variations. In particular, the response in the fibers' direction, S_F, is nearly constant,

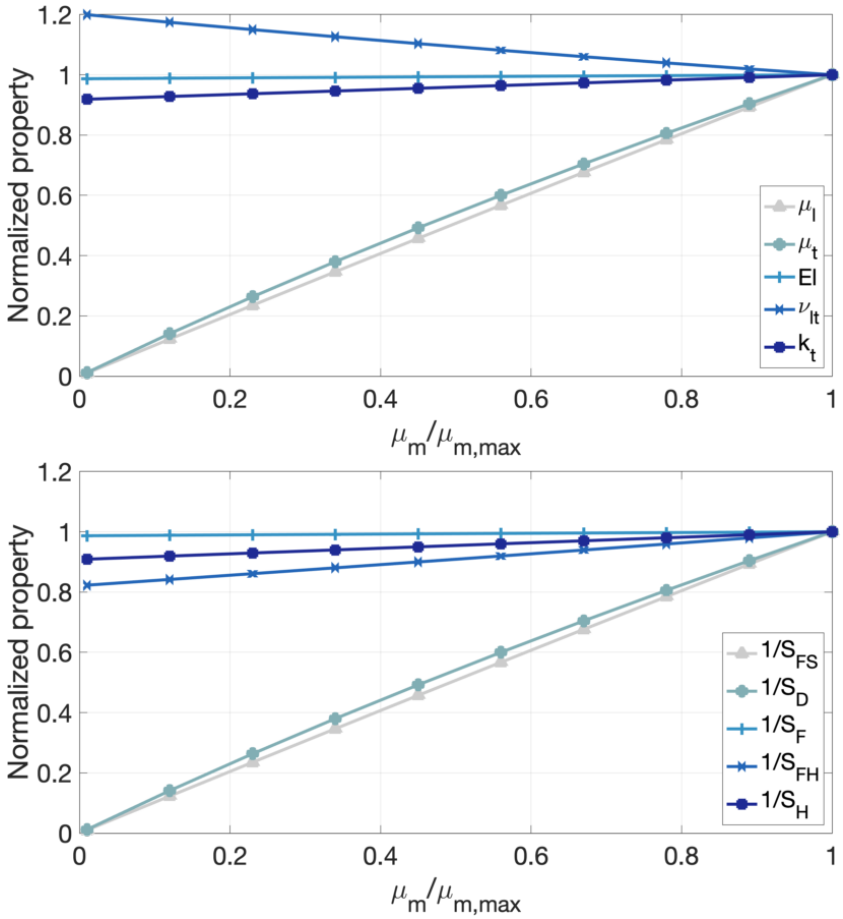

Figure 3.1: Normalised composite parameters for decreasing normalised matrix shear modulus (initial set of parameters for the constituents from Mallick (2008): $E_f = 248$ GPa, $\nu_f = 0.2$, $E_m = 3.24$ GPa, $\nu_m = 0.4$, $v_f = 0.5$).

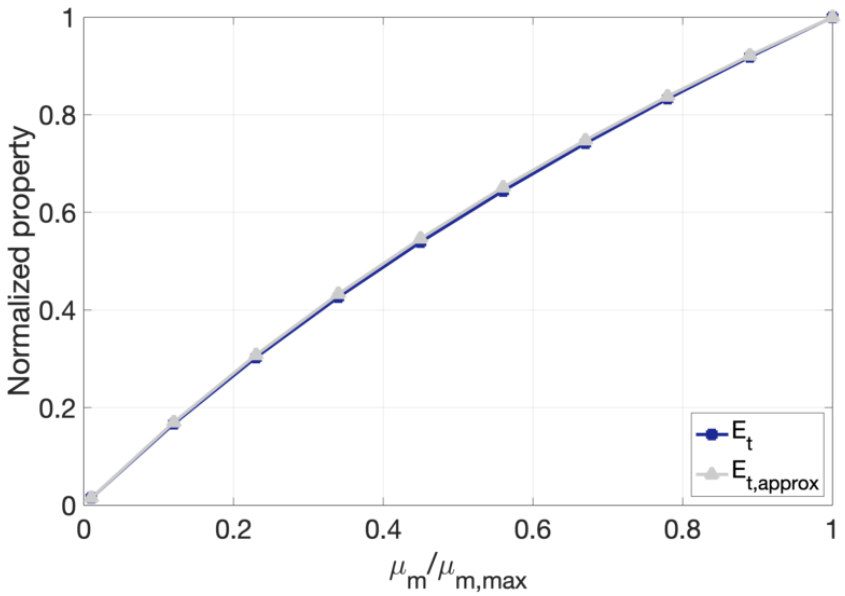

Figure 3.2: Composite transverse modulus E_t computed using Eqs. (3.20) to (3.24) *vs* Eq. (3.30), for decreasing normalised matrix shear modulus (initial set of parameters for the constituents from Mallick (2008): $E_f = 248$ GPa, $\nu_f = 0.2$, $E_m = 3.24$ GPa, $\nu_m = 0.4$, $v_f = 0.5$).

while the hydrostatic response in the plane of transverse isotropy, S_H, varies by 10% maximum and the coupling term, S_{FH}, by 20%.

It is interesting to notice that neglecting the variations of (S_F, S_{FH}, S_H) with respect to the matrix shear modulus still enables us to represent the transverse modulus E_T of the composite with considerable accuracy. This can be observed in Figure 3.2, where the transverse modulus computed using Eqs. (3.20) to (3.24) is compared to the one obtained by the following expression:

$$E_{T,approx} = \frac{2}{S_{H,ini} + S_D}, \tag{3.30}$$

where $S_{H,ini}$ is maintained at its initial value, and only S_D is considered to be affected by the evolution of the matrix shear modulus μ_m. As it can be seen from the Figure (3.2), the two results are nearly superposed. This confirms the assumption, made in Di Gennaro et al. (2021), that the strong influence of the matrix shear modulus μ_m on the transverse modulus of the composite, E_T, is essentially related to the in-plane deviatoric response.

3.4 . Linear viscoelasticity

A linear viscoelastic model is defined here and applied to the terms μ_L and μ_T of the behavior introduced in the previous Section.

Several viscoelastic models that can be found in the literature can be effectively understood by looking at their rheological representations. Combinations of springs and dash-pots can accurately represent and describe the material viscoelastic behavior.

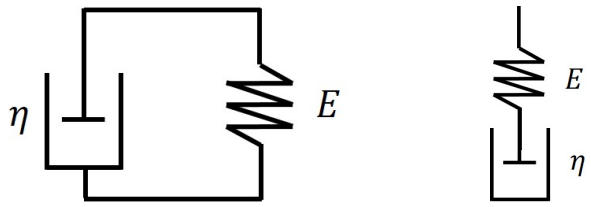

Figure 3.3: Basic rhelogical units: Kelvin-Voigt (left) and Maxwell (right)

The Kelvin-Voigt basic rheological unit, as shown in Figure (3.3) left, is characterized by a spring and a dash-pot in parallel, and its one dimensional differential equation is:

$$s = Ee + \eta\dot{e}, \tag{3.31}$$

where s and e are the one-dimensional stress and strain, E is the spring stiffness and η is the viscosity of the dash-pot. The generalized Kelvin-Voigt model, obtained by setting N different Kelvin-Voigt units (plus, eventually, a single spring) in series, is typically used to describe the material creep at constant stress.

The Maxwell basic rheological unit, on the other hand, is characterized by a spring and a dash-pot in series, and its one dimensional differential equation is:

$$\frac{s}{\eta} + \frac{\dot{s}}{E} = \dot{e},$$

which can be rewritten as

$$\frac{s}{\tau} + \dot{s} = E\dot{e}, \tag{3.32}$$

where the characteristic relaxation time for a given Maxwell unit is $\tau = \frac{\eta}{E}$.

In a stress relaxation test, imposing a constant strain e' at the time $t = t'$, the Maxwell model in Equation (3.32) leads to (Kelly, 2013; Simo and Hughes, 1998; Ward and Sweeney, 2004)

$$s = e'E\left(t - t'\right), \quad \text{where} \quad E(t - t') = E\exp\left(-\frac{t - t'}{\tau}\right) \tag{3.33}$$

is called the relaxation modulus function of the Maxwell model.

A convenient way to derive the viscoelastic formulation for the Maxwell model is through the integral representation. From Equation (3.32), using the integration factor $\exp(t/\tau)$ we obtain, (Kelly, 2013; Simo and Hughes, 1998):

$$\frac{d}{dt}\left(\exp\left(\frac{t}{\tau}\right)s(t)\right) = E\exp\left(\frac{t}{\tau}\right)\frac{de(t)}{dt}. \tag{3.34}$$

Integrating over the interval $[0,\hat{t}]$ and assuming that $s(0) = 0$ we have

$$s(\hat{t}) = \int_0^t E\exp\left(\frac{t-\hat{t}}{\tau}\right)\frac{de(t)}{dt}dt. \tag{3.35}$$

Remembering the expression of the relaxation modulus function in Equation (3.33) and changing the notation follows

$$s(t) = \int_0^t E\left(t-t'\right)\frac{de(t')}{dt'}dt'. \tag{3.36}$$

The generalized Maxwell model (Figure 3.4), obtained by setting N different Maxwell units and a single spring in parallel, is typically used to characterize the stress relaxation at constant strain of the material (as we saw earlier).

The relaxation modulus function for the generalized Maxwell model can be written as follows:

$$E\left(t-t'\right) = E^{\infty} + \sum_{i=1}^{N} E_i \exp\left(-\frac{t-t'}{\tau}\right). \tag{3.37}$$

In the present case, a general loading path is sought, in which stress and strain both vary to satisfy the problem equations. In this case, both generalized Kelvin-Voigt and generalized Maxwell models have been successfully applied in the literature (see, for example, Nedjar (2011) for the generalized Kelvin-Voigt model, and Kaliske (2000) for the generalized Maxwell model), often without an explicit discussion on the modeling choice.

In the following, a generalized Maxwell model is considered for ease of implementation in a finite element setting. Indeed, in a classical finite element implementation, the search direction to determine stress and strain fields which satisfy the local constitutive behavior is taken at constant displacement. For this reason, the algorithms which solve the local constitutive equations are strain-driven, and each element of the generalized Maxwell model can be solved independently. Furthermore, based on the Boltzmann superposition principle, the model

is formulated in integral form, which enables us to make use of well known literature results to achieve a simple and accurate numerical integration scheme.

From Equation (3.36) the hereditary integrals for $\boldsymbol{s}_{fs}$ and $\boldsymbol{s}_d$ of the generalized Maxwell model are:

$$\begin{aligned} \boldsymbol{s}_{fs}(t) &= \int_0^t \Gamma_{fs}(t-t')\frac{d\boldsymbol{e}_{fs}(t')}{dt'}dt', \\ \boldsymbol{s}_d(t) &= \int_0^t \Gamma_d(t-t')\frac{d\boldsymbol{e}_d(t')}{dt'}dt', \end{aligned} \tag{3.38}$$

where the relaxation functions Γ_{fs} and Γ_d, remembering Equation (3.37), can be written as follows:

$$\begin{aligned} \Gamma_{fs}(t-t') &= 2\mu_L^{lt} + \sum_{j=1}^{N} 2\mu_{L_j} \exp\left(-\frac{t-t'}{\tau_{fs_j}}\right), \\ \Gamma_d(t-t') &= 2\mu_T^{lt} + \sum_{j=1}^{N} 2\mu_{T_j} \exp\left(-\frac{t-t'}{\tau_{d_j}}\right). \end{aligned} \tag{3.39}$$

In these expressions, the parameter μ_L^{lt} (resp. μ_T^{lt}) is associated to the isolated spring, and it represents the long term behavior once all stress relaxation has taken place. The parameter μ_{L_j} (resp. μ_{T_j}) is associated to the j-th spring, while τ_{fs_j} (resp. τ_{d_j}) is the relaxation time associated to the j-th Maxwell element.

From now on, only the mathematical development of the viscoelastic model for the terms $\boldsymbol{s}_{fs}$ and $\boldsymbol{e}_{fs}$ is detailed, as the two equations are identical in all except the material parameters. Substituting (3.39) into (3.38), it is possible to split the integral into a long term elastic part and

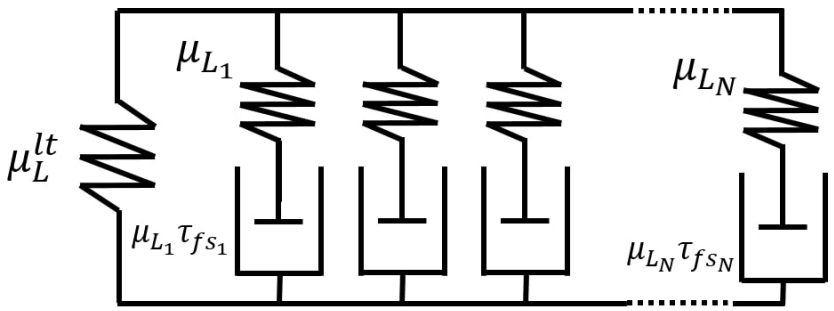

Figure 3.4: Material parameters for the Generalized Maxwell rheological model

a viscoelastic one:

$$\boldsymbol{s}_{fs}(t) = 2\mu_L^{lt}\boldsymbol{e}_{fs} + \sum_{j=1}^{N}\int_0^t 2\mu_{L_j}\exp\left(-\frac{t-t'}{\tau_{fs_j}}\right)\frac{d\boldsymbol{e}_{fs}(t')}{dt'}dt'. \tag{3.40}$$

Finally, from (3.40) $\boldsymbol{s}_{fs}$ can be decomposed as:

$$\boldsymbol{s}_{fs} = \boldsymbol{s}_{fs_0} + \sum_{j=1}^{N}\boldsymbol{g}_{fs_j}. \tag{3.41}$$

Eq. (3.41) shows how $\boldsymbol{s}_{fs}$ is obtained as a summation of an elastic stress $\left(\boldsymbol{s}_{fs_0} = 2\mu_L^{lt}\boldsymbol{e}_{fs}\right)$, and j internal viscoelastic stress variables $\boldsymbol{g}_{fs_j}$.

Finding an accurate and efficient numerical solution of the integral in Eq. (3.40) is crucial. Considering the time step $\Delta t = t^{n+1} - t^n$, and noting with a superscript i the quantities at time t^i, the elastic stress is readily computed as $\boldsymbol{s}_{fs_0}^{n+1} = 2\mu_L^{lt}\boldsymbol{e}_{fs}^{n+1}$, while the internal variables can be written as:

$$\boldsymbol{g}_{fs_j}^{n+1} = 2\mu_{L_j}\int_0^{t^{n+1}}\exp\left(-\frac{t^{n+1}-t'}{\tau_{fs_j}}\right)\frac{d\boldsymbol{e}_{fs}(t')}{dt'}dt'. \tag{3.42}$$

Remembering the properties of the integral and of the exponential function, we obtain:

$$\boldsymbol{g}_{fs_j}^{n+1} = \exp\left(-\frac{\Delta t}{\tau_{fs_j}}\right)\boldsymbol{g}_{fs_j}^{n} + 2\mu_{L_j}\int_{t^n}^{t^{n+1}}\exp\left(-\frac{t^{n+1}-t'}{\tau_{fs_j}}\right)\frac{d\boldsymbol{e}_{fs}(t')}{dt'}dt'. \tag{3.43}$$

This recursive formulation, first introduced in Taylor et al. (1970), is particularly efficient for large finite element problems, as it enables us to compute the internal variables at the current time instant t^{n+1}, knowing the information at the previous time instant t^n only, without needing to store the whole history of the material.

The finite difference approximation of the first derivative of the strain tensor $\boldsymbol{e}_{fs}$ enables us to compute the increment of the internal variables:

$$\frac{d\boldsymbol{e}_{fs}(t')}{dt'} \approx \frac{\boldsymbol{e}_{fs}^{n+1} - \boldsymbol{e}_{fs}^{n}}{\Delta t}. \tag{3.44}$$

Applying (3.44) to (3.43) we have:

$$\boldsymbol{g}_{fs_j}^{n+1} = \exp\left(-\frac{\Delta t}{\tau_{fs_j}}\right)\boldsymbol{g}_{fs_j}^{n} + 2\mu_{L_j}\int_{t^n}^{t^{n+1}}\exp\left(-\frac{t^{n+1}-t'}{\tau_{fs_j}}\right)dt'\left(\frac{\boldsymbol{e}_{fs}^{n+1} - \boldsymbol{e}_{fs}^{n}}{\Delta t}\right). \tag{3.45}$$

Solving the integral analytically, we finally obtain the following closed-form expression:

$$\boldsymbol{g}_{fs_j}^{n+1} = \exp\left(-\frac{\Delta t}{\tau_{fs_j}}\right)\boldsymbol{g}_{fs_j}^{n} + \frac{1-\exp\left(-\frac{\Delta t}{\tau_{fs_j}}\right)}{\left(\frac{\Delta t}{\tau_{fs_j}}\right)} 2\mu_{L_j}\left[\boldsymbol{e}_{fs}^{n+1} - \boldsymbol{e}_{fs}^{n}\right]. \quad (3.46)$$

With analogous reasoning, the consistent tangent stiffness can be obtained as:

$$2\mu_L^{n+1} = 2\mu_L^{lt} + \sum_{j=1}^{N} 2\mu_{L_j}\frac{1-\exp\left(-\frac{\Delta t}{\tau_{fs_j}}\right)}{\left(\frac{\Delta t}{\tau_{fs_j}}\right)}. \quad (3.47)$$

The full tangent constitutive tensor, useful to achieve efficient numerical solutions in commercial finite element codes, can be simply obtained by replacing the tangent values of μ_L and μ_T in Eq. (3.14).

Small values of $\left(\frac{\Delta t}{\tau_{fs_j}}\right)$ lead to cancellation error of the second term on the right-hand side of Eq. (3.46) and (3.47). In order to avoid this inconvenience, under these conditions the aforementioned term can be replaced by its Taylor series development as follows (Sorvari and Hämäläinen, 2010):

$$\frac{1-\exp\left(-\frac{\Delta t}{\tau_{fs_j}}\right)}{\left(\frac{\Delta t}{\tau_{fs_j}}\right)} \approx 1 - \frac{1}{2}\left(\frac{\Delta t}{\tau_{fs_j}}\right) + \frac{1}{6}\left(\frac{\Delta t}{\tau_{fs_j}}\right)^2. \quad (3.48)$$

It is important to notice that the only approximation introduced in the numerical solution is in Eq. (3.44), while the integral has been solved analytically. The resulting numerical integration algorithm is particularly accurate, even for large time increments.

3.4.1 . Remarks

The parameters to be identified for the viscoelastic portion of the model are μ_L^{lt} (resp. μ_T^{lt}), as well as μ_{L_j} and τ_{fs_j} (resp. μ_{T_j} and τ_{d_j}) for each Maxwell element. In particular, μ_L^{lt}, related to $\boldsymbol{s}_{fs_0}$, is the long term modulus, once viscoelastic relaxation has completely occurred (that is, once the internal variables $\boldsymbol{g}_{fs_j}$ are null), while the short term (instantaneous) modulus is given by $\mu_L^{st} = \mu_L^{lt} + \sum_{j=1}^{N}\mu_{L_j}$. Experimental characterization at temperatures much lower than the reference temperature yield a measure of μ_L^{st}, while higher temperature tests over time scales similar to the relaxation time enable to evaluate the other viscoelastic properties.

3.5 . Effects of temperature: thermal strains and time-temperature superposition

The viscoelastic response of the matrix and, consequently, of the composite, plays a crucial role in the establishment of residual stresses and strains during manufacturing processes involving high temperature gradients. In order to model these phenomena, temperature effects are included in the present model: in particular, the thermal strain is introduced, as well as the effect of temperature on viscoelasticity through time-temperature superposition.

In Section 3.2 the stress and strain Cartan decomposition was presented. The thermal strain can be decomposed in the same way to yield

$$\boldsymbol{\varepsilon}^{th} = e_f^{th}\boldsymbol{M}_f + e_h^{th}\boldsymbol{M}_h, \tag{3.49}$$

where

$$e_f^{th} = \alpha_1 \Delta T, \quad e_h^{th} = \sqrt{2}\alpha_2 \Delta T, \tag{3.50}$$

and α_1 and α_2 are the coefficient thermal expansions in the fibers' direction and in the transverse isotropy plane, respectively. Therefore, the viscoelastic strain tensor can be written as:

$$\boldsymbol{\varepsilon}^{ve} = \left(e_f - e_f^{th}\right)\boldsymbol{M}_f + \left(e_h - e_h^{th}\right)\boldsymbol{M}_h + \boldsymbol{e}_{fs} + \boldsymbol{e}_d. \tag{3.51}$$

It is interesting to notice that the thermal strain does not contain the terms $\boldsymbol{e}_{fs}$ and $\boldsymbol{e}_d$, while the viscoelastic model presented in Section 3.4 only applies to these two terms. Consequently, any possible relaxation of the stresses induced by incompatible thermal strains cannot occur directly through the f and h portions of the behavior, which is purely elastic, but needs to be linked to the viscoelastic portions fs and d. Obviously, the link between the different portions of the behavior occurs through the directions of the stress and strain tensors imposed by the rest of the problem equations. This consideration, which is valid as well for classical isotropic temperature-dependent viscoelastic behavior, is resumed in the rheological scheme of Fig. 3.5.

The definition of the stress relaxation as a function of the temperature involves, for thermorheologically simple materials, the introduction of a new time scale called reduced time, which is a function of the temperature (Lakes, 2009). The reduced time is defined as follows:

$$t_{red} = \int_0^t \frac{1}{a(T)} dt'. \tag{3.52}$$

The shift function $a(T)$ used here is the Williams-Landel-Ferry equation (WLF law):

$$\log\left[a(T)\right] = -\frac{C_1\left(T - T_{ref}\right)}{C_2 + \left(T - T_{ref}\right)}, \tag{3.53}$$

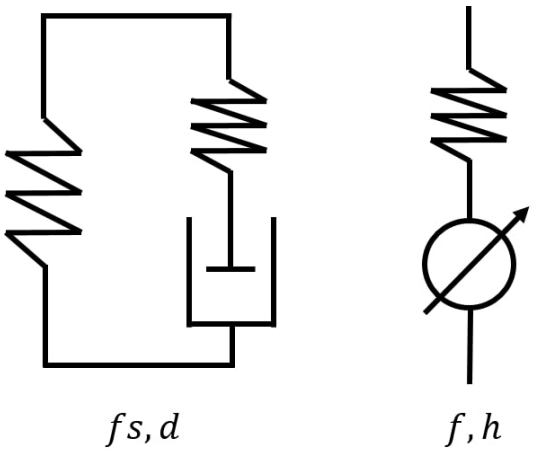

Figure 3.5: Rheological representation of the different portions of the composite's constitutive behavior: generalized Maxwell model to describe the viscoelastic portions (left) and the elastic portions with thermal strains (right)

where T is the temperature, T_{ref} is the reference temperature for the polymer (generally coincident with the glass transition temperature) and C_1, C_2 are two material constants. The reduced time is used instead of the real time in the viscoelastic model equations of Section 3.4.

Depending on the composite's temperature, two extreme scenarios can occur (Fig. 3.6):

- for temperatures well above the reference temperature, the reduced time is much longer than the real time (and than the relaxation time), so stresses relaxation occurs nearly instantaneously,
- for temperatures much lower than the reference temperature, the reduced time is much shorter than the relaxation time, so the polymer is characterized by an elastic behavior in the time scale of interest.

Numerical integration of the reduced time is not trivial to compute over a non isothermal time step. Indeed, the shift function $a(T)$ is extremely nonlinear with the temperature. An approximation of the shift function could lead to large errors, therefore $h(T) = -\ln(a(T))$ is approximated instead, as a linear function of the temperature over the time increment (Aba, 2011). Further assuming the temperature T is a linear function of the time t over the time increment, follows:

$$h(T) = -\ln(a(T(t))) = A + Bt, \tag{3.54}$$

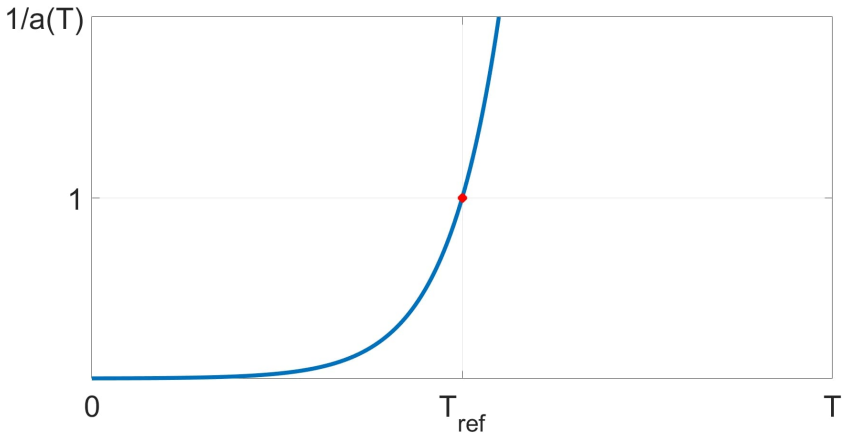

Figure 3.6: Reduced time as a function of temperature

where the coefficients are readily obtained as

$$A = \frac{t^{n+1}h(T^n) - t^n h(T^{n+1})}{\Delta t},$$
$$B = \frac{h(T^{n+1}) - h(T^n)}{\Delta t}. \tag{3.55}$$

Therefore, from Eq. (3.52) the reduced time increment can be computed as follows:

$$\Delta t_{red} = \int_{t^n}^{t^{n+1}} \exp\left(A + Bt\right) dt, \tag{3.56}$$

which yields:

$$\Delta t_{red} = \frac{a^{-1}(T^{n+1}) - a^{-1}(T^n)}{h(T^{n+1}) - h(T^n)}. \tag{3.57}$$

3.6 . Numerical simulations

In order to illustrate the main features of the proposed model, several numerical simulations are presented.

In Section 3.6.1, different loading histories are applied to a single material point in order to illustrate the model response in stress relaxation, creep and variable temperature tests. A Matlab implementation of the model is used for these examples.

In Section 3.6.2, on the other hand, the model is used within thermo-mechanical structural simulations, in order to predict the residual stresses distributions within a composite structure for different manufacturing processes. An Abaqus UMAT was implemented to this end, using

C language code generated from the original Matlab implementation via the Matlab Coder toolbox. The UMAT was used in conjunction with standard mechanical elements available in Abaqus.

The instantaneous elastic parameters used for all simulations are the following (Grogan et al., 2015):

$$E_L = 134 \text{ GPa}, \quad E_T = 10.3 \text{ GPa}, \quad \mu_L = 6 \text{ GPa}, \quad \nu_{LT} = 0.32, \quad \nu_{TT} = 0.4.$$

Only one Maxwell element has been used for simplicity. The viscoelastic parameters are specified for each simulation.

3.6.1 . Loading histories on a single material point

Stress relaxation tests

In order to simulate stress relaxation tests, a strain was imposed rapidly, then maintained until complete relaxation of the viscous term. Imposing different combinations of strain components, while setting the other stress components to zero, enables us to highlight some of the model features. Here, the fiber orientation vector was taken as $\boldsymbol{v}_f^{\mathrm{T}} = [1, 0, 0]$, thus the transverse isotropy direction is aligned with the x direction. For the simulations shown in this part, the viscoelastic parameters are taken as:

$$\mu_L^{lt} = 0.1\mu_L^{st}, \quad \mu_T^{lt} = 0.1\mu_T^{st}, \quad \tau_{fs} = 10 \text{ s}, \quad \tau_d = 10 \text{ s}.$$

The result obtained by imposing a shear strain $\varepsilon_{xy} = 0.005$ is depicted in Fig.(3.7). The evolution of the stress directly mirrors the evolution of the shear modulus μ_L as defined in Eq. (3.39).

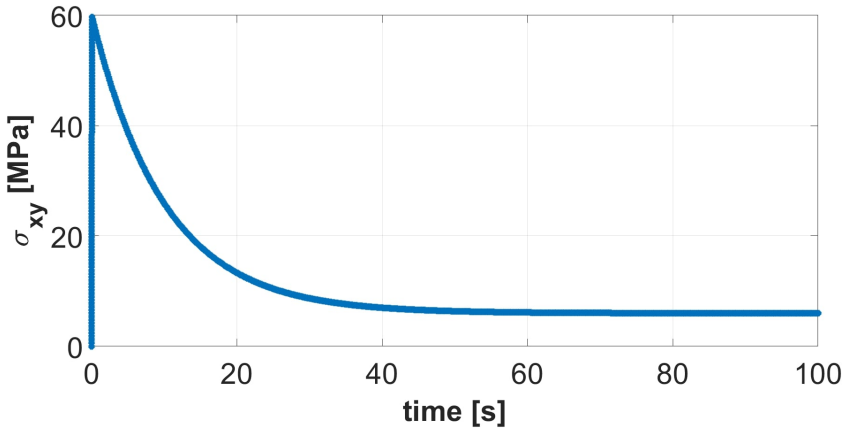

Figure 3.7: Shear stress relaxation for a constant imposed shear strain ($\varepsilon_{xy} = 0.005$)

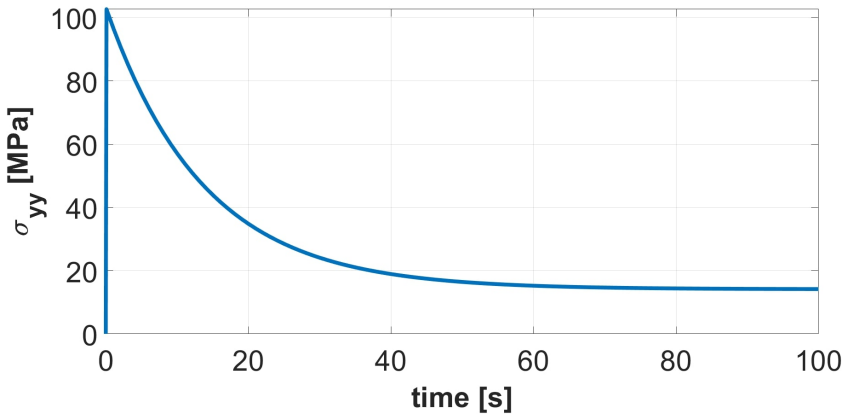

Figure 3.8: Transverse stress relaxation for a constant imposed transverse strain ($\varepsilon_{yy} = 0.01$)

Imposing a strain $\varepsilon_{yy} = 0.01$ in the transverse direction, on the other hand, enables us to observe the evolution of the transverse modulus E_T with time (see Figure 3.8). While other transversely isotropic material models, as Zocher et al. (1997); Kaliske (2000); Pettermann and DeSimone (2018), choose to specify different relaxation function for each of the five material parameters, here the relaxation of E_T is directly related to the relaxation of μ_T, as it can be noticed in the model equations. In particular, the short and long term values of E_T can be easily assessed as:

$$E_T = \frac{4\mu_T}{1 + 2\mu_T S_H}, \tag{3.58}$$

where S_H is constant and μ_T takes its short term and long term values, respectively. This is a distinguishing and very important feature of the proposed model.

More complex combinations of strains enable us to highlight the interplay between the different elements of the stress and strain decomposition. Imposing $\varepsilon_{yy} = 0.01$ and $\varepsilon_{zz} = 0$, the terms e_h and e_d are both constant and equal, and the stress response is the sum of the corresponding s_h and s_d terms. This is illustrated in Fig.(3.9).

The e_h contribution can be easily turned off imposing $\varepsilon_{yy} = 0.01$ and $\varepsilon_{zz} = -0.01$. In this case, the stress relaxation is directly given by the evolution of μ_T (see Fig. (3.10)).

Creep tests

In this example, the viscoelastic response of the composite to a load applied in different directions is illustrated using a creep test. The results are similar to those provided by Nedjar (2011). In particular, the effect of introducing different viscoelastic parameters for μ_L and μ_T is

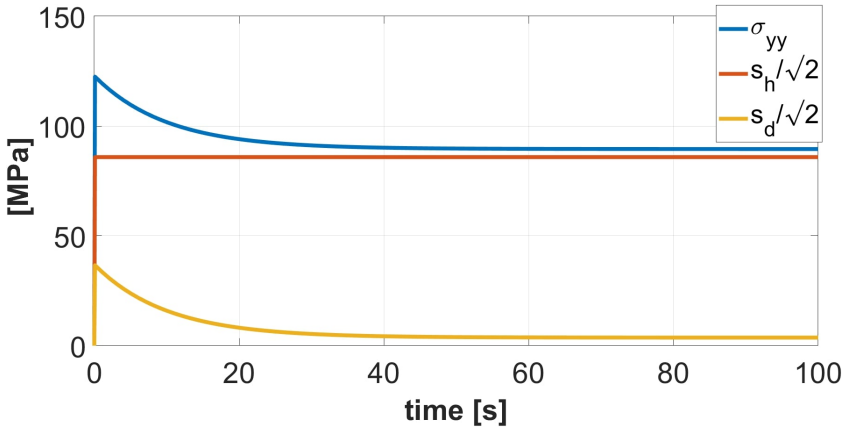

Figure 3.9: Transverse stress relaxation for a biaxial constant imposed strain state ($\varepsilon_{yy} = 0.01$, $\varepsilon_{zz} = 0$)

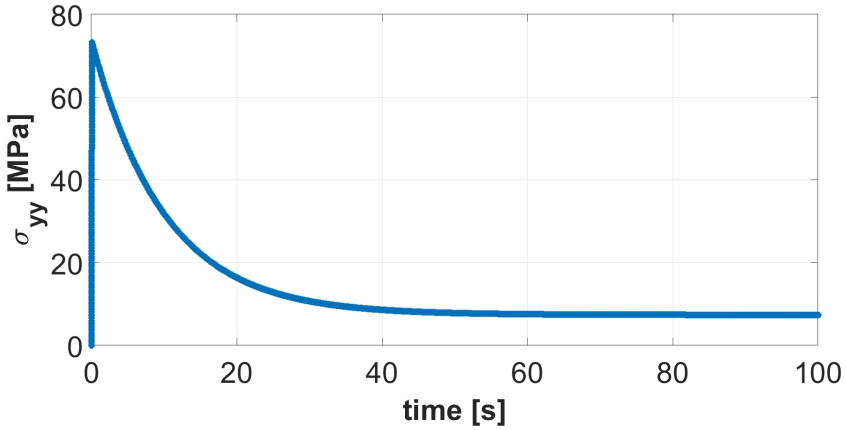

Figure 3.10: Transverse stress relaxation for a biaxial constant imposed strain state ($\varepsilon_{yy} = 0.01$, $\varepsilon_{zz} = -0.01$)

illustrated. Indeed, the viscoelastic behavior of the matrix could translate into different relaxation functions for μ_L and μ_T. Differently from Nedjar (2011), the model proposed here enables one to account for this effect. A more detailed numerical validation of the proposed model, based on the numerical homogenization of a fiber/matrix representative volume element, is among the perspectives of this work.

In order to highlight the effect of each set of viscoelastic parameters, a constant stress $\sigma_{xx} = 100$ MPa was imposed, while the fiber direction $\boldsymbol{v}_f$ was rotated at different angles θ with respect to x.

Two different sets of simulations are depicted in Fig. (3.11). In the first, the viscoelastic parameters are

$$\mu_L^{lt} = 0.5\mu_L^{st}, \quad \mu_T^{lt} = 0.5\mu_T^{st}, \quad \tau_{fs} = 100 \text{ s}, \quad \tau_d = 100 \text{ s},$$

while, in the second, more relaxation is assumed to occur in the μ_T term:

$$\mu_L^{lt} = 0.5\mu_L^{st}, \quad \mu_T^{lt} = 0.28\mu_T^{st}, \quad \tau_{fs} = 100 \text{ s}, \quad \tau_d = 100 \text{ s}.$$

The difference between the two sets of parameters can be noticed, especially in the tests with large angles between the fibers and the loading direction. Indeed, in these transverse dominated directions, the term μ_T plays a more significant role, while μ_L is dominant for small angles. All viscoelastic contribution disappears completely for a load along the fibers's direction, which yields a purely elastic response.

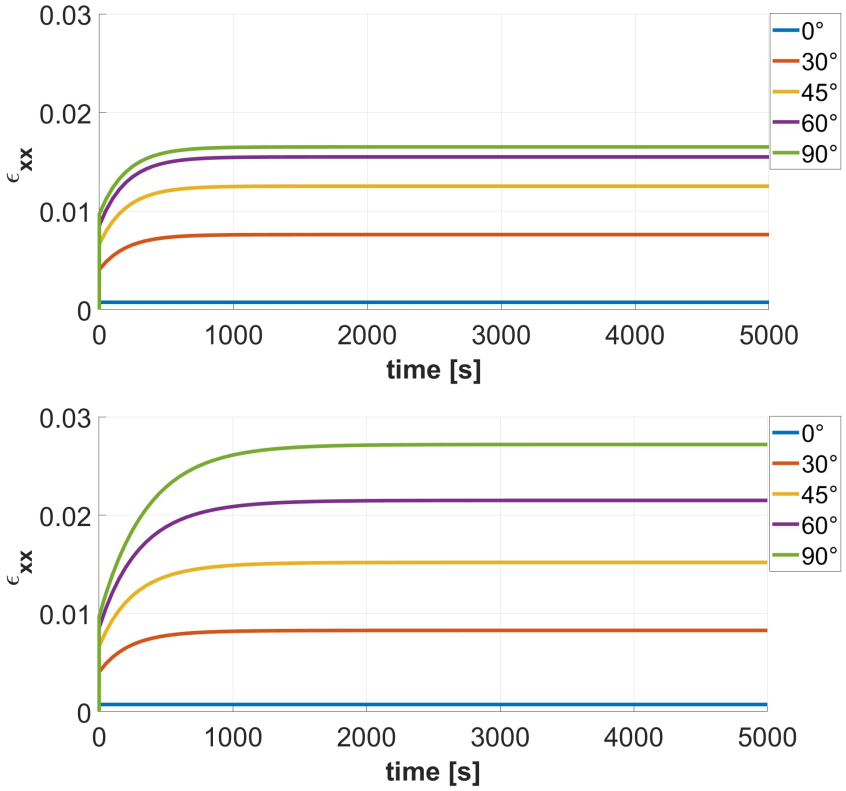

Figure 3.11: Creep loading tests for different angles θ between the loading and the fibers' direction, with the same relaxation functions (top) and with different relaxation functions (bottom) for μ_L and μ_T

Variable temperature tests

In order to see the effect of the temperature on stress relaxation, two simulations of a thermoplastic matrix composite cooling down from above its fusion point were carried out. As for the stress relaxation tests, the fiber orientation vector was taken as $\boldsymbol{v}_f^{\mathrm{T}} = [1, 0, 0]$, thus the

transverse isotropy direction is aligned with the x direction. We suppose that the initial temperature T_0 is associated to a null initial state. A simple linear temperature function (to simulate a constant cooling rate from $T_0 = 400$°C to $T_e = 100$°C in a time frame of 100 s) was used as input, and different restraints were imposed on the material point in order to evaluate their effect on the generation of thermal residual stresses. In this Section, the following viscoelastic parameters were used, to simulate the possibility of nearly complete relaxation:

$$\mu_L^{lt} = 0.001\mu_L, \quad \mu_T^{lt} = 0.001\mu_T, \quad \tau_{fs} = 10 \text{ s}, \quad \tau_d = 10 \text{ s}.$$

The coefficients thermal expansion of the composite material are (Grogan et al., 2015):

$$\alpha_1 = 0.2(10^{-6})/°\text{C}, \quad \alpha_2 = 28.8(10^{-6})/°\text{C},$$

while the parameters used for the WLF law are (Chapman et al., 1990):

$$T_{ref} = 143°\text{C}, \quad C_1 = 52, \quad C_2 = 243°\text{C}.$$

Two different situations were considered. In the first, a null strain was imposed in the transverse isotropic plane ($\varepsilon_{yy} = 0$ and $\varepsilon_{zz} = 0$). From the boundary conditions imposed, stresses in the transverse isotropic plane are equal and non null ($\sigma_{yy} = \sigma_{zz} \neq 0$) therefore, the deviatoric stress is null ($s_d = 0$) while, the hydrostatic stress is non null ($s_h \neq 0$, see Equation (3.4)).

The total hydrostatic strain (e_h) is equal to the sum of the elastic and thermal hydrostatic strains (e_h^{el} and e_h^{th}). Remembering the constitutive law, Equation (3.13), with $s_f = 0$, the total hydrostatic strain is obtained:

$$e_h = e_h^{el} + e_h^{th} = S_H s_h + \sqrt{2}\alpha_2 \Delta T. \tag{3.59}$$

Due to the imposed conditions, the total hydrostatic strain e_h is null, thus the elastic strain is equal and opposite to the thermal strain. Therefore, we obtain the thermal stress as follows:

$$s_h = -\frac{e_h^{th}}{S_H} = -\frac{\sqrt{2}\alpha_2 \Delta T}{S_H} = -\frac{\sqrt{2}\alpha_2 \left(T(t) - T_0\right)}{S_H}. \tag{3.60}$$

Results are shown in Figure (3.12), top. Since the deviatoric part of the response in the plane of transverse isotropy is constrained and it cannot develop, no stress relaxation occurs even for temperatures above the reference temperature T_{ref}.

In the second scenario, a null strain was imposed only in the transverse direction ($\varepsilon_{yy} = 0$). The hydrostatic and deviatoric stresses and

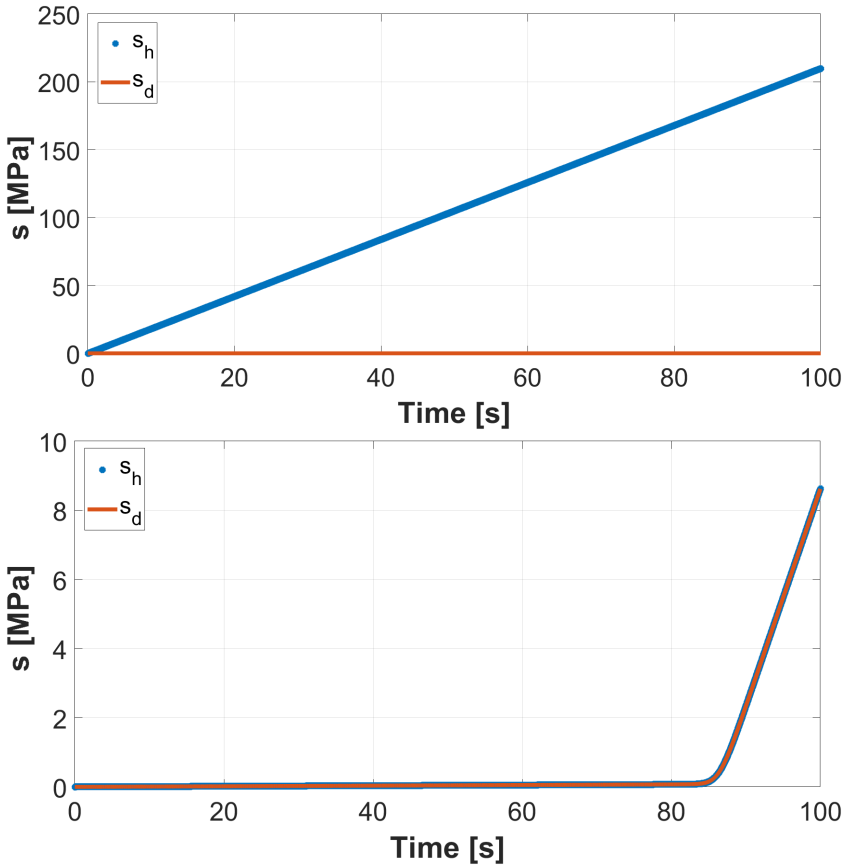

Figure 3.12: Thermal stresses induced by a linear temperature history when the relaxation is inhibited (top) and where the relaxation is allowed (bottom)

strains ($\bullet_h$ and $\bullet_d$ respectively), are both non null. In particular, we can write:

$$s_h = \frac{\sqrt{2}}{2}\left(\sigma_{yy} + \sigma_{zz}\right) = \frac{\sqrt{2}}{2}\sigma_{yy} = s_d, \tag{3.61}$$

$$e_h = \frac{\sqrt{2}}{2}\left(\varepsilon_{yy} + \varepsilon_{zz}\right) = \frac{\sqrt{2}}{2}\varepsilon_{zz} = -e_d, \tag{3.62}$$

$$e_h^{el} = \frac{\sqrt{2}}{2}\left(\varepsilon_{yy}^{el} + \varepsilon_{zz}^{el}\right) \neq e_d^{el} = \frac{\sqrt{2}}{2}\left(\varepsilon_{yy}^{el} - \varepsilon_{zz}^{el}\right). \tag{3.63}$$

For temperature higher than the reference temperature ($T > T^{ref}$), stress relaxation occurs rapidly, and the deviatoric stress is null ($s_d = 0$), as shown in Figure (3.12) bottom. In other words, the transverse isotropic plane (ε_{yy} and ε_{zz}) can adapt to become compatible with the thermal deformation e_h^{th} and have null hydrostatic stress s_h. Thus, elastic deformations do not arise, and the total deformation, from Equation (3.59), can be written as:

$$e_h = e_h^{th} = \sqrt{2}\alpha_2 \Delta T. \tag{3.64}$$

From Equation (3.62), the total strain ε_{zz} during this phase of cooling is:

$$\varepsilon_{zz} = 2\alpha_2 \Delta T = 2\alpha_2 \left(T(t) - T_0\right). \tag{3.65}$$

For temperature lowers than the reference temperature ($T < T^{ref}$), stresses relax extremely slowly and the behavior can be considered elastic. Therefore, s_h and s_d adapt so that the strain is compatible. Hence, we can write (see constitutive relations in Equation (3.13)):

$$e_h = S_H s_h + e_h^{th} \tag{3.66}$$

$$e_d = S_D s_d, \tag{3.67}$$

from which it follows that

$$\frac{\sqrt{2}}{2}\varepsilon_{zz} = S_H \frac{\sqrt{2}}{2}\sigma_{yy} + \sqrt{2}\alpha_2 \Delta T \tag{3.68}$$

$$-\frac{\sqrt{2}}{2}\varepsilon_{zz} = S_D \frac{\sqrt{2}}{2}\sigma_{yy}. \tag{3.69}$$

Solving for σ_{yy} and ε_{zz} the Equations (3.68) and Equation (3.69), and remembering the expression for S_H in Equation (3.18), the trasnverse stress σ_{yy} and the total strain ε_{zz} are obtained:

$$\sigma_{yy} = -\alpha_2 E_T \Delta T = -\frac{\sqrt{2}}{2}\alpha_2 E_T \left(T(t) - T_{ref}\right) \tag{3.70}$$

$$\varepsilon_{zz} = \left(1 + \nu_{TT}\right)\alpha_2 \Delta T = \left(1 + \nu_{TT}\right)\alpha_2 \left(T(t) - T_{ref}\right). \tag{3.71}$$

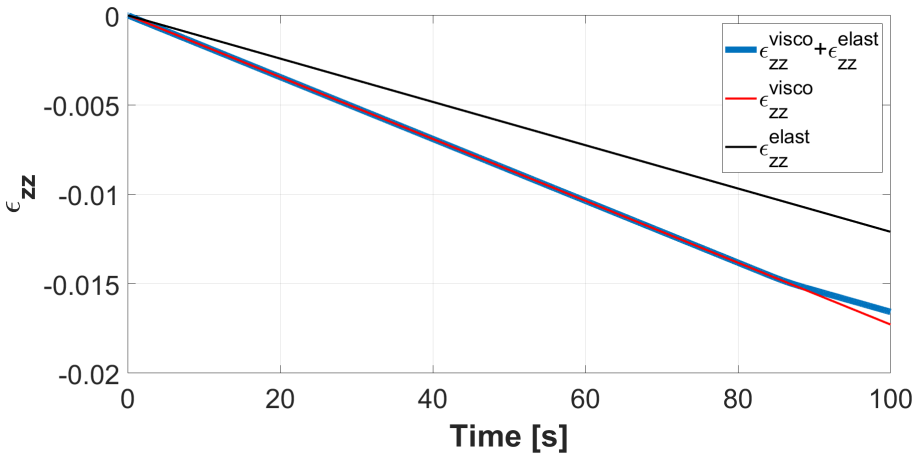

Figure 3.13: Material point simulation imposing $\varepsilon_{yy} = 0$. The total strain in the transverse direction ε_{zz} is depicted. The elastic and viscous strains that would be obtained with constant slopes are also shown.

In other words, in this second scenario, stresses buildup begins at temperatures lower than the reference temperature, since above the viscoelastic behavior of the matrix enables stress relaxation. Through-thickness strains ε_{zz}, on the other hand, develop immediately after cooling from the zero state temperature T_0, according to different slopes in the different zones, Equations (3.65) and (3.71). This will play a significant role in Chapter 5, where this model will be applied to the simulation of residual stresses within tubes.

The hydrostatic and deviatoric stresses are depicted in Figure (3.12) bottom, while the total strain ε_{zz} is depicted in Figure (3.13). Comparing the strain in the viscous domain in Equation (3.65) with the elastic strain in Equation (3.71), it can be noticed that the two linear functions have different slopes. These slopes are highlighted in Figure (3.13). In particular, the elastic ε_{zz}^{elast} and the viscous ε_{zz}^{visco} strains linear functions depicted in Figure (3.13), are obtained imposing the same $T_0 = T_i$ just to highlight the slopes.

In other words, the particular boundary conditions used in the problem induce the coupling between the hydrostatic and deviatoric response of the matrix, allowing thermal hydrostatic stresses relaxation as it was shown in Figure (3.5).

3.6.2 . Structural simulations

In this Section, the temperature-dependent viscoelastic model is used within different thermomechanical structural simulations, in order to compute the residual stressed buildup during manufacturing.

The first set of simulations involves a flat unidirectional plate, cool-

ing under an imposed temperature profile, representing for instance a hot press manufacturing process: in this case, the non-uniform cooling is the only cause of residual stresses buildup, and the cooling rate has a significant influence on the final stress level. The results, analogous to those obtained by Chapman et al. (1990), constitute a first validation of the proposed model.

Residual stress buildup on a cooled infinite plate

In the present Section, following the work presented in Chapman et al. (1990), the residual stresses induced in an infinite, unconstrained unidirectional plate undergoing a non-uniform cooling process were assessed using the commercial finite-element software Abaqus. Numerical simulations were performed on a small plate volume (Fig. (3.14), left). The cooling process occurs through the external surfaces, where an exponential decay temperature function has been imposed. The thermal problem has been solved numerically in Abaqus, setting the following thermal material properties:

$$\rho = 1598 \text{ kg/m}^3, \quad C = 930 \text{ J/(kg K)}, \quad k = 0.4 \text{ W/(m K)},$$

where ρ is the density, C is the specific heat and k is the conductivity in the out-of-plane direction of the composite.

The temperature history obtained from the thermal computation was used as input to the mechanical problem, in which the material behavior of the composite was defined by an UMAT based on the proposed model. The mechanical boundary conditions are schematically represented in Fig. (3.14), right. Specifically, the plate volume can deforms in the thickness direction (z-axis), but the two faces of normals x and y are constrained to remain planar, which represents the effect of the infinite surrounding plate. The parameters for the mechanical simulation are the same as in Section 3.6.1.

Residual stresses in the transverse direction were assessed imposing different cooling rates on the external surfaces of the plate volume as depicted in Fig. (3.15). The outer portions of the plate are the first to reach room temperature, and then act as a constraint to the inner portions, which are not able to contract freely during cooling. A well-known residual stresses profile, with tension at the core and compression close to the surface, develops in the plate. As it can be noted, this effects is exacerbated by high cooling rates, which lead to significant through-thickness temperature gradient. On the other hand, it becomes negligible for slow cooling rates, the limit case being a uniform cooling, which would lead to no internal stresses at the ply's scale for a unidirectional composite.

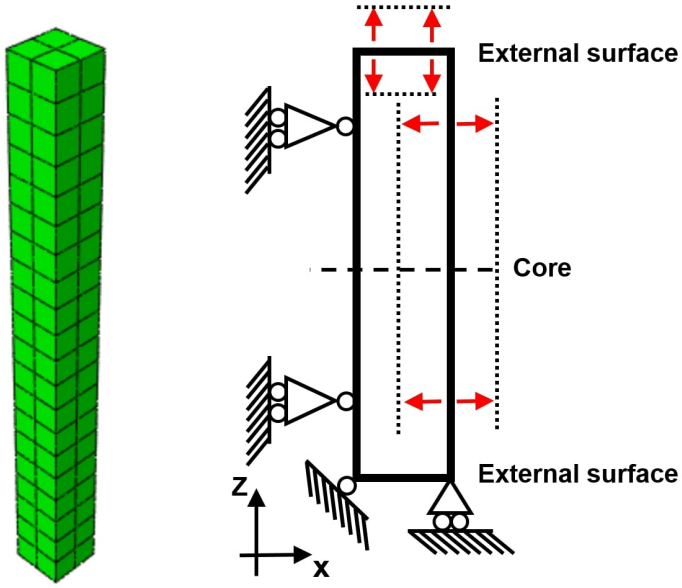

Figure 3.14: Plate volume simulated in Abaqus (left) and schematic representation its mechanical boundary conditions (right)

As we have mentioned before, the numerical simulation performed here is inspired by the work presented in Chapman et al. (1990), which includes both numerical and experimental results. Some differences, however, exist between the simulations in Chapman et al. (1990) and the present work. Indeed, unlike the current version of our model, Chapman et al. (1990) includes the crystallization kinetics of the polymeric matrix, which intervenes as an extra source term in the thermal problem, and as an extra source of inelastic deformation in the mechanical problem. On the other hand, the mechanical model is far simpler, involving an incremental elastic description of the stress/strain relation in order to mimic the viscoleastic behavior. Nevertheless, the comparison between the results of the model proposed here and those given in Chapman et al. (1990) for the same initial cooling rate, reported in Figure 3.15, shows a very good agreement.

3.7 . Conclusions and perspectives

A temperature-dependent viscoelastic constitutive model suited for unidirectional fiber reinforced composite material was presented. In order to highlight the contributions of the fibers and the polymeric matrix, a Cartan decomposition for the stress and the strain tensors was used. The energy function, based on an integrity basis of the de-

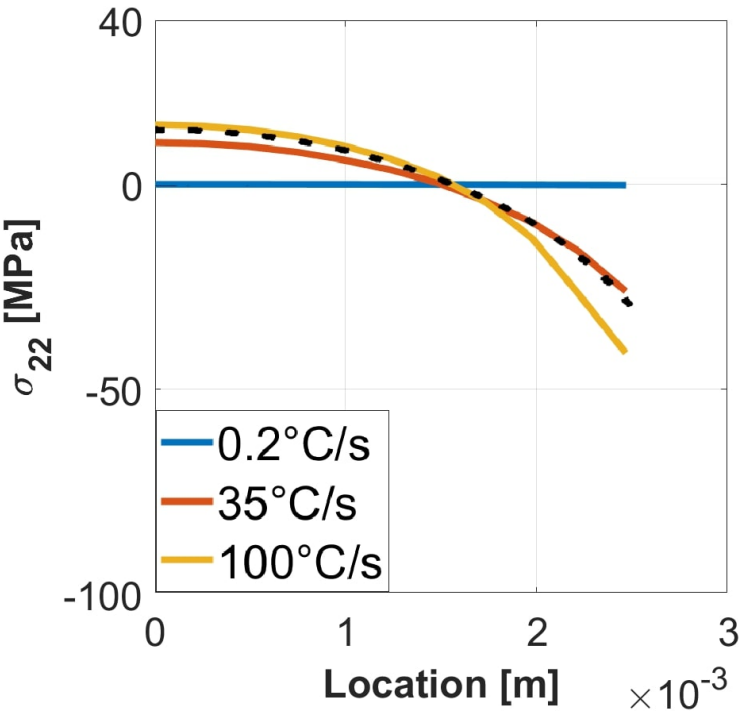

Figure 3.15: Final residual stress through the thickness in the transverse direction for different initial surfaces cooling rates. $Location = 0$ corresponds to the plate midplane. The black dotted line corresponds to the numerical result proposed by Chapman Chapman et al. (1990) for an initial cooling rate of $35°C/s$.

composition, enabled us to obtain uncoupled constitutive equations in which fibers and matrix contribution are easily recognized. The influence of the matrix shear modulus on the material parameters of the unidirectional composite was evaluated using analytical solutions derived in the literature. These results were used to justify the viscoelastic behavior only on the parameters affected by the deviatoric response of the matrix. A generalized Maxwell model was applied only to these terms, in agreement with the underlying physical mechanism. The temperature dependence was introduced through the time-temperature superposition principle using the Williams–Landel–Ferry shift function. Thermal strains were included using the same Cartan decomposition.

A first perspective of this work is to derive the constitutive law for the composite from homogenization of a fiber/matrix representative volume element, and to use the homogenized behavior to identify the material parameters introduced here. Simulating relaxation (strain-driven) and creep (stress-driven) tests, should enable us to identify the viscoelastic relaxation and creep functions in terms of the matrix be-

havior, which would give a complete description of the viscoelastic constitutive behavior of the composite.

As the model was developed in the framework of residual stresses and strains prediction for thermoplastic matrix composites, it will be used in further work to simulate the initial state of LATP manufactured parts. To this aim, it may be necessary to address in the model other physical mechanisms which could affect the development of residual stresses and strains, such as the effect of crystallization of the matrix on the mechanical behavior. The stress/strain decomposition proposed here should make this task relatively easy to achieve.

In Chapter 4, the one-dimensional heat transfer transient equation is used to describe the severe temperature gradients induced by the LATP processing. The temperature-dependent viscoelastic model developed here enables us to take into account the effects of LATP thermal history modeled in terms of residual stresses and strains within the manufactured structure. These effects, along with the combined effect of geometry and anisotropy seen in Chapter 2, will be assessed in Chapter 5 where simulations of the LATP manufacturing process are performed on several tubes.

4 - Thermal model of Laser Assisted Tape Placement

4.1 . Introduction

Among the sources of residual stresses and strains discussed in Chapter 1, the temperature gradients during manufacturing play a significant role. The viscoelastic model for the unidirectional composite, developed in Chapter 3, enables us to account for the temperature's effect, as it was shown through the last treated example in Section 3.6.2. In order to predict the residual stresses and strains associated to the Laser Assisted Tape Placement (LATP) process, therefore, we need an accurate thermal model of this process.

The LATP process (Schledjewski, 2009; Lukaszewicz et al., 2012) is used especially to fabricate tubes of different section types, pressure vessels and curved or flat plates. It can be summarized as a laying process with localized consolidation. Specifically, the machine winds up over a mandrel, or applies over a mold, a pre-impregnated tape of unidirectional fibers reinforced thermoplastic matrix composite. During this placement process, the composite tape is under tension, and a laser beam heats up the tape to be placed and the tapes previously deposed on the mandrel (which represent the consolidated substrate) to achieve consolidation. In order to achieve a better consolidation between tapes, a compaction roller applies a pressure transversely to the tapes.

The LATP thermal consolidation between the composite material tape and substrate is achieved through two phases, that occur consecutively: the heating phase and the consolidation phase.

In the heating phase, the machine heats up through a laser beam the inner surface of the tape being placed and the outer surface of the previously consolidated substrate. The heating zone is a rectangular spot, whose width exceeds the incoming tape width (the tape width can range from 10 mm to 300 mm for bigger structural composite parts) and whose length is a few tens of millimeters (up to 50 mm). Considering that the placement speed can range from 50 mm/s to 400 mm/s or more, the heating phase duration is very short, reaching an operating process time of 0.05 s. Therefore, a concentrated and limited area of the tape and the substrate exceeds the melting temperature of the thermoplastic matrix.

The consolidation phase begins when the incoming tape and sub-

strate, aided by the compaction roller, come into contact. In this phase, the laser heat source is removed, because the roller moved forward with the tape placement process, and tape and substrate cool down bonding together.

In order to manufacture the single layer of the structure, the machine applies and consolidates the unidirectional composite tapes side by side, following particular trajectories dependent on the designed geometry and the stacking sequence of the structure. Placing and consolidating layer over layer, the machine is able to fabricate the whole composite material structure.

During the manufacturing process, each composite material layer experiences several heating and cooling phases, depending on the number of layers of the structure, except for the last layer of the manufactured structure, which undergoes a single heating and cooling phase. In this scenario, the LATP process clearly generates a complex thermal history in the structure, characterized by high temperature gradients in every space direction (Toso et al., 2004; Hassan et al., 2005). This, in turn, induces a complex initial state in the manufactured structure (Parlevliet et al., 2006; Chapman et al., 1990; Sonmez and Hahn, 1997a; Baran et al., 2017; Sonmez et al., 2002). The assessment of the process induced residual stresses and strains is essential to predict the mechanical properties of the structure, therefore the modelling of the thermal processes involved in the LATP is crucial.

Several thermal models have been developed in the literature. Complex numerical three-dimensional heat transfer models were proposed by (Toso et al., 2004; Hassan et al., 2005), where the heat source used is a hot gas torch. Hosseini et al. (2021) and Stokes-Griffin and Compston (2015a) in their works studied the thermal problem of the laser assisted tape winding process, and they provided a 3D optical model coupled with a 2D heat transfer model. The effects of the heat source power and the placement velocity on the temperature evolution were studied through a 2D heat transfer model by Grove (1988); Stokes-Griffin et al. (2015), while Beyeler and Guceri (1988) and Sonmez and Hahn (1997a) included a heat generation term in the discussion in order to address for the heat release or heat absorption due to the crystallization of the thermoplastic matrix. An analytical solution to this thermal problem was proposed by Nejhad et al. (1991). However, later on it was pointed out by Pitchumani et al. (1996) and Tierney and Gillespie (2003) that the heat due to the crystallization can be neglected compared to the external heat input and the heat transfer through the material, suggesting that model simplifications can be taken into account.

Using these complex thermal models to assess the temperature

history experienced by the manufactured composite structure, and then applying the thermal history as input in order to evaluate the induced residual stresses and strains, would make the computational time too long compared to the industrial demand. Therefore, model simplifications have to be made.

The thermal problem is dominated by the through thickness conduction, as opposed to the layer in-plane conduction (Kok, 2018; Grouve, 2012), therefore we can expect more relevant temperature gradients along the structure's thickness with respect to the structure's plane (Grove, 1988; Tierney and Gillespie, 2003). Indeed, the tapes used in the LATP manufacturing process are extremely thin (the composite tapes used by CETIM are 0.16 mm thick) compared to the size of the structure. In particular, even if the thermal diffusivity in the fibers direction is one order of magnitude higher compared to the thermal diffusivity in the matrix direction, this heat transfer direction can be neglected due to the high placement speeds involved in the LATP manufacturing process, as highlighted by several authors (Grove, 1988; Grouve, 2012; Weiler et al., 2018).

Assuming a null initial state for the incoming ply, we can consider that the LATP process starts to generate residual stresses within the structure when the incoming ply and the substrate make contact. Therefore, in our discussion, a one-dimensional heat transfer equation is used to describe the consolidation phase of the LATP thermal problem, and the analytical solution of this problem is presented.

An analytical one dimensional heat transfer model solved by the finite-difference method was proposed by Colton and Leach (1992). Weiler et al. (2018) proposed two different one dimensional heat transfer models to describe both the heating phase and the consolidation phase of the laser assisted tape placement, while Dai and Ye (2002) modelled only the consolidation phase. Both works developed an analytical solution to the thermal problem, but they didn't include the thermal effect of the mandrel, which act as a heat sink especially in the first part of the manufacturing process, when the structure is still thin (up to 1 or 2 mm thick).

In the present work, the thermal effects of the mandrel and the ambient are accounted for, and they are considered as a convective mixed boundary conditions. The heat flux with the inner surface of the substrate is time and temperature dependent, since it is a function of the mandrel temperature, taken as constant, and the substrate temperature, which evolves in time. The same stands for the outer surface of the tape, which is exposed to air, supposed at constant temperature.

The initial condition for the present analytical model is the initial

temperature distribution in the thickness direction of the tape and the substrate at the end of the heating phase of the LATP. The heating phase itself is not modeled in our discussion. For this reason, where possible, the initial temperature distribution is extrapolated (through exponential fitting) from the numerical results of optical-thermal models present in the literature. Otherwise, the initial condition is assumed based on some common features of the litterature results.

Having an analytical solution of the consolidation phase of the LATP process, which takes into account its main physical mechanisms, turns out to be a big advantage in terms of computational time when thermo-mechanical simulations are performed over the whole manufactured structure.

In Section 4.2, the one-dimensional thermal model is presented. The effect of the mandrel as heat sink is introduced in the model as a mixed boundary condition. The second mixed boundary condition is introduced as convective heat flux with the ambient. In particular, the initial condition of the present thermal model is induced by the LATP heating phase, and thus derived through exponential fitting from numerical and experimental results presented in the literature. In Section 4.3, the analytical solution of the one-dimensional thermal model is derived.

Four case studies proposed in the litterature, including numerical and experimental results, are presented in Section 4.4. Each case study differs for the model considered, as well as for the number of deposed plies and, in some cases, the heating method. They enable us to study the common features of the temperature distributions induced by the heating phase of the LATP, as well as to compare our solution to the one provided by more complex 2D and 3D optical-thermal models. In particular, the analytical results are compared in Section 4.4.2 with the results from the literature in order to validate the proposed thermal model. Finally, the considerations made in Section 4.4.3 about the initial conditions enabled us to make a proposition for the initial temperature profile to be fed to the proposed one-dimensional thermal model.

Final comments are made in Section 4.5

4.2 . Thermal Model

During the manufacturing process of the composite structure, the LATP process generates temperature gradients across the whole structure. Hence, the thermal problem is described by a three-dimensional transient heat transfer equation. However, facing this problem would mean modeling the trajectories that the machine follows in order to

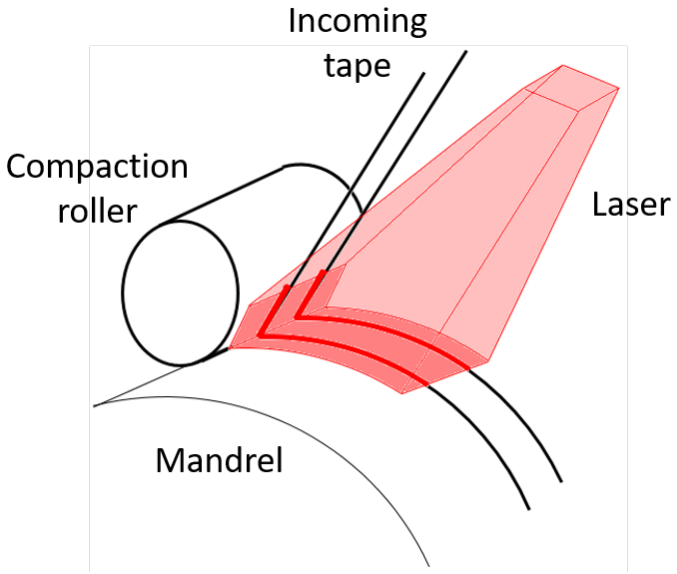

Figure 4.1: Laser assisted tape placement manufacturing process schematic image. The key LATP elements represented in the present Figure are: the laser heat source, the incoming tape, the compaction roller and the cylindrical mandrel. It can be noticed that the surface heated by the laser is dominant compared to the thickness of the tape.

manufacture the whole structure, and this is not feasible in terms of computational time.

As previously discussed, the laser heated surface is a rectangular spot, and its dimensions are at least one or two orders of magnitude bigger than the tape thickness (50mm for the size of the spot, against 0.125mm for the tape thickness, see Figure (4.1)). The heated area, which corresponds to the inner surface of the tape and to the outer surface of the substrate, reaches a almost uniform temperature, compared to the temperature distribution in the thickness direction (Stokes-Griffin and Compston, 2015a). Therefore, the LATP thermal problem is dominated by heat conduction in the thickness direction, where high temperature gradients are most likely to appear. Hence, the in-plane thermal problem is neglected, and a one dimensional transient heat transfer equation is used instead.

In terms of manufacturing process, such an assumption means that the single composite material layer of the structure is not characterized by several composite tapes placed side by side, but it is seen as manufactured in one go. The structure, on the other hand, is manufactured by placing each composite layer over the previously consolidated substrate. In this way, the notion of the trajectory that the machine needs

to follow in order to place the tape over the substrate is lost.

It follows that the heating phase and the consolidation phase involve the whole composite material layer and substrate. In particular:

1. **Heating phase.** In the heating phase (Kok, 2018; Weiler et al., 2018), the laser beam heats up the layer inner surface and the substrate outer surface. The heat is absorbed by the fibers that are on the surface, and then transferred by conduction through both the layer being placed and the substrate. In order to achieve the bond, in the following consolidation phase polymer chains have to cross the interface between the substrate and the tape. Therefore, the composite material is heated over the melting temperature of the thermoplastic matrix.

   The initial temperature distribution within the ply and the substrate, generated during the heating phase, is affected by several factors, such as: the optical and thermal properties of the composite material, the laser power, the laser beam inclination, the velocity of the tape placement, the temperature of the mandrel or the mold on which the machine is placing the tape, the elastic and thermal properties and the geometry of the consolidation roller (as it affects the shadow area at the nip point), and the geometry of the structure to be manufactured (which corresponds to the geometry of the mandrel/mold). Usually, a melted zone is expected at the ply/substrate interface, but the depth of this zone is quite challenging to predict numerically and to measure experimentally. In any case, the temperature distribution induced by the LATP strongly differs from the temperatures induced by the autoclave curing process, and high temperature gradients are likely to appear.

   The heating phase induces an initial temperature distribution within the ply being placed and the substrate. As soon as the two come into contact, and the heat source is removed, the cooling process begins.

2. **Consolidation phase.** In the consolidation phase, the thermoplastic matrix cools down and solidifies, and the layer being placed and the substrate bond together. This cooling process, as such, is deeply affected by the initial temperature distribution induced by the heating phase, discussed before. The main factors affecting the consolidation process are (Kok, 2018; Weiler et al., 2018; Hosseini et al., 2021): the thermal properties of the composite material, the thermal properties and the temperature of the consolidation roller, the mandrel and the surrounding environment. In

particular, the potential presence of voids at the interface, therefore the quality of the bond between previously consolidated layers, affects the thermal properties of the interfaces. In case of low bond quality, interfaces can have an insulating effect, as the polymer matrix has poor heat conduction properties. In modeling terms, this can be seen as a contact thermal resistances. This aspect is not considered in the following, where the heat conduction properties of the substrate are assumed to be uniform across the thickness. This amounts at considering a perfect bond between layers. As we mentioned earlier, the temperature distribution induced by the heating phase affects the consolidation phase, thus all the factors discussed before (in the heating phase) have a direct or an indirect impact on the cooling process of tape and substrate.

In the present work, the through-thickness transient heat transfer equation is used to describe the consolidation phase of the LATP, while the heating phase is not modelled. The initial condition of this model comes from the heating phase, therefore it will be derived from models describing the heating phase or from experimental results present in the literature. Once the initial condition has been derived, the thermal aspects included in the heating phase are indirectly included in our discussion. This strategy is used because a null initial state is assumed for the incoming layer and the build up of residual stresses and strains is considered to initiate as the layer being placed and the substrate make contact.

As regards the consolidation phase, we assume a perfect thermal contact, therefore a complete absence of interfacial voids. Due to the low thermal diffusivity of the polymeric compaction roller and to the high speed of the process, we assume that the outer surface of the placed composite layer is thermally exposed only to still air.

All the thermal material parameters used in the following discussion are taken as constant with temperature. The analytical solution of the model proposed here is also detailed.

4.2.1 . Heat transfer equation

The thermal problem in the consolidation phase is described by the following second-order parabolic partial differential equation with constant coefficients:

$$\frac{\partial T(z,t)}{\partial t} = k\frac{\partial^2 T(z,t)}{\partial z^2}, \qquad 0 < z < l, \tag{4.1}$$

where T is the temperature, t is time, z is the thickness coordinate and l is the total thickness of the manufactured structure. The thermal dif-

fusivity k of the composite material in the transverse direction can be written as function of the specific heat C, density ρ and the conductivity K, as follows: $k = \frac{K}{\rho C}$.

4.2.2 . Boundary conditions

The boundary conditions of the present model are represented as convective heat fluxes at the inner surface of the substrate and at the outer surface of the ply being placed, as follows:

$$-\left.\frac{\partial T}{\partial z}\right|_{z=0} + H_1\left(T(0,t) - T_1\right) = 0, \qquad z = 0 \tag{4.2}$$

$$\left.\frac{\partial T}{\partial z}\right|_{z=l} + H_2\left(T(l,t) - T_2\right) = 0, \qquad z = l, \tag{4.3}$$

where T_1 and T_2 are respectively the temperatures of the mandrel and of the air, while H_1 and H_2 are the heat transfer coefficients of the composite material respectively with the mandrel (h_1) and with the still air (h_2), scaled by the thermal conductivity K, and they can be written as: $H_1 = h_1/K$ and $H_2 = h_2/K$. The mandrel temperature (T_1) and the room temperature (T_2) are kept constant.

Equations (4.2) and (4.3) represent time-dependent heat fluxes between the mandrel (respectively, the air) at a prescribed constant temperature $T = T_1$ (respectively, $T = T_2$) and the substrate at temperature $T = T(0,t)$ (respectively, the incoming tape at temperature $T = T(l,t)$).

4.2.3 . Initial condition

As we said earlier, the initial condition is the initial temperature distribution of the ply being placed and the substrate. It can be written as follows:

$$T(z,0) = f(z), \qquad t = 0, \qquad 0 < z < l. \tag{4.4}$$

For the time being, the solution is developed for a general piecewise continuous function $f(z)$, re-written as:

$$f(z) = \begin{cases} f_1(z), & \text{for} \quad 0 < z < l_1 \\ f_2(z), & \text{for} \quad l_1 < z < l. \end{cases} \tag{4.5}$$

The function $f_1(z)$ in Equation (4.5) is a continuous function which represents the temperature distribution induced in the substrate by the heating phase of the LATP manufacturing process. On the other hand, $f_2(z)$ in Equation (4.5) is a continuous function that represents the temperature distribution in the layer being placed. Therefore, the

location $z = l_1$ represents the interface between the layer and the substrate.

In the present work, the initial temperature distribution of the layer and the substrate are derived by fitting other models or experimental results present in the literature (in order to obtained a continuous function for the incoming ply and substrate). In other cases, the initial condition is assumed by the author based on the common features observed in the initial temperature distributions discussed in the litterature.

4.3 . Analytical solution of the 1D heat transfer equation

Following the resolution steps presented by Carslaw and Jaeger (1959), the initial problem in Equations (4.1), (4.2), (4.3) and (4.4) can be decomposed into two sub-problems:

$$T(z,t) = u(z) + w(z,t), \tag{4.6}$$

where $u(z)$ is the solution to the steady state problem while $w(z,t)$ is the solution to the transient problem.

4.3.1 . Steady-state problem solution

The steady state problem takes care of the boundary conditions, and it can be written as follows:

$$\frac{d^2u(z)}{dz^2} = 0, \qquad 0 < z < l \tag{4.7a}$$

$$-\frac{du(0)}{dz} + H_1\left(u(0) - T_1\right) = 0, \qquad z = 0 \tag{4.7b}$$

$$\frac{du(l)}{dz} + H_2\left(u(l) - T_2\right) = 0, \qquad z = l. \tag{4.7c}$$

A solution of Equation (4.7a) is of the form:

$$u(z) = C_1 + C_2 z,$$

where C_1 and C_2 are constants that can be found by applying the boundary conditions (4.7b) and (4.7c). Indeed

$$\begin{aligned} -C_2 + H_1\left(C_1 - T_1\right) &= 0 \\ C_2 + H_2\left(C_1 + C_2 l - T_2\right) &= 0. \end{aligned}$$

Therefore the final solution to the steady state problem is:

$$u(z) = \frac{H_1T_1 + H_2T_2 + H_1H_2lT_1}{H_1 + H_2 + H_1H_2l} + \frac{H_1H_2(T_2 - T_1)}{H_1 + H_2 + H_1H_2l}z. \tag{4.8}$$

4.3.2 . Transient problem solution

The transient problem takes care of the time temperature evolution, and it can be written as follows:

$$\frac{\partial w(z,t)}{\partial t} = k\frac{\partial^2 w(z,t)}{\partial z^2}, \qquad 0 < z < l \tag{4.9a}$$

$$-\frac{\partial w(0,t)}{\partial z} + H_1 w(0,t) = 0, \qquad z = 0 \tag{4.9b}$$

$$\frac{\partial w(l,t)}{\partial z} + H_2 w(l,t) = 0, \qquad z = l \tag{4.9c}$$

$$w(z,0) = f(z) - u(z), \qquad t = 0, \qquad 0 < z < l, \tag{4.9d}$$

where $f(z)$ is the initial condition reported in (4.5).

We shall now provide the analytical expression of the solution to the transient thermal problem. The desired solution is sought in the form of separate variables (as in modal analysis). We consider the following expression:

$$w(z,t) = \sum_{n=1}^{\infty} w_n^z(z) w_n^t(t). \tag{4.10}$$

In order to satisfy Equation (4.9a), we need to have:

$$w_n^z(z) = A_n \cos(\alpha_n z) + B_n \sin(\alpha_n z) \tag{4.11a}$$

$$w_n^t(t) = e^{-k\alpha_n^2 t}, \tag{4.11b}$$

with A_n, B_n and α_n to be determined from the boundary conditions in Equations (4.9b) and (4.9c) and the initial condition in Equation (4.9d).

Substituting Equation (4.11a) in the boundary condition in Equation (4.9b), the following condition can be found:

$$B_n = \frac{H_1}{\alpha_n} A_n. \tag{4.12}$$

and, injecting it back in Equation (4.11a), we have:

$$w_n^z(z) = A_n X_n(z) = A_n \left(\cos(\alpha_n z) + \frac{H_1}{\alpha_n} \sin(\alpha_n z) \right). \tag{4.13}$$

Substituting Equation (4.11a) in the boundary condition in Equation (4.9c), we have:

$$A_n \left[(-\alpha_n \sin(\alpha_n l) + H_1 \cos(\alpha_n l)) + H_2 \left(\cos(\alpha_n l) + \frac{H_1}{\alpha_n} \sin(\alpha_n l) \right) \right] = 0. \tag{4.14}$$

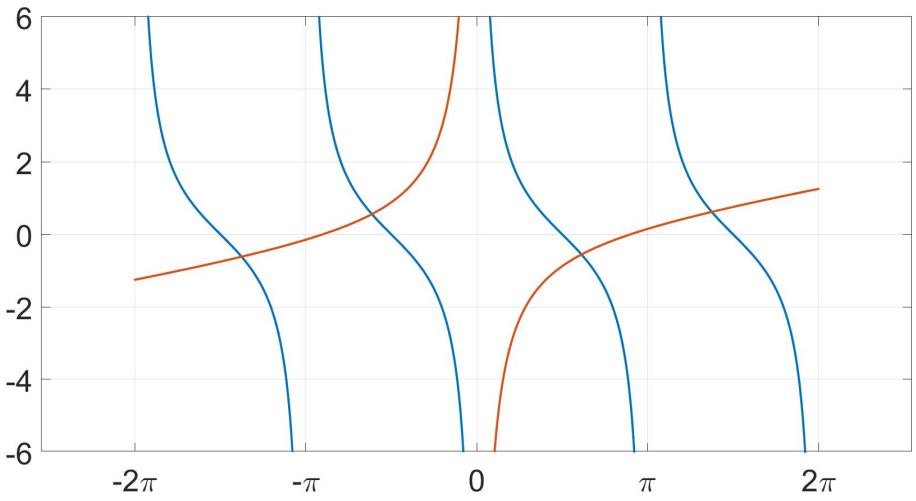

Figure 4.2: Typical solution of the transcendental equation

It follows:

$$\sin(\alpha_n l)\left(\frac{H_1 H_2 - \alpha_n^2}{\alpha_n}\right) + \cos(\alpha_n l)(H_1 + H_2) = 0. \tag{4.15}$$

Then:

$$\frac{H_1 + H_2}{H_1 \tan \alpha_n l} = \frac{\alpha_n^2 - H_1 H_2}{\alpha_n H_1}. \tag{4.16}$$

Rearranging the RHS, we have:

$$\frac{H_1 + H_2}{H_1 \tan \alpha_n l} = \frac{\alpha_n l}{H_1 l} - \frac{H_2 l}{\alpha_n l}. \tag{4.17}$$

If we set $\xi_n = \alpha_n l$, we obtain:

$$\frac{H_1 + H_2}{H_1 \tan \xi_n} = \frac{\xi_n}{H_1 l} - \frac{H_2 l}{\xi_n}. \tag{4.18}$$

As a result, in Equation (4.11a), A_n is an arbitrary constant while α_n is any non-zero root of Equation (4.18). Equation (4.18) is a transcendental equation, and the solution for α_n can be found graphically by plotting the LHS and RHS functions and intersecting the two curves.

It is clear from Figure (4.2), obtained using the following parameters:

$$H_1 = 25 \times 10^3 \text{ 1/m}, \quad H_2 = 12.5 \times 10^3 \text{ 1/m}, \quad l = 0.16 \times 10^{-3} \text{ m},$$

that the positive roots lie in one of each interval $(0, \pi)$, $(\pi, 2\pi)$,..., and the negative roots are equal in absolute value to the positive roots. Also, there are no repeated roots nor imaginary ones.

The remaining constant A_n is found so that it satisfies the initial condition in Equation (4.9d). In particular, similarly to the modal analysis, we can prove that the modes are orthogonal:

$$\int_0^l X_m X_n dz = 0 \quad \text{for} \quad n \neq m \tag{4.19a}$$

$$\int_0^l X_n^2 dz = \frac{1}{2\alpha_n^2}\left(H_2\left(\frac{\alpha_n^2+H_1^2}{\alpha_n^2+H_2^2}\right)+H_1+\left(\alpha_n^2+H_1^2\right)l\right) \quad \text{for} \quad n=m, \tag{4.19b}$$

The details of the proof, and in particular the determination of the value of $\int_0^l X_n^2 dz$, necessary for the following developments, is given in Appendix A.

Assuming that the initial condition $f(z)$ for the transient problem can be developed in an infinite series, we can rewrite it as:

$$w(z,0) = \sum_{n=1}^{\infty} A_n X_n(z) = f(z) - u(z), \tag{4.20}$$

which can be rewritten as:

$$\int_0^l X_m(z) w(z,0) dz = \int_0^l X_m(z) \sum_{n=1}^{\infty} A_n X_n(z) dz = \int_0^l X_m(z)\left(f(z)-u(z)\right) dz. \tag{4.21}$$

Following the orthogonality condition in Equation (4.19a) the constant A_n is computed as:

$$A_n = \frac{\int_0^l \left(f(z)-u(z)\right) X_n(z) dz}{\int_0^l X_n^2(z) dz}. \tag{4.22}$$

In particular, we have:

$$A_n = \frac{2\alpha_n^2}{H_2\left(\frac{\alpha_n^2+H_1^2}{\alpha_n^2+H_2^2}\right)+H_1+\left(\alpha_n^2+H_1^2\right)l} \int_0^l \left(f(z)-u(z)\right) X_n dz. \tag{4.23}$$

The final solution of the transient thermal problem is:

$$w(z,t) = 2\sum_{n=1}^{\infty} e^{-k\alpha_n^2 t} \frac{\alpha_n^2\left(\cos\alpha_n z + \frac{H_1}{\alpha_n}\sin\alpha_n z\right)}{H_2\left(\frac{\alpha_n^2+H_1^2}{\alpha_n^2+H_2^2}\right)+H_1+\left(\alpha_n^2+H_1^2\right)l} \int_0^l \left(f(z)-u(z)\right)\left(\cos\alpha_n z + \frac{H_1}{\alpha_n}\sin\alpha_n x\right) dz, \tag{4.24}$$

where $f(z)$ is the initial condition of the thermal model of the LATP manufacturing process presented in Equation (4.5), α_n are any positive roots obtained graphically from the transcendental equation (4.18) and $u(z)$ is expressed in Equation (4.8) which is the solution of the steady state problem.

The final time temperature distribution through the thickness can be obtained from Equation (4.6).

The function $f(z)$ in Equation (4.24) is the initial condition presented in Section 4.2.3, and it is a piece-wise continuous function therefore integrable function. In the next Section (4.4)) the initial condition $f(z)$ of the analytical thermal model just presented is obtained by exponential fitting of scattered points taken from other thermal models in the literature describing the LATP heating phase.

4.4 . Partial results: temperature evolution during ply deposition

The initial condition in Equation (4.5) is a piece-wise continuous function, and it represents the initial temperature distribution induced by the heating phase. The consolidation phase starts when the incoming ply and the substrate make contact, and if we assume a perfect thermal contact the temperature at the interface will be the same. The heating phase is not modeled in the present discussion, therefore the initial condition of the analytical model presented earlier is derived from literature results. In particular, the initial temperature function for the substrate and the incoming ply is obtained through an exponential fitting of scattered temperature points taken from thermal models results present in the literature.

Information about the initial temperature distribution of the incoming ply is not well detailed in the literature, however, a preliminary discussion can be made:

- the maximum temperature is reached at the interface between the incoming ply and the substrate, since it is the surface directly heated by the laser;
- the initial temperature distribution is almost constant (a low gradient temperature is expected), due to the rapidity of the placement process and to the low thermal diffusivity of the polymeric compaction roller, which acts almost as an adiabatic surface (Stokes-Griffin et al., 2015; Grouve, 2012).

The initial temperature distribution in the substrate depends on its thickness, as well as on the mandrel temperature. In the following, we

address the problem of the temperature evolution induced by the deposition of the last ply of a composite laminate. In this scenario, it is assumed that, at the end of the previous ply deposition, the laminate reaches its equilibrium temperature, which is the mandrel temperature, due to its high thermal diffusivity value. As it is shown in the following, the initial temperature of most of the laminate substrate is at the mandrel temperature, because of the high speed of the process and the limited depth that the laser heat source can reaches.

4.4.1 . Initial temperature distribution induced by different heating phase models

In the following, four case studies are addressed in order to understand the trend of the initial thermal distribution induced by the heating phase of the LATP as consolidation begins, and to validate the analytical consolidation thermal model presented before. Each case study is taken from the literature, and it describes the heating and the consolidation phase of the LATP presenting different initial temperature distributions. The final goal of the present Section is to validate the analytical thermal model comparing the analytical results with the numerical and experimental results present in the literature.

First case study

Grove (1988) presented a two-dimensional finite-element model of heat conduction associated with the tape laying manufacturing process of continuous fibers reinforced composite laminates with a laser heat source. Figure (4.3) depicts the derived initial temperature distribution induced by the laser heating phase of the 8^{th} ply placed over the consolidated substrate. The red dots, in Figure (4.3), are the temperature values obtained by Grove (1988) in a 1 mm thick carbon/PEEK laminate (each layer is 0.125 mm thick), where the imposed placement speed is 100 mm/s. The composite material parameters used by Grove (1988) are the following:

$$\rho = 1598 \text{ kg/m}^3, \quad C = 930 \text{ J/(kg K)}, \quad K = 0.5 \text{ W/(m K)}.$$

The substrate inner surface undergoes a heat conduction exchange with the mandrel, while the upper surface is exposed to free convection with still air. The following boundary conditions parameters were used (Grove, 1988):

$$h_1 = 500 \text{ W/(m}^2 \text{ K)}, \quad h_2 = 7 \text{ W/(m}^2 \text{ K)}, \quad T_1 = 20 \text{ °C}, \quad T_2 = 20 \text{ °C},$$

where h_1 and h_2 are the heat transfer coefficients and T_1 and T_2 are the constant temperatures respectively of the mandrel and the air, as

we discussed in Section 4.2. In Section 4.4.2, the same parameters will be used in the analytical model presented before to assess the time temperature evolution during cooling of the composite laminate. The analytical results will be then compared with the numerical results presented by Grove (1988).

It can be noticed, in Figure (4.3), that only the incoming ply and a small portion of the substrate exceed the melting temperature (T_m) of the thermoplastic matrix (PEEK, Cogswell (1992)). This is because the laser heat source is indeed highly localized. In Figure (4.3), the inner surface of the substrate is initially at the mandrel temperature, as discussed before in Section 4.4, because it is assumed that at the end of the previous deposition the laminate reaches its equilibrium temperature.

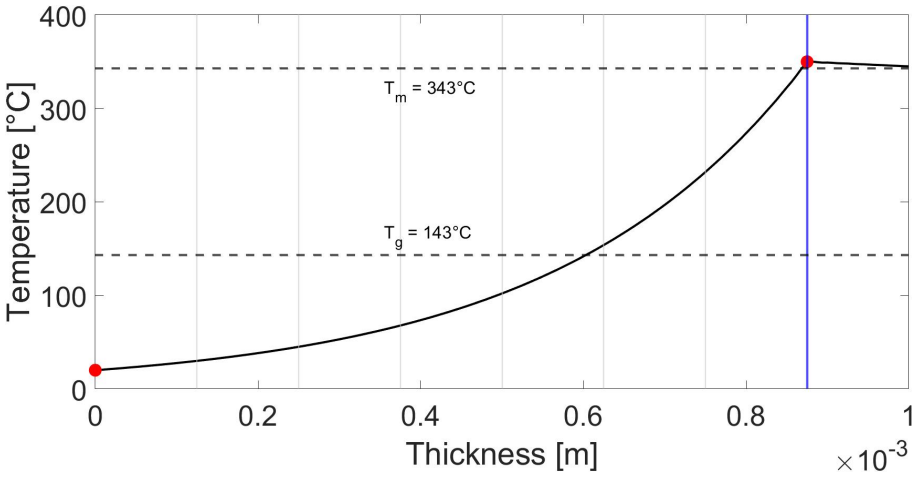

Figure 4.3: Initial temperature distribution induced by the 8^{th} ply placement. $Thickness = 0$ m is the interface between the substrate and the mandrel while $Thickness = 1 \times 10^{-3}$ m is the interface between the incoming ply and the air. Vertical lines represent the plies interfaces and the blue vertical line is the interface between the incoming 8^{th} ply and the substrate. The red dots are the interfaces temperatures assessed by Grove (1988).

The incoming ply temperature distribution is assumed, based on the discussion presented in Section 4.4, due to lack of data in this sense. In particular, the temperature function of the incoming layer is made so that the temperature exceeds the melting temperature of the polymeric matrix PEEK (Grouve, 2012; Stokes-Griffin et al., 2015). On the other hand, this hypothesis does not seem to significantly affect the overall time temperature evolution in the laminate, as we will see later.

Second case study

Kok (2018) used a thermal-optical model in order to study the effects of a compliant roller and of the laser inclination on the heating phase on a AS-4/PEEK laminate. Then, a one-dimensional thermal model solved by the finite difference method was used by Kok (2018) to evaluate the temperature distribution within the laminate during the consolidation phase, and its results were experimentally validated.

The initial temperature distribution depicted in Figure (4.4) is obtained through an exponential fitting of the red dots as shown in Section 4.4.1 in Figure (4.3). The red dots are the temperature values, numerically assessed and experimentally validated by Kok (2018), induced in a 1.8 mm thick carbon/PEEK laminate (each layer is 0.15 mm thick) by the laser heating phase of the 12^{th} ply placed over the consolidated substrate, imposing a placement speed of 100 mm/s.

Due to the complexity of the optical-thermal model used by Kok (2018), numerous parameters are required to perform the numerical simulation. These includes for example the laser spot size dimensions, the roller geometry, the refractive index of the composite material, the emissivity, the heat flux distribution in the tape and the substrate etc. In our discussion, the parameters we are interested in are the ones that we can use later to compare our analytical results with numerical ones presented by Kok (2018). In particular, the composite material parameters used are (Kok, 2018)

$$\rho = 1560 \text{ kg/m}^3, \quad C = 1425 \text{ J/(kg K)}, \quad K = 0.72 \text{ W/(m K)},$$

while the boundary conditions parameters used are (Kok, 2018):

$$h_1 = 500 \text{ W/(m}^2 \text{ K)}, \quad h_2 = 20 \text{ W/(m}^2 \text{ K)}, \quad T_1 = 20 \text{ °C}, \quad T_2 = 20 \text{ °C}.$$

In his numerical thermal model, Kok (2018) included also the heat flux between the incoming tape and the compaction roller. However, this thermal effect, as we will see in the following, does not seem to affect in a significant way the overall thermal response in the laminate (Stokes-Griffin et al., 2015; Grouve, 2012).

The temperatures of the interface between the substrate and the incoming ply in Figure (4.3) and in Figure (4.4) are quite different (roughly 350°C and 400°C respectively for Grove (1988) and Kok (2018)). Nevertheless, it can be noticed that, in both cases, only the first three layers of the laminate exceed the glass transition temperature (T_g) of the polymeric matrix PEEK. This is because in the laminate simulated by Grove (1988) each ply is 0.125 mm thick, compared to the laminate studied by Kok (2018) where each ply is 0.15 mm thick.

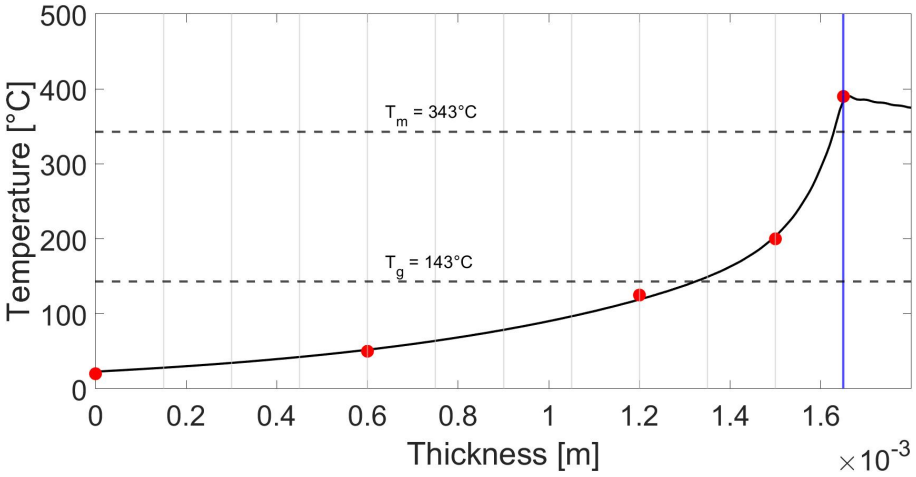

Figure 4.4: Initial temperature distribution in the laminate thickness induced by the 12^{th} ply placement. $Thickness = 0$ m is the interface between the substrate and the mandrel and $Thickness = 1.8 \times 10^{-3}$ m is the interface between the incoming ply and the air. Vertical lines represent the plies interfaces and the blue vertical line is the interface between the incoming 12^{th} ply and the substrate. The red dots are the interfaces temperatures assessed by Kok (2018).

Third case study

In the third case study, Sonmez and Hahn (1997a) present a temperature distribution induced by the heating phase of the 21^{th} ply placement with two different heat sources (Figure (4.5)): the hot gas torch and the laser. The black triangles and the red dots in Figure (4.5) are the temperature values caused by the laser heat source and by the hot gas torch heat source respectively. These values are assessed by Sonmez and Hahn (1997a) through a heat transfer analysis strongly coupled with a crystallization kinetics model carried out using a finite element method.

The numerical simulations were performed using numerous parameters, including the densities of the amorphous and the crystalline phases, the heat of melting the semi-crystalline matrix, etc. However, the material is the same as the one analyzed in the second case study, and the parameters we are interested in are those presented in the Section 4.4.1. The imposed placement speed is 50 mm/s.

The following boundary conditions parameters were used (Sonmez and Hahn, 1997a):

$$h_1 = 400 \text{ W/(m}^2 \text{ K)}, \quad h_2 = 10 \text{ W/(m}^2 \text{ K)}, \quad T_1 = 25 \text{ °C}, \quad T_2 = 25 \text{ °C}.$$

Sonmez and Hahn (1997a) included also the heat flux between the

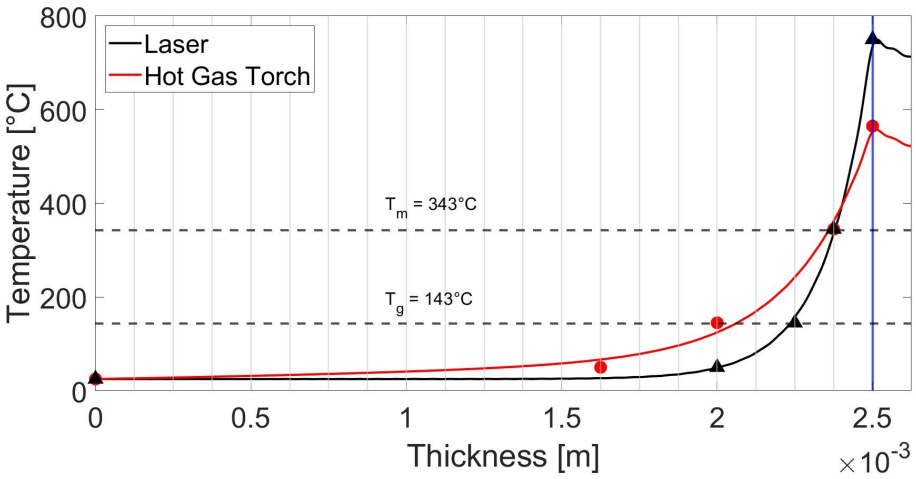

Figure 4.5: Initial temperature distribution in the laminate thickness induced by the 21^{th} ply placement with two different heat source: the hot gas torch and the laser. Vertical lines represent the plies interfaces. The red dots and the black triangles are the interfaces temperatures assessed by Sonmez and Hahn (1997a) using respectively the gas torch and the laser. $Thickness = 0$ m is the interface between the substrate and the mandrel and $Thickness = 2.625 \times 10^{-3}$ m is the interface between the incoming ply and the air.

incoming tape and the compaction roller in their numerical thermal model, . However, this thermal effect, as we will see in the following, does not seem to affect in a significant way the overall thermal response in the laminate (Stokes-Griffin et al., 2015; Grouve, 2012).

The carbon/PEEK composite laminate simulated by Sonmez and Hahn (1997a) is 2.625 mm thick and the thickness of each ply is 0.125 mm. The temperature functions depicted in Figure (4.5) are obtained, as always, through an exponential fitting.

In Figure (4.5), the temperature at the interface between the substrate and the incoming ply reaches $750°$C which is a really high temperature for the polymeric matrix considering that its melting temperature is $343°$C. However, as we will see in the following, the time spent at this temperature is very low (much less than a second). Therefore it is not considered very problematic for the polymer in terms of its degradation, as pointed out by Sonmez and Hahn (1997a) and Cogswell (1992).

It is interesting to compare the temperature distributions in Figure (4.5) induced by the laser and the hot gas torch. The highly localized nature of the laser heat source causes only the first three layers of the laminate to exceed the glass transition temperature, and only the first two layers to exceed the melting temperature. This particular case is

different from the two case studies seen before, in which only the incoming ply and a small portion of the substrate exceed the melting temperature (see Figures (4.3) and (4.4)). The use of the hot gas torch heat source makes the temperature of the interface between the first ply and the substrate much lower (roughly 560°C) with respect to the temperature reached by the same interface with the laser heat source (in Figure (4.5)). On the other hand, with the hot gas torch, the first five plies of the laminate exceed the T_g. This will change in a significant way the time temperature evolution of the laminate, as shown in the following.

Fourth case study

The last case study is the temperature induced by a hot gas torch at the 21^{th} ply placement over a preheated mandrel at $150°$C. The material, the laminate and all the parameters values are the same as in the Section 4.4.1. The temperature distribution is depicted in Figure (4.6).

This case study was addressed because it appears to be interesting from an industrial application point of view. A structure made with the LATP manufacturing process does not necessarily has a uniform crystallization rate (due to strong thermal gradients the structure does not stay long enough above the crystallization temperature (Tierney and Gillespie, 2004)). To overcome this problem, a preheated mandrel to a temperature higher than the glass transition temperature is sometimes used, thus allowing a more uniform crystallization in the structure.

In Figure (4.6), the temperature at the interface between the incoming ply and the substrate was derived through exponential fitting since it is not provided by Sonmez and Hahn (1997b). This temperature reaches roughly 650°C, which could be a problem in terms of the degradation of the polymeric matrix. However, also in the present case study, as it is shown in the following, the time spent at this temperature is less than a second. Therefore it is not considered very problematic for the polymer.

Compared to the previous cases, in this case the whole laminate is at a temperature higher than the T_g, since the mandrel is preheated to 150°C. Moreover, in the present case the heat source goes deeper into the laminate (because the mandrel is preheated), and the first three layers exceed the melting temperature.

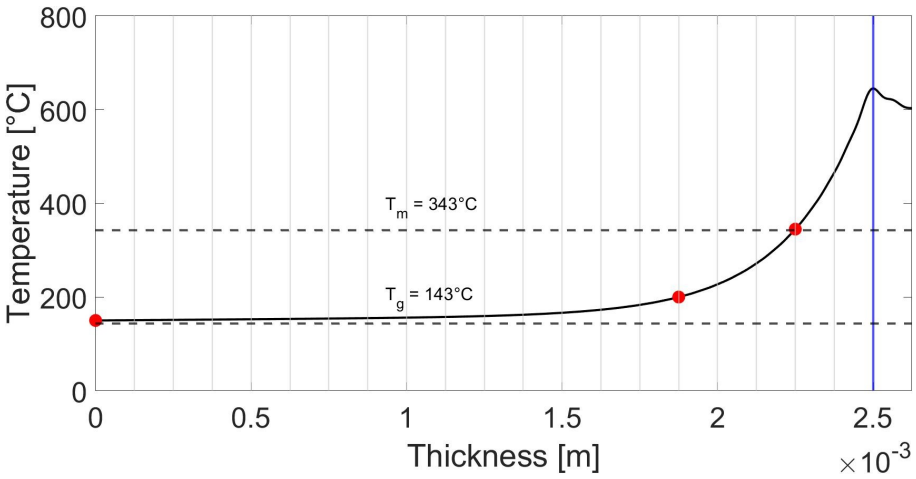

Figure 4.6: Initial temperature distribution induced by the 21^{th} ply placement over a preheated mandrel at 150°C. The blue vertical line represent the interface between the incoming 21^{th} ply and the substrate. The red dots are the temperatures values assessed by Sonmez and Hahn (1997a). $Thickness = 0$ m is the interface between the substrate and the mandrel and $Thickness = 2.625 \times 10^{-3}$ m is the interface between the incoming ply and the air.

4.4.2 . Time temperature evolution in the composite material laminate: a comparison

First case study results

The results assessed by Grove (1988), as well as by the present model, for the consolidation phase in the first case study, are depicted in Figures (4.7) and (4.8). In particular, assuming that the first ply was already welded on the mandrel, the superimposed temperature histories experienced by the inner surface of the substrate (Figure (4.7)) and by the surface at 0.125 mm from the mandrel (Figure 4.8) are represented during the placement of different plies (first, second placement, third and seventh placements).

In particular, in Figure (4.7), the curve called "2 plies" represents the thermal response of the interface between the mandrel and the substrate (which is the inner surface of the substrate) after the first placement. Therefore, in Figure (4.7) left the curves called "3 plies", "4 plies" and "8 plies" represent the temperature history experienced by the inner surface of the mandrel respectively after the second placement, the third placement and the seventh placement. The same stands for Figure (4.8), where the temperature history is experienced by the surface at 0.125 mm from the mandrel.

The parameters used are presented in Section 4.4.1. The initial con-

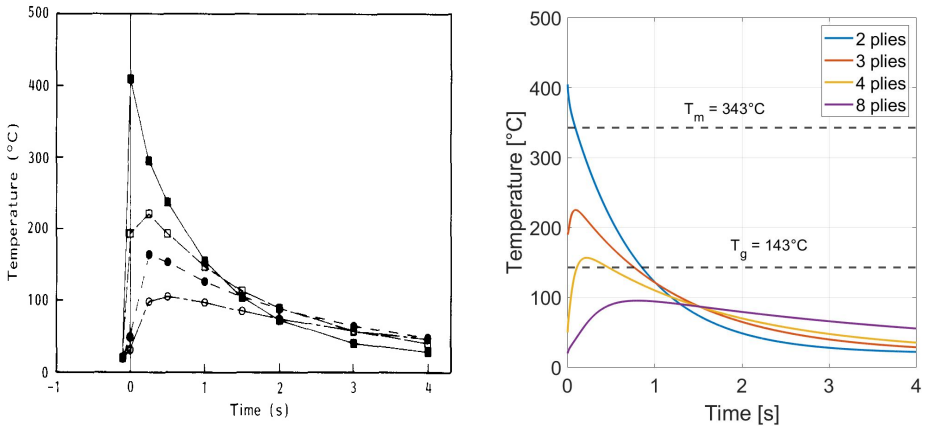

Figure 4.7: Superimposed thermal responses of the inner surface of the substrate fabricated at 100 mm/s placement speed. Grove (1988) numerical results (left): (■) 2 plies; (□) 3 plies; (●) 4 plies; (○) 8 plies. The present analytical model results (right).

ditions for the present model are obtained through exponential fitting of the temperature values in Figure (4.7) left and in Figure (4.8) left at the $Time = 0$ s, as well as the temperature at the interface between the incoming ply and the substrate. In particular, the initial condition used to obtain the curves called "8 plies" is the one depicted in Figure (4.3.)

It is possible to notice, in Figure (4.7) and in Figure (4.8), how the numerical results presented by Grove (1988) and the analytical results are in very good agreement. In particular, the laminate at the inner surface (in Figure (4.7)) exceeds the melting temperature of the polymeric matrix only during the first pass, and it exceeds the glass transition temperature during the first three passes. The same consideration can be made for the Figure (4.8).

In the placement of the second ply (the curve called "2 plies"), the laminate is subjected to a high cooling rate, up to 300° C/s. The reason underneath this phenomenon is the low thermal inertia of the laminate, due to its small thickness (0.25 mm). For this reason, the thermal heat flux towards the mandrel is relevant and the laminate temperature tends towards the mandrel temperature. In this scenario, in the thermal modeling approach of the laser assisted tape placement it is essential to consider the heat flow between the substrate and the mandrel, which has a significant thermal effect especially in the placement of the first plies.

As the ply placement process progresses, the laminate's thermal inertia increases (the laminate get thicker at each ply deposition) and

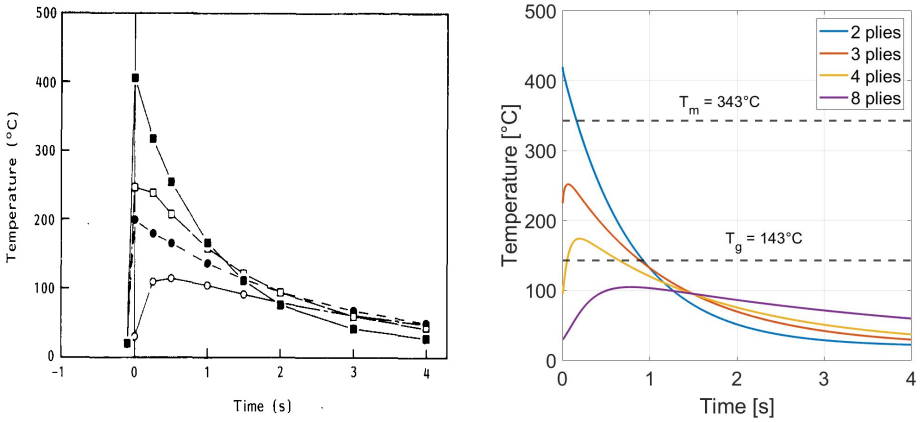

Figure 4.8: Superimposed thermal responses of the surface at 0.125 mm from the substrate. Grove (1988) numerical results (left): (■) 2 plies; (□) 3 plies; (●) 4 plies; (○) 8 plies. The present analytical model results (right).

the thermal heat flux towards the mandrel becomes less and less relevant. Consequently, the required cooling time increases, since the 8 plies laminate will not undergo to the same cooling rate as the 2 plies laminate. The time temperature evolution for different interfaces of the laminate during the 8^{th} ply placement is depicted in Figure (4.9). Looking at these results, it is possible to compare the cooling rates of the interface between the substrate and the incoming ply in a 2 plies laminate, which is the curve "2 plies" in Figure (4.8), and in a 8 plies laminate, which is the curve "1^{st} interface" in Figure (4.9). In the first case, in Figure (4.8), the cooling rate reaches $300°$ C/s, while in the second case, in Figure (4.9), the cooling rate reaches $200°$ C/s. This difference in cooling rates can be considerably increased if the convective heat flux coefficient between the mandrel and the substrate is increased up to $h_1 = 4000$ W/(m^2 K), as proposed for example by Hosseini et al. (2021) in his numerical model.

Figure (4.10) depicts the contour plot of the time temperature evolution of the laminate in the thickness direction during placement of the 8^{th} ply, assessed by the analytical model. As illustrated in Section 4.4.1 in Figure (4.3), the incoming ply and a small portion of the substrate exceed the polymer melting temperature, and the first three plies reach a temperature over $200°$ C. The top surface of the laminate is subjected to a higher cooling rate with respect to the base of the laminate, since the former reaches higher temperatures during the heating phase.

Figure (4.10) is derived assuming a stationary placement process. Indeed, during the placement process, each in-plane point of the layer

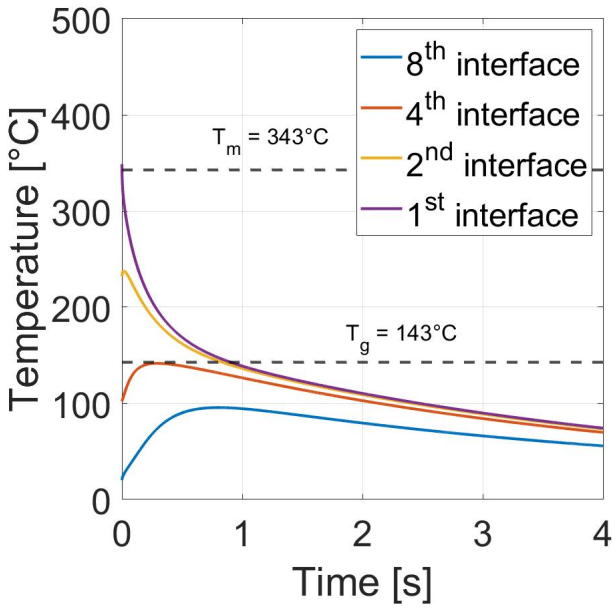

Figure 4.9: Time temperature evolution for different plies interfaces at the placement of the 8^{th} ply. The first interface corresponds to the interface between the incoming ply and the substrate. The interface between the substrate and the mandrel is the 8^{th} interface.

being placed and of the substrate undergoes the same thermal history, but at different times. This means that (as it is observed in Figure (4.10)), if a given point "A" at a certain distance from the mandrel is heated at the time $t = 0$ s, after 4 seconds the same point "A" reaches a temperature just below 100° C. Meanwhile, the machine covered a distance during the 4 seconds, and it is now heating another point, point "B", located in the same plane as the point "A". The point "B", heated at the time $t = 0$ s, will experiences the same thermal history as the point "A", and after 4 seconds its temperature will be just below 100° C. Therefore, in Figure (4.10), the abscissa can also be seen as the distance covered by the machine during the placement process, and the plot depicts the temperature evolution in the thickness direction, but also in the length direction of the laminate. In this scenario, fixing the placement speed, the time and the length (intended as distance in the plane from the heat source) are interchangeable.

From Figure (4.10), another important consideration can be made. It can be seen that the thermal gradients in the thickness direction are significantly more important than the thermal gradients in the length of the laminate, since there are three orders of magnitude difference between the two. This further justifies the choice of developing a one-dimensional thermal model. The same considerations can be made

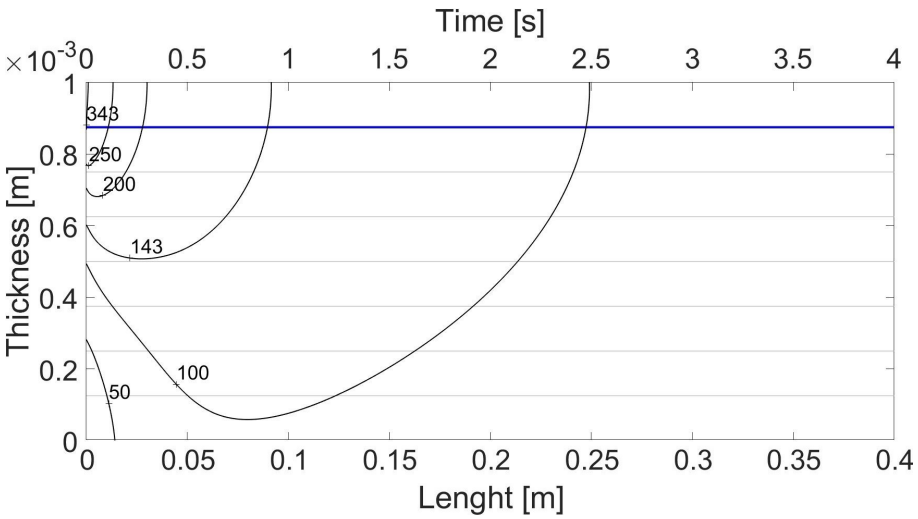

Figure 4.10: Temperature evolution in time and in the length of the laminate for each ply at the 8^{th} ply placement. The abscissa indicates the time and the corresponding distance covered by the machine during the placement process at a speed of 100 mm/s. The black curves are the iso-temperature curves and the blue horizontal line is the interface between the substrate and the 8^{th} ply. $Thickness = 0$ m is the interface between the substrate and the mandrel while $Thickness = 1 \times 10^{-3}$ m is the interface between the incoming ply and the air.

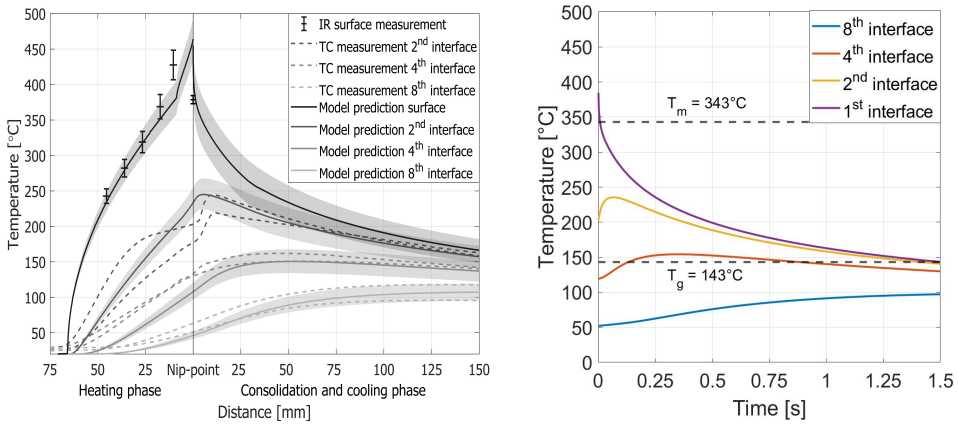

Figure 4.11: Temperature evolution for different plies interfaces at the placement of the 12^{th} ply. The first interface corresponds to the interface between the incoming ply and the substrate. Numerical and experimental results of the heating and the consolidation phases presented by Kok (2018) (left) and the results of the consolidation phase modelled analytically in the present work (right).

with the results shown in the following with different thermal histories.

Second case study results

The time temperature evolution for different interfaces during placement of the 12^{th} ply, at a placement speed equal to 100 mm/s, are shown in Figure (4.11). The experimental and numerical results of the heating and consolidation phases, presented by Kok (2018), are shown in Figure (4.11) left, while the results of the consolidation phase modelled in the present work in an analytical fashion are depicted in Figure (4.11) right. The results in Figure (4.11) right are assessed using the parameters presented in Section 4.4.1 and the initial condition presented in Figure (4.4).

In Figure (4.11) left, the abscissa indicates the distance from the nip-point, which is the point where the heating phase ends and the consolidation phase starts. In Figure (4.11) left, at the nip-point left the incoming ply and the substrate are not in contact and the laser heats up the two surfaces separately. The substrate temperature starts to increase when the substrate meets the laser spot. Furthermore, based on what is said in Section 4.4.2 about Figure (4.10), fixing the placement speed at 100 mm/s, the thermal history experienced by two points belonging to the same laminate plane is the same, but temporally out of phase. In this scenario, the layer placement process can be considered stationary. Therefore, in Figure (4.11) left, the abscissa indicates the distance covered by the heating source, while in Figure (4.11) right, the abscissa

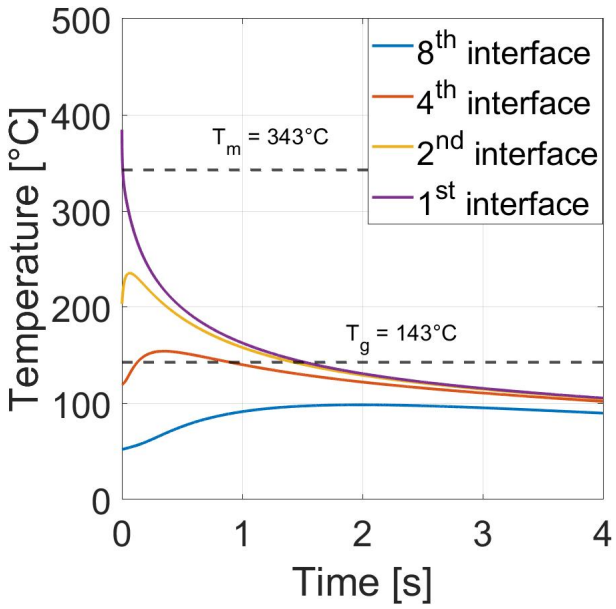

Figure 4.12: Time temperature evolution for different plies interfaces at the placement of the 12^{th} ply. The first interface corresponds to the interface between the incoming ply and the substrate. The interface between the substrate and the mandrel is the 12^{th} interface.

indicates the time needed by the heat source to cover that distance.

The results for the temperature distribution induced by the LATP consolidation phase modelled by Kok (2018) in Figure (4.11) left and analytically by the present work are in bery good agreement, and the cooling rate shown by the first interface between the incoming 12^{th} ply and the substrate is roughly 200° C/s.

Comparing the time temperature evolution of the first interface in Figure (4.9), where the laminate thickness is 1 mm, and in Figure (4.12), where the laminate thickness is 1.8 mm, the two curves show almost the same initial cooling rate (roughly 200°C/s), proving that the thermal effect of the mandrel decreases significantly as soon as the substrate become thick enough (1 mm) and the thermal problem is dominated by the conduction through the laminate thickness. Moreover, increasing the laminate thickness (the thickness is almost doubled between the two case studies) increases also the laminate thermal inertia, which increases the time needed to cool down (see Figure (4.9) and Figure (4.12)).

The temperature evolution in time and along the length of the laminate during the placement of the 12^{th} ply is shown in Figure (4.13). As it was discussed in the previous Section, a point in Figure (4.13) represents the temperature of a point in the thickness of the laminate at a

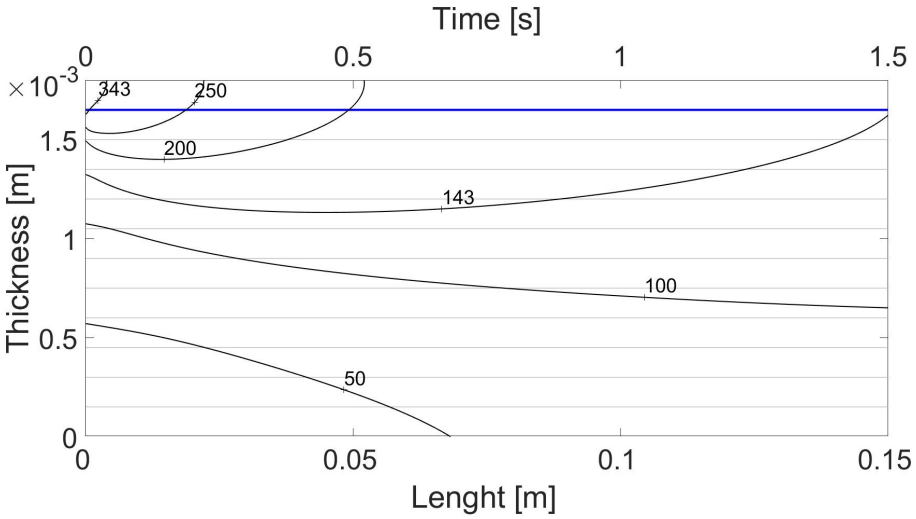

Figure 4.13: Temperature evolution in time and in the length of the laminate for each ply at the 12^{th} ply placement. The abscissa indicates the time and the corresponding distance covered by the heat source during the placement process at a speed of 100 mm/s. The black curves are the iso-temperature curves and the blue horizontal line is the interface between the substrate and the 12^{th} ply.

given time, but also at a certain distance from the heating source along the length of the laminate. This is possible because we assume a stationary placement process.

Third case study results

The temperature fields in the laminate induced respectively by the laser heat source and the hot gas torch heat source at the 21^{th} ply placement are depicted in Figures (4.14) and (4.15). In particular, the curves assessed numerically by Sonmez and Hahn (1997a) are shown on the left, while the analytical results assessed using the initial conditions in Figure (4.5) and the parameters in Section 4.4.1 are shown on the right.

Sonmez and Hahn (1997a) present a numerical model to describe the heating and the consolidation phase of the thermoplastic composite tape placement process. In Figures (4.14) and (4.15) left, for negative values of the abscissa the substrate and the incoming ply are not in contact, and the temperature starts to rise when they encounter the laser spot. Comparing the heating phases in Figures (4.14) and (4.15) left, in the first case the length heated by the laser is much more concentrated than the length heated in the second case by the hot gas torch. The laser heat source is much more localized compared to the hot gas torch. Therefore, the initial conditions presented in Figure (4.5)

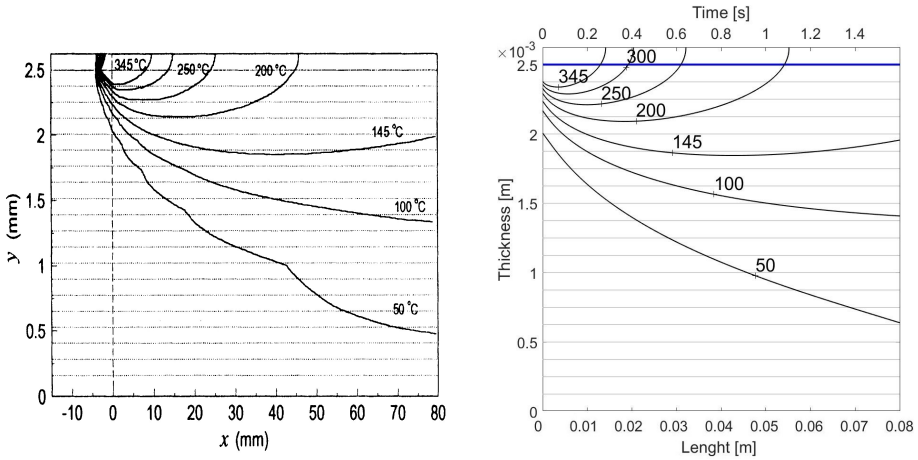

Figure 4.14: Temperature field in the laminate induced by the laser heat source at the 21^{th} ply placement. Numerical results presented by Sonmez and Hahn (1997a) (left) and the present analytical model results (right). The abscissa indicates the time and the corresponding distance covered by the machine during the placement process at a speed of 50 mm/s. The black curves are the iso-temperature curves and the blue horizontal line is the interface between the substrate and the 21^{th} ply. $Thickness = 0$ m is the interface between the substrate and the mandrel while $Thickness = 2.625 \times 10^{-3}$ m is the interface between the incoming ply and the air.

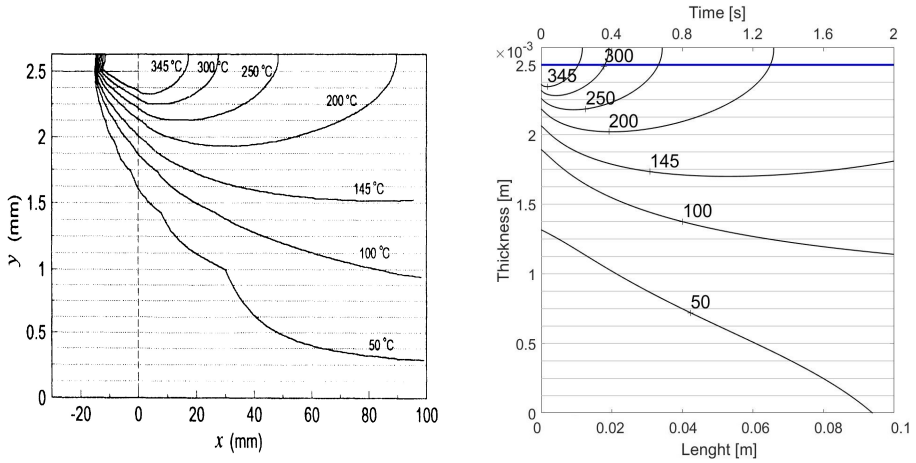

Figure 4.15: Temperature field of the laminate induced by the hot gas torch heat source at the 21^{th} ply placement. Numerical results presented by Sonmez and Hahn (1997a) (left) and the present analytical model results (right). In the abscissa we have the time and the corresponding distance covered by the machine during the placement process at a speed of 50 mm/s. The black curves are the iso-temperature curves and the blue horizontal line is the interface between the substrate and the 21^{th} ply. $Thickness = 0$ m is the interface between the substrate and the mandrel while $Thickness = 2.625 \times 10^{-3}$ m is the interface between the incoming ply and the air.

for the laser and for the hot gas torch differ so much, because the heat spreads much more by conduction in the thickness of the laminate when the heat source is the hot gas torch.

The analytical results for the present model, in Figure (4.14) right, are in very good agreement with the numerical results for the laser heat source presented by Sonmez and Hahn (1997a) in Figure (4.14) left.

The analytical results in Figure (4.15) right are not in very good agreement with the numerical results for the hot gas torch heat source presented by Sonmez and Hahn (1997a) in Figure (4.15) left. The biggest difference can be noticed in the deeper layers of the laminate, where temperatures are lower (the temperature here ranges between 50° C and 100° C), while in the superficial layers of the laminate, where temperatures are higher (above the T_g where the composite behavior is viscoelastic), the results are in very good agreement. In Figure (4.15) left, the heat reaches by conduction the lowest layers of the laminate without reaching the interface with the mandrel, but stopping about two layers before. On the other hand, in Figure (4.15) right, the layer in contact with the mandrel is also heated by conduction. The reason is probably because the exponential fitting adopted for the initial condition of the present model (Figure (4.5)) does not exactly match the numerical results presented by Sonmez and Hahn (1997a). No further investigation has been done, as this is not the main goal of the present work, and because the biggest differences between the results in Figure (4.15) are in a temperature range not relevant in terms of manufacturing process induced residual stresses and strains, since the temperature gradients here are not relevant.

The time temperature evolution induced by the laser and the hot gas torch for different interfaces during placement of the 21^{th} ply, assessed analytically by the present model, are depicted in Figure (4.16). The initial cooling rate for the first interface between the substrate and the incoming ply heated by the laser in Figure (4.16) left is approximately 550° C/s, while the initial cooling rate for the first interface heated by the hog gas torch in Figure (4.16) right is roughly 360° C/s. These are very high when compared to previous case studies. However, this was expected, since the initial temperature of the interface between the incoming ply and the substrate is 750° C for the laser and 560° C for the hot gas torch (see Figure (4.5)).

Although the temperature at the first interface of the laminate is much higher in the case of the laser heat source than in the case of the hot gas torch heat source, we saw previously in Figure 4.5 that the heat gas torch heats up the laminate more deeply with respect to the laser and this, in addition to the thermal inertia of the laminate, means that

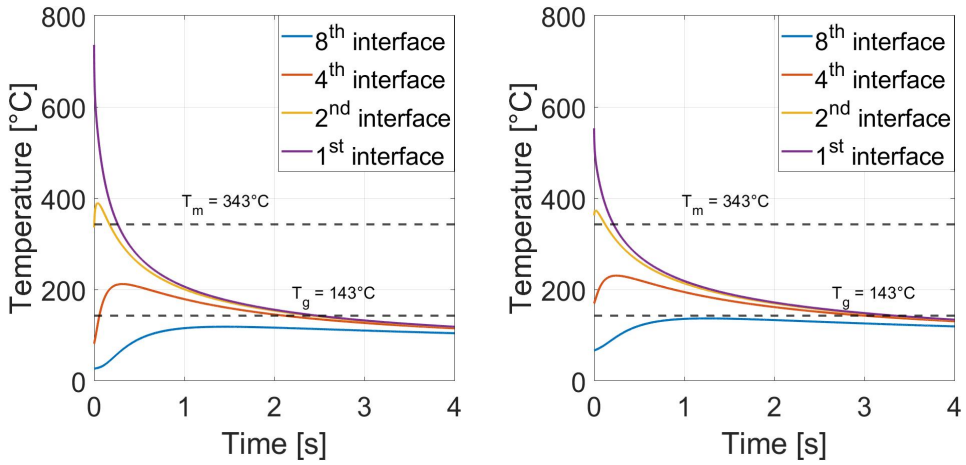

Figure 4.16: Analytical time temperature evolution induced by the laser (left) and by the hot gas torch (right) for different plies interfaces at the placement of the 21^{th} ply. The first interface corresponds to the interface between the 21^{th} incoming ply and the substrate.

the laminate takes longer to cool down, as it can be observed comparing Figure (4.16) left with Figure (4.16) right. For the same reason, the cooling time in this case (Figure (4.16)) turns out to be way bigger than the cooling time shown in Figure (4.9) and in Figure (4.12).

Fourth case study results

The temperature distribution within the laminate as function of time and distance is depicted in Figure (4.17). The numerical results presented by Sonmez and Hahn (1997a) are shown in Figure (4.17) left, while the analytical results are depicted in Figure (4.17) right. The initial temperature distribution used in the present case to assess analytically the time temperature distribution at the 21^{th} ply placement over a preheated mandrel at 150° C is the initial condition depicted in Figure (4.6).

Exceeding the T_g of the polymeric matrix during the whole manufacturing process, the structure reaches the maximal crystallization rate (Chapman et al., 1990; Cogswell, 1992). The results shown in Figure (4.17) right (assessed by the present analytical thermal model) are in good agreement with the results presented by Sonmez and Hahn (1997a) in Figure (4.17) left, showing that the heat generated or absorbed during the crystallization process of the thermoplastic matrix is a thermal effect that can be neglected , as compared to the effect of thermal conduction in the laminate or the heat flow to the mandrel, in the modeling of the LATP thermal problem (Pitchumani et al., 1996; Tierney and Gillespie, 2003).

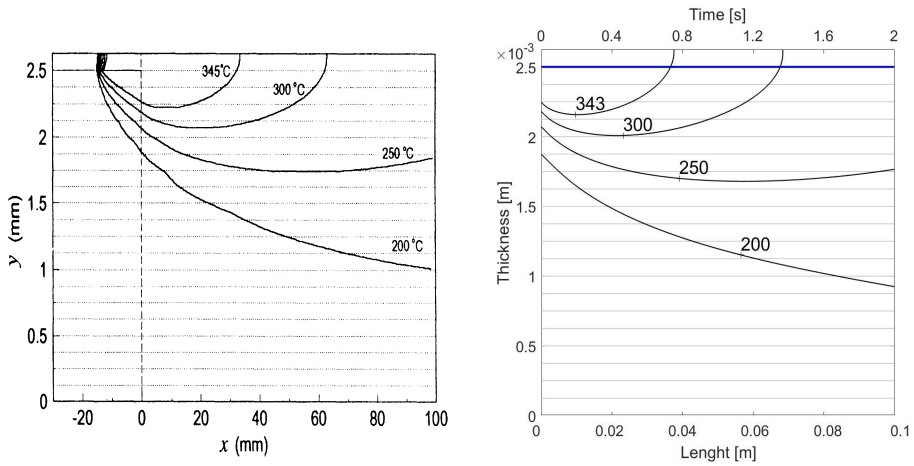

Figure 4.17: Temperature evolution in time and in the length of the laminate for each ply at the 21^{th} ply placement over a preheated mandrel at 150° C. The heat source used is the hot gas torch. The abscissa indicates the time and the corresponding distance covered by the machine during the placement process at a speed of 50 mm/s. The black curves are the iso-temperature curves and the blue horizontal line is the interface between the substrate and the 21^{th} ply. Numerical results presented by Sonmez and Hahn (1997a) (left) and the present analytical model results (right).

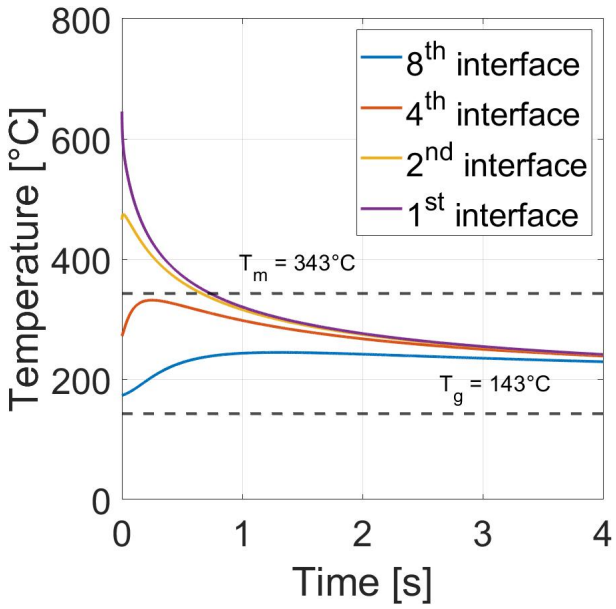

Figure 4.18: Time temperature evolution for different plies interfaces at the placement of the 21^{th} ply over a preheated mandrel at 150°C. The first interface corresponds to the interface between the incoming ply and the substrate.

The initial cooling rate of the first interface between the substrate and the incoming 21^{th} ply is approximately slightly higher than 320° C/s, as shown in Figure (4.18).

4.4.3 . Thermal history induced by the Laser Assisted Tape Placement

In the following, an example of a possible thermal history assessed by the analytical consolidation model presented in Section 4.3 induced during the LATP manufacturing process of a 7-layer composite laminate is shown. In particular, each layer is 0.15 mm thick and the composite material parameters used for the analytical calculations are (Grogan et al., 2015)

$$\rho = 1598 \text{ kg/m}^3, \quad C = 930 \text{ J/(kg K)}, \quad K = 0.4 \text{ W/(m K)},$$

while the boundary conditions parameters used are (Cogswell, 1992):

$$h_1 = 400 \text{ W/(m}^2 \text{ K)}, \quad h_2 = 10 \text{ W/(m}^2 \text{ K)}, \quad T_1 = 25^{\circ}\text{C}, \quad T_2 = 25^{\circ}\text{C}.$$

The initial temperature distribution is derived from the LATP heating phase, which is not modeled in the present work and not known from the literature for this specific case study. Consequently, in order to derive the initial condition to be used in the analytical calculations at

the placement of each layer of the structure, certain assumptions need to be made, based on the case studies previously addressed. The following assumptions were made about the initial condition:

- the whole manufacturing process is temperature-controlled (Stokes-Griffin and Compston, 2015b) which means that the temperature at the interface between the incoming ply and the substrate at the beginning of the consolidation process for each ply placement is fixed (for example at $450°$C, which is one of the interface temperature provided by CETIM);
- at the 2^{nd} ply placement, both layers will exceed the melting temperature of the thermoplastic matrix (as illustrated in Section 4.4.1);
- at the placement of the subsequent layers (3^{rd} ply, 4^{th} ply and so on up to the 7^{th} ply placement), at least three layers exceed the T_g of the polymeric matrix (as shown in Section 4.4.1 and in Section 4.4.1);
- at the placement of the subsequent layers (3^{rd} ply, 4^{th} ply and so on up to the 7^{th} ply placement), only the incoming ply and a part of the first layer of the substrate exceed the melting temperature of the polymeric matrix (as shown in Section 4.4.1 and in Section 4.4.1) (Grove, 1988; Stokes-Griffin et al., 2015; Kok, 2018)).

From an industrial application point of view, a temperature controlled LATP process means that the placement speed is kept constant, while the laser power is adjusted in order to keep constant the temperature at the nip-point during the heating phase (Stokes-Griffin and Compston, 2015b)).

The initial conditions assumed for the placement of the 2^{nd}, 3^{rd}, 4^{th} and 7^{th} ply are depicted in Figure (4.19). The initial conditions in Figure (4.19) are piece-wise exponential functions to be used in the analytical calculation of the temperature distribution induced by the LATP. It can be noticed that the initial conditions presented in Figure (4.19) meet the assumptions made.

The thermal responses of the inner surface of the substrate (the interface between the substrate and the mandrel) at the placement of the 2^{nd} ply, the 3^{rd} ply, the 4^{th} ply and the 7^{th} ply are depicted in Figure (4.20). Figure (4.20) is similar to Figure (4.7) left. In Section 4.4.2, the 1 mm thick, 8 layers laminate undergoes an initial cooling rate of roughly $250°$C/s (see the "2 plies" curve in Figure (4.7) left) and just 4 layers exceed the glass transition temperature ($T_g = 143°$C). In the present case, the 7 layers laminate (each layer is 0.15 mm thick) undergoes an initial

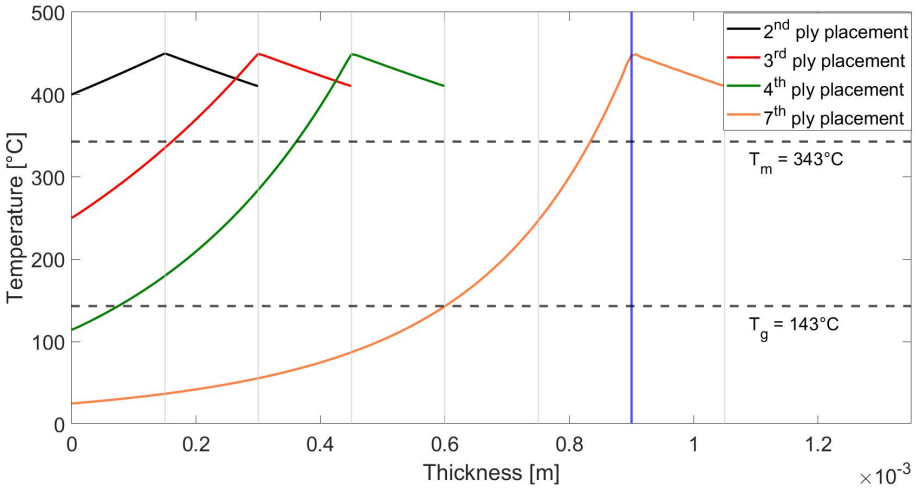

Figure 4.19: Initial temperature distribution assumed induced by the laser heat source at different plies placement. The vertical blue line indicates the interface between the 7^{th} incoming ply and the substrate. The functions depicted are piece-wise exponential functions.

cooling rate of roughly $200°$C/s (see the "2 plies" curve in Figure (4.20)) and the heat goes deeper in the laminate and 4 plies exceed the T_g (in this case each ply is thicker with respect to the ply thickness in Section 4.4.2), as shown in Figure (4.20). The initial conditions used (see Figure (4.19)) are quite different from the initial conditions used in Section 4.4.1 (see Figure (4.3)). Indeed, the temperature at the interface between substrate and the incoming ply are always fixed at $450°$C in the present case, while Grove (1988), for each ply deposition, uses different temperatures at the interface.

Assuming the first layer of the laminate was already welded on the mandrel, the initial conditions found in Figure (4.19) are applied sequentially to the analytical thermal model presented in Section 4.3 for each placed layer of the 7-layer laminate, updating the thickness at each iteration. The complete thermal history induced within the laminate by the LATP manufacturing process is depicted in Figure (4.21). At $Time = 0$ s, the LATP machine winds-up the second ply of the laminate (the curve "2 plies" in Figure (4.21)), at $Time = 4$ s the third ply placement occurs (the curve "3 plies" in Figure (4.21)) and so on for the other curves.

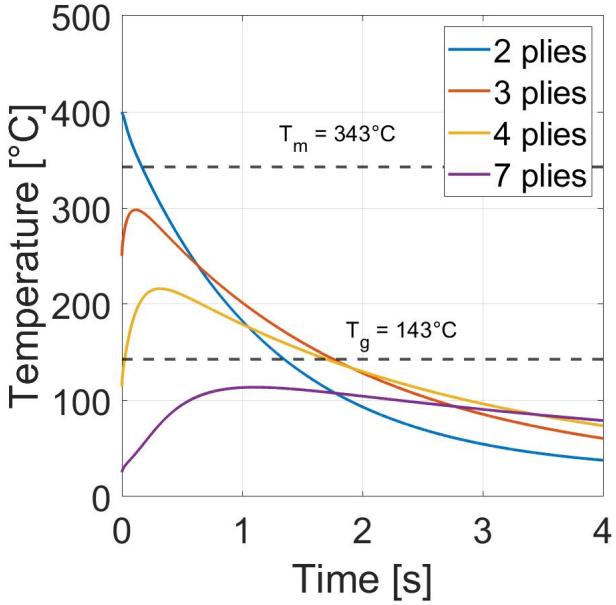

Figure 4.20: Superimposed thermal responses of the inner surface of the substrate at the placement of the 2^{nd} ply, the 3^{rd} ply, the 4^{th} ply and the 7^{th} ply.

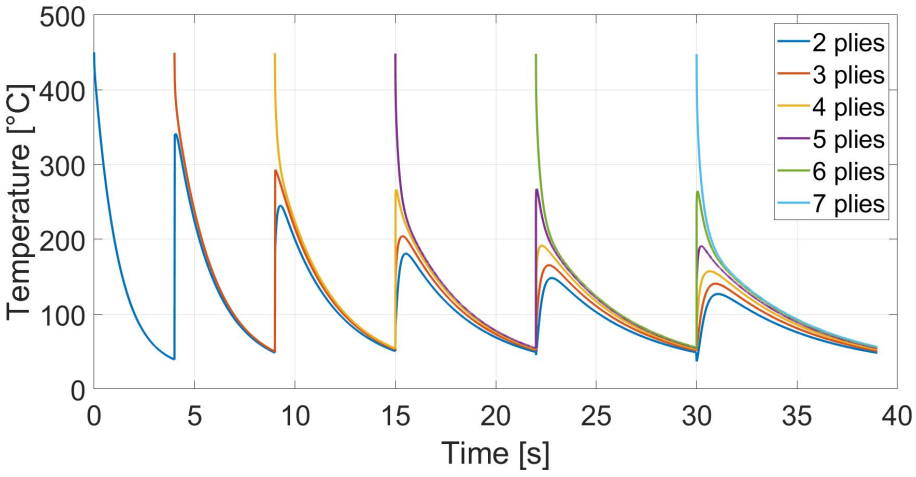

Figure 4.21: Thermal history, assessed by the analytical model, experienced by the interfaces between the substrate and the different incoming layers during the LATP manufacturing process.

4.5 . Conclusions

In the present Chapter, a one-dimensional transient heat transfer model was proposed in order to describe the consolidation phase of the laser assisted tape placement and its analytical solution was presented. The boundary conditions used involved the presence of the mandrel as a heat sink, especially for the first deposed plies, while the outer surface of the laminate is exposed to the convection with air. A crucial role is played by the initial condition, which is the temperature distribution induced by the heating phase of the LATP. Here, it was derived from other models describing the heating phase of the LATP (Grove, 1988; Kok, 2018; Sonmez and Hahn, 1997a).

Several scenarios were addressed, where different initial conditions were used in order to assess the time temperature evolution through the thickness of the laminate. In particular, in Section 4.4.1 the results presented by Grove (1988) were used in order to derive the initial condition to be used in the thermal model proposed here to assess analytically the temperature distribution induced in the laminate in Section 4.4.2. The same was made in Section 4.4.1 and in Section 4.4.1, where the results presented respectively by Kok (2018) and Sonmez and Hahn (1997a) were used to derive the initial conditions to be used in the analytical thermal model and the time temperature evolution were assessed respectively in Section 4.4.2 and in Section 4.4.2. The initial condition induced by the heating phase of the LATP manufacturing process using a preheated mandrel was derived in Section 4.4.1 from the results presented by Sonmez and Hahn (1997a) and used in the analytical thermal model in Section 4.4.2 to assess the time temperature evolution in the laminate.

The literature research carried out on different temperature distributions induced by the LATP heating phase and considerations made enabled us to derive in Section 4.4.3 the initial conditions to be used in the analytical model to develop a thermal history caused by a LATP manufacturing process of a 8 plies composite laminate.

The present analytical model takes into account the main thermal aspects involved in the LATP and it turns out to be a great advantage in terms of computational time. It will be used in Chapter 5, where thermo-mechanical simulations of the whole LATP manufacturing process are performed.

5 - Residual stresses and strains induced in tubes manufactured by LATP

5.1 . Introduction

In Chapter 3, a temperature-dependent visco-elastic constitutive model suited for fibers reinforced polymer matrix composite material was presented. This constitutive model was introduced in order to include the relaxation of some stress terms when the temperature is higher then the glass transition temperature of the polymeric matrix. In Chapter 4, a transient heat transfer model for the laser assisted tape placement was proposed. The through-thickness one-dimensional thermal model was solved analytically in order to describe the temperature distribution induced within the composite structure by the consolidation phase of the LATP manufacturing process.

In the present Chapter, thermo-mechanical simulations were performed on tubes by means of the commercial finite element software Abaqus, with the goal to assess the residual stresses and strains induced by the LATP. The temperature-dependent viscoelastic constitutive model and the analytical thermal model were implemented in user-defined subroutines, a UMAT and a UTEMP respectively, in order to perform structural simulations on Abaqus.

LATP manufacturing processes with two different mandrel temperatures are simulated in Section 5.2 on different 6-layer tubes with different stacking sequences. For all the tubes, each layer is 0.16 mm thick, and the angle is assessed with respect the axial direction of the tube. The stacking sequences are: $[90°]_6$, $[\pm 85°]_3$, $[\pm 55°]_3$, $[0°]_6$. A particular strategy, that follows that of the additive manufacturing process (Michaleris, 2014), is used in Section 5.2.1 to simulate the LATP manufacturing processes. Different simulations were performed, assuming either a cold mandrel ($T^{mand}_{cold} = 20°$C) or a hot mandrel ($T^{mand}_{hot} = 180°$C). The thermal histories induced in the structure by the manufacturing processes are derived from the considerations made in Chapter 4 and presented in Section 5.2.2.

A cut along the axial direction of the tubes is simulated in Section 5.3 in order to break the material continuity, and therefore to release residual stresses. The geometrical distortions of the tubes after the axial cut are presented in Section 5.3. Among all simulated tubes, the only tube to open is the $[0°]_6$ tube manufactured with a cold mandrel, where the strong temperature gradients induce the opening. After the

axial cut, the shear stresses induced in the $[\pm 85°]_3$ and $[\pm 55°]_3$ tubes by the manufacturing processes cause the tubes to twist.

A comparison between numerical and experimental deformations is made in Section 5.3.1 for $[\pm 85°]_3$ and $[\pm 55°]_3$ tubes manufactured with both cold and hot mandrel. The tools developed in the present work are capable to predict the closing and twisting of tubes in qualitative agreement with the experimental results, with the exception for the $[\pm 55°]_3$ tube manufactured with cold mandrel. The thermal gradients implemented for the cold mandrel thermal history may not be severe enough to cause the experimentally observed change from closed (with hot mandrel) to open (with cold mandrel) tube.

Finally, in Section 5.4 conclusions and perspectives are discussed.

5.2 . Tubes simulations: residual stresses results

In the following sections, the cold mandrel and hot mandrel LATP manufacturing processes are simulated on tubes. The thermo-mechanical simulations are performed on 6-layer tubes with circular section and the following geometrical parameters:

$$R_{in} = 20 \text{ mm}, \quad L = 60 \text{ mm}, \quad h_{tot} = 0.96 \text{ mm},$$

where R_{in} is the inner radius, L is the length of the tube while h_{tot} is the thickness.

The instantaneous elastic parameters used are the following (Grogan et al., 2015):

$$E_L = 134 \text{ GPa}, \quad E_T = 10.3 \text{ GPa}, \quad \mu_L = 6 \text{ GPa}, \quad \nu_{LT} = 0.32, \quad \nu_{TT} = 0.4,$$

while the following viscoelastic parameters are used to simulate a nearly complete relaxation:

$$\mu_L^{lt} = 0.001\mu_L, \quad \mu_T^{lt} = 0.001\mu_T, \quad \tau_{fs} = 10 \text{ s}, \quad \tau_d = 10 \text{ s}.$$

The coefficients of thermal expansion of the composite material are (Grogan et al., 2015):

$$\alpha_1 = 0.2(10^{-6})/°\text{C}, \quad \alpha_2 = 28.8(10^{-6})/°\text{C},$$

while the parameters used for the WLF law are (Chapman et al. (1990)):

$$T_{ref} = 143°\text{C}, \quad C_1 = 52, \quad C_2 = 243°\text{C}.$$

The tubes simulated have different stacking sequences: $[90°]_6$, $[\pm 85°]_3$, $[\pm 55°]_3$ and $[0°]_6$. The temperature-dependent viscoelastic constitutive model for the composite material and the analytical thermal model for the LATP manufacturing process were implemented in users-subroutines called respectively UMAT and UTEMP.

5.2.1 . LATP manufacturing process modeling

The LATP manufacturing process was simulated as follows:

- at the beginning of the simulations, all of the plies that will be placed are already present in the model (in order to avoid remeshing) as shown in Figure (5.1);
- a detailed simulation of the trajectory followed by the machine in the tape deposition over the substrate would be too time consuming, for this reason each layer is assumed to be deposed in one go, leading to a thermal gradient in the layer thickness direction only (the details of this assumption were discussed in Chapter 4);
- the first ply of the composite structure is assumed to be already welded on the mandrel, therefore the 6-layer tube simulated is obtained through five placement processes;
- the analytical thermal model proposed in Chapter 4 and implemented in the UTEMP is applied sequentially for each ply deposition to the ply being placed and the substrate, and at each iteration only the structure thickness is updated;
- layers which are not involved in the placement process are artificially kept (through the developed UTEMP) at the maximum temperature reached during the deposition process ($T = 420°$C) and their material parameters are set to zero (through the developed UMAT) in order prevent them from mechanically contributing to the stress buildup (this strategy is similar to the quiet elements strategy in the simulation of additive manufacturing, see for instance (Michaleris, 2014));
- the presence of the mandrel is assumed imposing a null displacement ($U_1 = U_2 = U_3 = 0$) at the inner surface of the tube.

In the last layer placement simulation step, the structure reaches the cold mandrel temperature or the hot mandrel temperature. Two further simulations steps are carried out. In the first additional step, the mechanical boundary conditions imposed by the mandrel are replaced with boundary conditions where only the rigid motion of the tube is blocked. In the second additional step, the thermal boundary conditions imposed by the convection with the mandrel and the ambient during the placement process are removed. In the LATP simulation with the hot mandrel, the analytical thermal model implemented

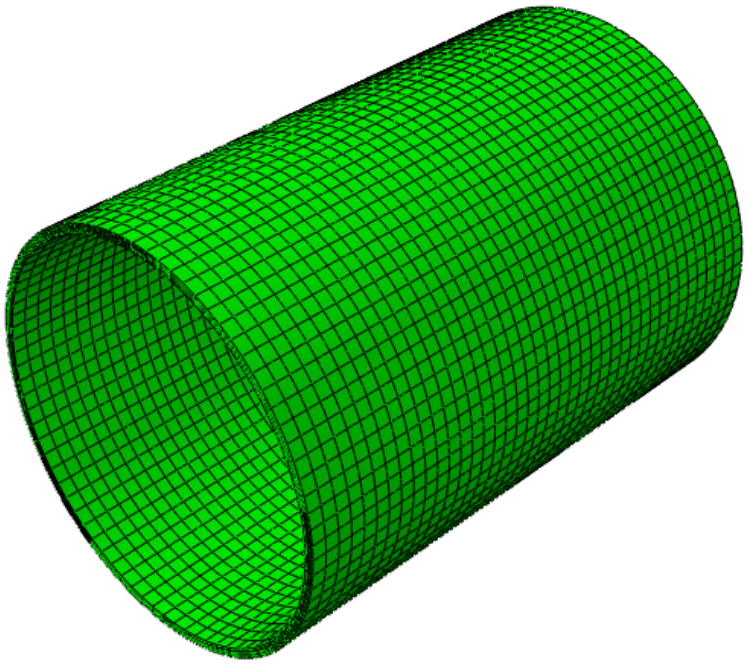

Figure 5.1: Geometry and mesh of the simulated tube.

in the UTEMP is replaced by a linear temperature function to simulate the uniform and slow cooling process to room temperature. On the other hand, the structure reaches the ambient temperature in the manufacturing process simulation with the cold mandrel at the end of the placement process.

The simulated tube (see Figure(5.1)) is meshed using the classical composite modelling technique presented in Chapter 2, that is one solid element per ply in the thickness direction. In particular, we used the 3D stress element to include the significant effect of the geometry and anisotropy of the tubes, and the quadratic interpolation function in order to have a better discretization in the thickness direction. The total number of elements is 19680.

5.2.2 . Thermal histories induced by the LATP manufacturing processes with hot and cold mandrel

The material parameters used in the analytical calculations for the thermal model are (Grogan et al., 2015)

$$\rho = 1598 \text{ kg/m}^3, \quad C = 930 \text{ J/(kg K)}, \quad K = 0.4 \text{ W/(m K)},$$

while the boundary conditions parameters used are (Cogswell, 1992):

$$h_1 = 500 \text{ W/(m}^2 \text{ K)}, \quad h_2 = 10 \text{ W/(m}^2 \text{ K)}, \quad T_1 = 20^\circ\text{C}, \quad T_2 = 20^\circ\text{C}.$$

The thermal history induced by the cold mandrel ($T^{mand}_{cold} = 20°$C) implemented in the UTEMP is derived based on the observations made in Chapter 4. In this case, the temperature at the interface between the layer being placed and the substrate is $420°$C. This is an average temperature, provided by CETIM, obtained from thermal camera data. The thermal histories induced by the LATP manufacturing process with cold mandrel for the second interface and the sixth interface are depicted in Figure (5.2) top. It can be noticed that at the end of the placement process, the structure reaches the temperature T^{mand}_{cold}.

The thermal history induced by the hot mandrel ($T^{mand}_{hot} = 180°$C) implemented in the UTEMP is derived based on the observations made in Chapter 4, and also in this case the temperature at the interface between the layer being placed and the substrate is $420°$C. At the end of the placement process, the temperature of the entire composite structure exceeds the glass transition temperature of the polymeric matrix ($T_g = 143°$C) and it reaches the temperature T^{mand}_{hot} (see Figure (5.2) bottom). Therefore, a uniform cooling process to room temperature ($T^{room} = 20°$C) was implemented in the UTEMP through a linear temperature function to simulate an annealing process. The mechanical boundary conditions imposed by the mandrel during the annealing process are replaced with boundary conditions where only the rigid motion is inhibited. The thermal histories induced by the LATP manufacturing process with hot mandrel for the second interface and the sixth interface are depicted in Figure (5.2) bottom.

In Figure (5.3) left and right, the through-thickness temperature induced by the manufacturing process with cold and hot mandrel are depicted at a particular time step (the first time step of the third ply placement) of the simulations. In Figure (5.3) left and right, the difference in terms of temperature gradient between the two manufacturing processes can be seen.

5.2.3 . Numerical simulations on a $[90°]_6$ cylindrical tube

Three thermo-mechanical simulations are performed on a $[90°]_6$ tube (that is, with fibers aligned along the circumferential direction):

1. in the first, the thermal history depicted in Figure (5.2) top, for a cold mandrel ($T^{mand} = 20°$C), is simulated, and the viscoelastic material model is considered;

2. in the second, the thermal history depicted in Figure (5.2)) bottom, for a hot mandrel ($T^{mand} = 180°$C), is simulated, and the viscoelastic material model is considered;

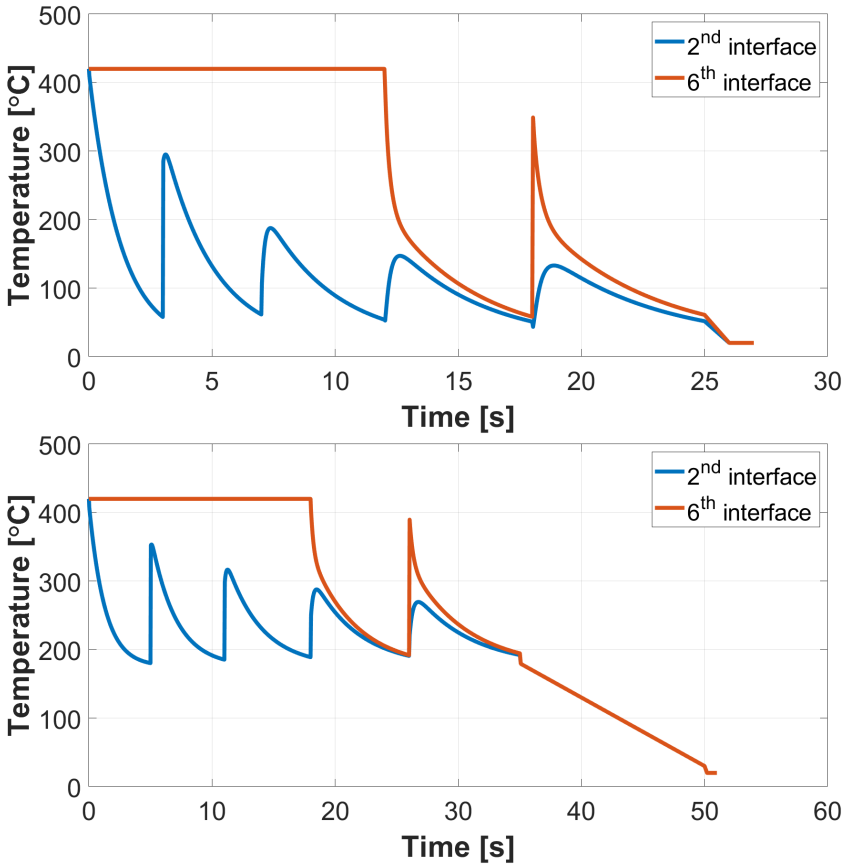

Figure 5.2: Temperature history experienced by the second and the sixth interfaces of the structure manufactured by the LATP using a cold mandrel ($T^{mand} = 20°$C) (top) and a hot mandrel ($T^{mand} = 180°$C) (bottom). The interface between the mandrel and the first ply of the structure corresponds to the first interface. In the simulation using a hot mandrel, after the structure reaches the mandrel temperature, the mandrel is removed and a uniform cooling process to the room temperature ($T = 20°$C) is imposed.

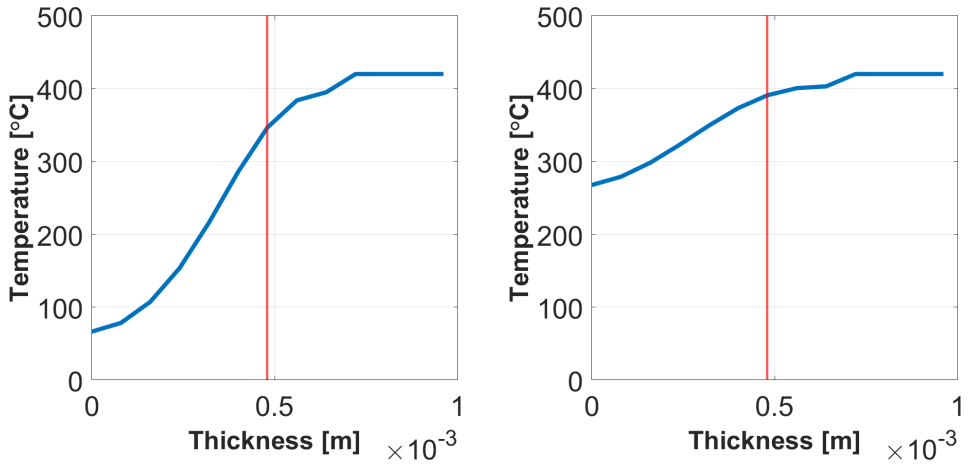

Figure 5.3: Through thickness temperature induced by the manufacturing process using a cold mandrel ($T^{mand} = 20°$C) (left) and a hot mandrel ($T^{mand} = 180°$C) (right) at the third ply placement. The red vertical line is the interface between the substrate and the incoming ply.

3. in the third, a fully elastic tube is subjected to a uniform cooling process ($\Delta T = -400°$C).

The results are shown in Figure (5.4a) for the circumferential stress, in Figure (5.4b) for the axial stress and in Figure (5.4c) radial stresses.

The circumferential direction of the $[90°]_6$ tube is dominated by the fibers behavior, which is elastic (see Chapter 3) and therefore less affected by the temperature gradients induced by the manufacturing process. One could expect that the circumferential stress results obtained with the LATP thermal histories would be similar to the results obtained for the elastic simulations with the tube subjected to a uniform cooling, but this is not the case, as it shown in Figure (5.4a). The differences observed are interpreted in the following.

In the simulations with cold and hot mandrel, and the viscoelastic model, the mandrel presence as a boundary condition inhibits the strain ε_{zz} in the tube axial direction, which corresponds to ε_{22} in the material basis. This situation is similar to the material point simulations discussed in Chapter 3 (see Section 3.6.1): the inhibition of ε_{22} results in a more significant development of the radial strain ε_{rr}, here ε_{33}, both in the viscous regime ($T > T^{ref}$) and in the elastic regime ($T < T^{ref}$).

Remembering now that the tube geometry (Chapter 2) couples the out of plane kinematics with the in plane kinematics, the resultant circumferential stress assessed with both hot and cold mandrel turns out to be higher with respect to the fully elastic simulation on the same

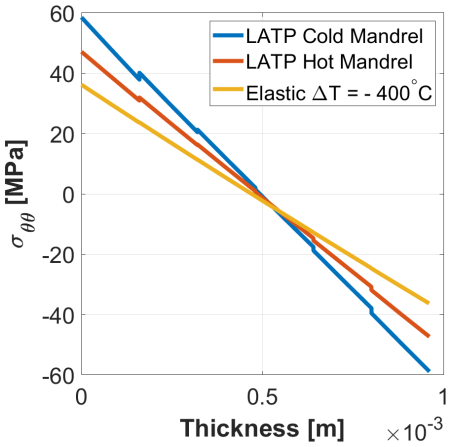

(a) Circumferential stress distribution.

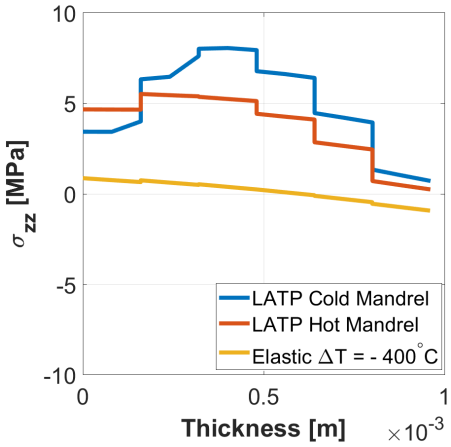

(b) Axial stress distribution.

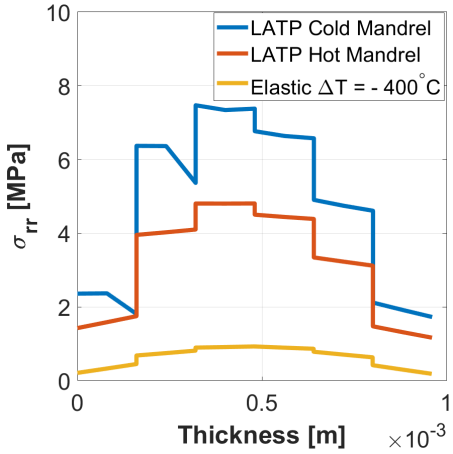

(c) Radial stress distribution.

Figure 5.4: Residual stresses distributions along the thickness of a tube $[90°]_6$ simulated with three different thermal histories and material models: thermal histories induced by the LATP using a cold mandrel ($T^{mand}_{cold} = 20°$C) and a hot mandrel ($T^{mand}_{hot} = 180°$C) and viscoelastic model, and an elastic simulation on the tube subjected to a uniform cooling process.

tube subjected to a uniform cooling process and using an elastic material. In other words, the difference in the circumferential stress $\sigma_{\theta\theta}$ results in Figure (5.4a) between the manufacturing process simulations and the fully elastic simulation is due to the combined effects of:

1. the transversely isotropic visco-elastic constitutive behavior;
2. the mandrel boundary condition;
3. the geometry of the tube and the anisotropy of the composite ply.

The differences between the simulations with hot and cold mandrel are further analyzed in the following.

The circumferential stress obtained in the simulation with a cold mandrel is higher than the one obtained in the simulation with a hot mandrel. In the hot mandrel case, the mandrel is removed while the structure is still in the viscous domain ($T_{hot}^{mand} = 180°\text{C} > T^{ref}$), therefore the radial deformation adapts to the axial deformation lock induced by the mandrel over a smaller temperature range than for the cold mandrel (from $T = 420°\text{C}$ to $T_{hot}^{mand} = 180°\text{C}$). After the mandrel removal, both the axial and the radial strains adapt so as to have a compatible transverse isotropic hydrostatic strain in the viscous domain. On the other hand, in the cold mandrel simulation the mandrel is removed at $T_{cold}^{mand} = 20°\text{C}$, therefore the radial strain adapts to the axial strain lock induced by the mandrel over a larger temperature range (from $T = 420°\text{C}$ to $T^{ref} = 143°\text{C}$), leading to a higher radial strain and consequently to a higher circumferential stress (see Figure (5.4a)).

The radial and the axial directions of the $[90°]_6$ tube, which belong to the transverse isotropic plane, are dominated by the matrix behavior, which is affected by the thermal gradients of the manufacturing process through the strains accommodation in the viscous domain. Therefore, discrepancies between the axial and radial stresses distributions (see Figure (5.4c) and Figure (5.4b)) for the different simulations are expected.

5.2.4 . Numerical simulations on a $[\pm 85°]_3$ tube

Here, thermo-mechanical simulations were performed on a $[\pm 85°]_3$ tube using the LATP temperature histories with a cold and a hot mandrel (illustrated in Figure (5.2) top and in Figure (5.2) bottom respectively). This particular case is quite similar to the example presented previously in Section (5.2.3), because the fibers are oriented almost along the circumferential direction of the tube. Therefore, the circumferential direction is dominated by the fibers elastic behavior, while the

axial and the radial directions are dominated by the viscoelastic behavior of the matrix. The same considerations made in Section (5.2.3) apply also in this case. In Figure (5.5a), in Figure (5.5b) and in Figure (5.5c) are depicted the circumferential, the axial and the radial stresses induced by the manufacturing process with cold and hot mandrel, respectively.

The only difference with respect to the previous case is the presence, in the tube $[\pm 85^\circ]_3$, of a shear stress distribution (depicted in Figure (5.5d)). The shear stress was identically zero in the $[90^\circ]_6$ tube, and thus no curve was given.

5.2.5 . Numerical simulations on a $[0^\circ]_6$ tube

In this Section, thermo-mechanical simulations on a $[0^\circ]_6$ tube (that is, with fibers aligned along the axial direction) using the thermal history induced by the manufacturing process LATP with both cold and hot mandrel were performed, in order to see the effects of the temperature gradients in the circumferential direction, which is dominated by the viscoelastic behavior of the matrix. In Figure (5.6), the residual stresses induced in the tube are shown.

In this case, zero residual stresses would be obtained by performing a fully elastic simulation with a uniform cooling process, because the combined effect of the geometry and the anisotropy of the composite material seen in Chapter 2 is absent. Indeed, the radial and the circumferential directions are both dominated by the matrix behavior (thermal strains $\alpha_2 \Delta T$), therefore no incompatibility is introduced by the geometry which couples the two directions. In this scenario, therefore, the only source of residual stresses within the tube are the strong temperature gradients induced by the manufacturing process.

The thermal gradients induced by the hot mandrel are not relevant enough to introduce the incompatibility and build residual stress in the circumferential direction (as depicted in Figure (5.6a)). On the contrary, the thermal gradients induced by the cold mandrel generate a residual stress distribution in the circumferential direction (shown in Figure (5.6a)), similarly to the skin-core effect on thermoformed plates discussed in Chapter 3.

It is interesting to notice that the circumferential stress distribution depicted in Figure (5.6a) for the cold mandrel, leads to compression of the inner part and traction of the outer part of the $[0^\circ]_6$ tube. This results in an overall bending moment whose sign is opposite to the one predicted for the previous cases. The effect of the thermal gradient for tubes with a matrix-dominated circumferential direction is therefore opposite to the one brought about by the coupled geometry and anisotropy.

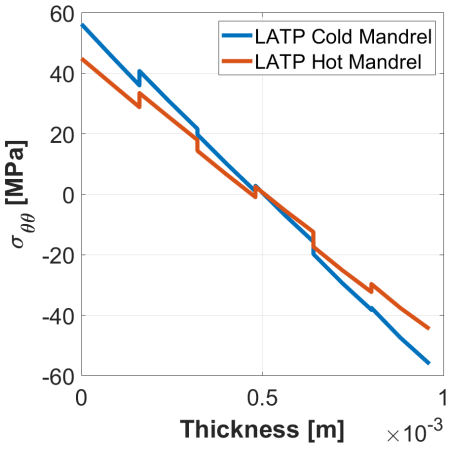

(a) Circumferential stress distribution.

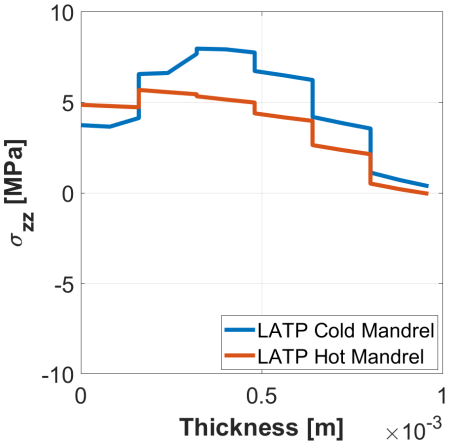

(b) Axial stress distribution.

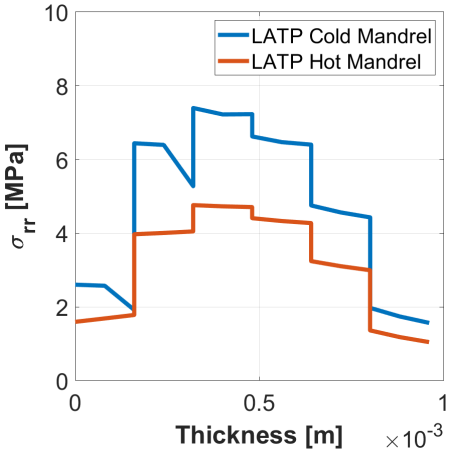

(c) Radial stress distribution.

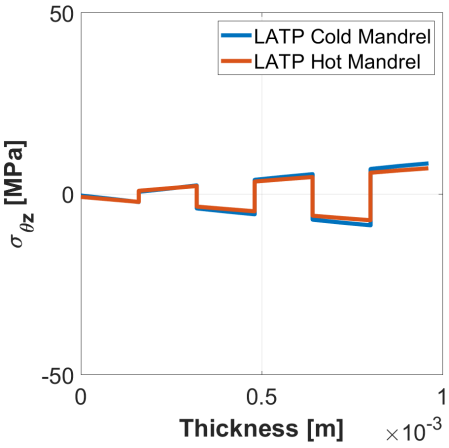

(d) Shear stress distribution.

Figure 5.5: Residual stresses distributions along the thickness of a tube $[\pm 85°]_6$ simulated with two different thermal histories: thermal histories induced by the LATP using a cold mandrel ($T^{mand}_{cold} = 20°$C) and a hot mandrel ($T^{mand}_{hot} = 180°$C) and viscoelastic model.

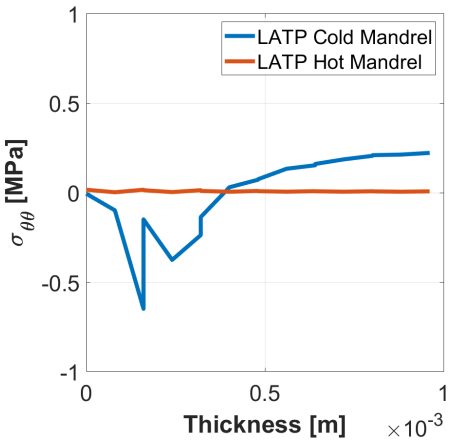

(a) Circumferential stress distribution.

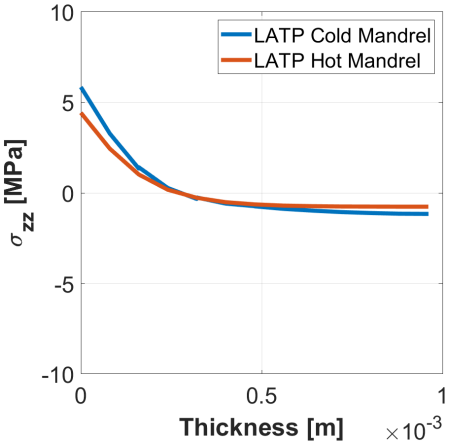

(b) Axial stress distribution.

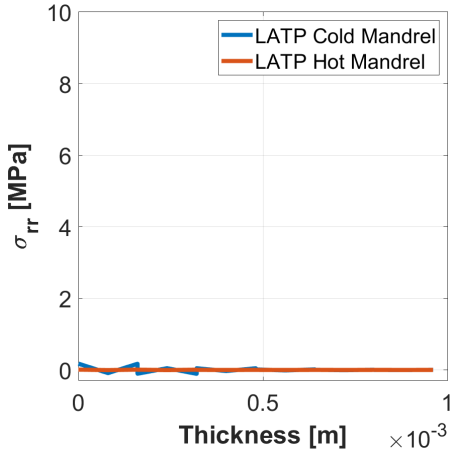

(c) Radial stress distribution.

Figure 5.6: Residual stresses distributions along the thickness of a tube $[0°]_6$ simulated with two different thermal histories: thermal histories induced by the LATP using a cold mandrel ($T_{cold}^{mand} = 20°$C) and a hot mandrel ($T_{hot}^{mand} = 180°$C) and viscoelastic model.

The complex shape of the circumferential stress distribution for the first two layers in Figure (5.6a), indicates that a finer through-thickness mesh should be used there to capture the effect of the high thermal gradients during deposition of these plies.

The axial direction is dominated by the elastic behavior of the fibers, therefore unaffected by the thermal gradients. The non-linear stress distribution in the axial direction depicted in Figure (5.6b) is the consequence of the combined effects of:

1. the incompatibility introduced, in the transversely isotropic plane, by the thermal history of the cold mandrel;

2. the transversely isotropic visco-elastic constitutive behavior;

3. the mandrel boundary condition.

The manufacturing processes with both cold and hot mandrel $[0°]_6$ tube do not build-up residual stresses in the radial direction, as depicted in Figure (5.6c).

5.2.6 . Numerical simulations on a $[\pm 55°]_3$ cylindrical tube

In this Section, the same thermo-mechanical simulations performed in Section 5.2.3 on a $[90°]_6$ tube were performed on $[\pm 55°]_3$ tube. A fourth simulation was performed on a fully elastic $[\pm 55°]_3$ tube subjected to a uniform cooling process wiht $\Delta T = -123°$C. The induced residual stress are depicted in Figure (5.7). The circumferential, the axial, the radial and the shear residual stresses distributions are depicted in Figure (5.7a), (5.7b), (5.7c) and in Figure (5.7d) respectively.

In the present case, the same combined effects discussed in Ssection 5.2.3 for the $[90°]_6$ tube apply. In addition, the stacking sequence needs to be considered here. Indeed, the strain in the transverse direction (ε_{22}) of one ply is partially inhibited by the strain in the fibers' direction (ε_{11}) of the adjacent ply. Moreover, the boundary condition of the mandrel partially inhibits the strain ε_{22} of the innermost layer of $[\pm 55°]_3$ tube. Consequently, different visco-elastic strains adaptation and partial stress relaxation are obtained in the viscous domain. For these reasons, the circumferential and axial stresses assessed in the cold and hot mandrels simulations are lower compared to the stresses obtained in the elastic simulation with $\Delta T = -400°$C, as shown in Figure (5.7a) and in Figure (5.7b).

If complete stresses relaxation had been possible, the results for circumferential and axial stresses would have been similar to those obtained in the elastic simulations with $\Delta T = -123°$C.

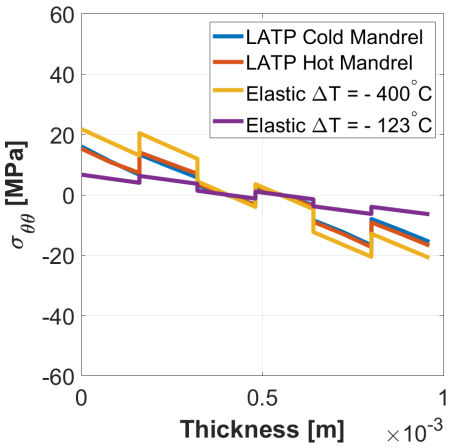

(a) Circumferential stress distribution.

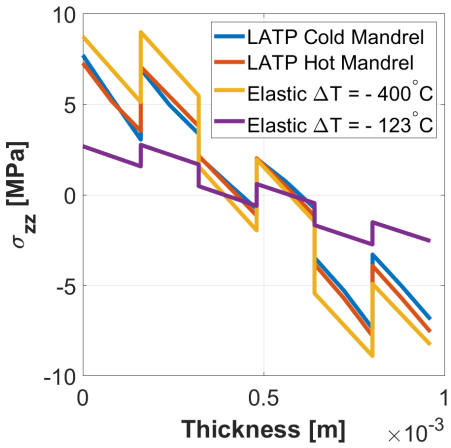

(b) Axial stress distribution.

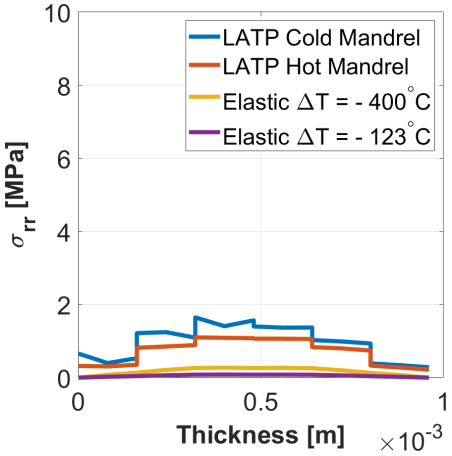

(c) Radial stress distribution.

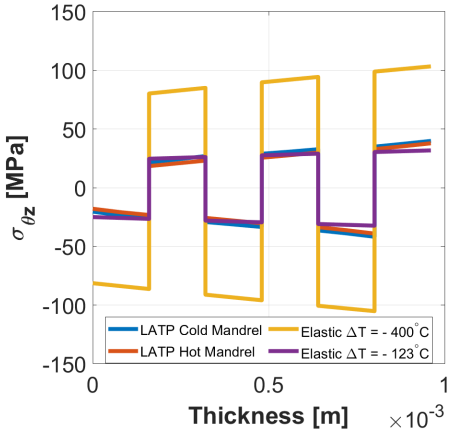

(d) Shear stress distribution.

Figure 5.7: Residual stresses distributions along the thickness of a tube $[\pm 55°]_3$ simulated with four different thermal histories and material models: thermal histories induced by the LATP using a cold mandrel ($T^{mand}_{cold} = 20°$C) and a hot mandrel ($T^{mand}_{hot} = 180°$C) and viscoelastic model, a fully elastic simulation on the tube subjected to a uniform cooling process ($\Delta T = -400°$C) and a fully elastic simulation on the tube subjected to a uniform cooling process ($\Delta T = -123°$C).

The circumferential and axial stresses distributions depicted in Figure (5.7a) and in Figure (5.7b) are almost the same for the cold and hot mandrel simulations. In this scenario, the main factors that can change the tube's responses are the thermal history and the viscoelastic constitutive behavior. Consequently, implementing a more severe thermal history for the cold mandrel simulation could probably result in different circumferential stresses in the tube than those shown in Figure (5.7a) and (5.7b). More significant thermal gradients could be expected if, for instance, the fibers distribution in the cross-section of the tape is not uniform. This would result in a higher concentration of polymeric matrix on the tape's outer surfaces, leading to higher thermally insulating tape. Similarly, a constitutive model enabling viscoelastic relaxation also of the hydrostatic stress of the transverse isotropic plane, would lead to different stresses in the tube. Indeed, the shear modulus of the matrix phase does affect the hydrostatic response of the transverse isotropic plane of the composite, as it was pointed out in Chapter 3 with the analytical homogenization made in Section 3.3, while this effect is neglected in the present model.

The strains adaptation in the viscous domain, caused by the coupling between the visco-elastic behavior and the boundary condition of the mandrel, generates higher radial residual stresses, as depicted in Figure (5.7c) right, with respect to the elastic simulations.

In Figure (5.7d), the shear stresses $\sigma_{\theta z}$ are shown. In the material basis, the shear stress σ_{12} is the dominant contribution on the shear stress $\sigma_{\theta z}$ which, in the viscous domain (for $T > T^{ref}$), experiences a complete relaxation. Consequently, the thermal path followed by the simulation does not affect the shear stress $\sigma_{\theta z}$ as shown in Figure (5.7d). Indeed, the shear stress induced by the LATP manufacturing process (with both cold and hot mandrel) is the same as the shear stress obtained in the fully elastic simulation with a constant temperature difference $\Delta T = T^{end} - T^{ref} = -123°\text{C}$.

5.3 . Geometrical distortions of the cylindrical tubes after the axial cut

The circumferential stresses distributions induced by the manufacturing process, obtained in the previous simulations (in Figure (5.4a), (5.5a), (5.6a) and (5.7a)), generate bending moments, which represent constraints reactions to the material continuity in the circumferential direction of the tube (see Chapter 2). In Table (5.1), the bending moments calculated for the tubes simulated before are reported.

In Table (5.1), it can be noticed that the bending moments asso-

Table 5.1: Numerical bending moments for the $[90°]_6$, $[\pm 85°]_3$, $[\pm 55°]_3$ and $[0°]_6$ tubes manufactured with hot and cold mandrel.

Tube	Manufacturing process	Bending moment [N m/m]
$[90°]_6$	Hot mandrel	-7.3581
$[90°]_6$	Cold mandrel	-9.1358
$[\pm 85°]_3$	Hot mandrel	-7.1505
$[\pm 85°]_3$	Cold mandrel	-8.8847
$[\pm 55°]_3$	Hot mandrel	-2.5929
$[\pm 55°]_3$	Cold mandrel	-2.4660
$[0°]_6$	Hot mandrel	-2.6882×10^{-4}
$[0°]_6$	Cold mandrel	4.5840×10^{-2}

ciated to the circumferential stresses distributions presented before are always negative (as shown also in Chapter 2), except for the last tube $[0°]_6$ manufactured using a cold mandrel, which shows a positive bending moment. In the $[0°]_6$ tube, the effect of the geometry and the transverse isotropy is absent (both radial and circumferential behavior of the tube are dominated by the matrix behavior) and residual stresses are induced only by the severe temperature gradients of the thermal history induced by the manufacturing process with cold mandrel. On the other hand, the tube $[0°]_6$ manufactured using a hot mandrel presents an almost null bending moment, because the temperature gradients induced are not strong enough to generate residual stresses in the circumferential direction.

The material continuity in the circumferential direction of the tube can be interrupted by cutting the tube along the axial direction. By releasing the circumferential constraint of the cylindrical tube, the tubes deform due to the residual stresses induced during the manufacturing process. In particular, tubes with a negative bending moment and a shear stress distributions, after the axial cut, close on themselves and twist. On the other hand, the positive bending moment associated to the circumferential stress distribution induced in the tube $[0°]_6$ manufactured using a cold mandrel, tends to open the tube.

The simulation with the axial cut process was performed on the tubes simply by removing the mesh elements of the cut portion of the tube after the placement process and the mandrel removal. The width of the axial cut is $d_i = 3.4$ mm. Table (5.2) contains the geometrical distortions predicted numerically for each simulated tube. Particularly, the circumferential distance is the final width of the cut d_e (see Figure (2.7)), the circumferential relative displacement is the difference between the initial distance d_i and the final distance d_e ($d_e - d_i$ in Fig-

Table 5.2: Numerical results for the $[90°]_6$, $[\pm 85°]_3$, $[\pm 55°]_3$ and $[0°]_6$ tubes manufactured with hot and cold mandrel: circumferential distance, circumferential relative displacement and twist offset.

Tube	Manufacturing process	Circ. dist. [mm]	Circ. rel. disp. [mm]	Twist offset [mm]
$[90°]_6$	Hot mandrel	1.547	-1.854	–
$[90°]_6$	Cold mandrel	1.108	-2.292	–
$[\pm 85°]_3$	Hot mandrel	1.524	-1.877	0.734
$[\pm 85°]_3$	Cold mandrel	1.076	-2.324	0.770
$[\pm 55°]_3$	Hot mandrel	2.151	-1.249	1.289
$[\pm 55°]_3$	Cold mandrel	2.238	-1.162	1.276
$[0°]_6$	Hot mandrel	3.381	-0.019	–
$[0°]_6$	Cold mandrel	3.548	0.148	–

ure (2.7) in Chapter 2) while the twist offset is the distance between the free edges in the axial direction (see Figure (2.8) in Chapter 2).

The cut tube before deformation is depicted in Figure (5.8a), and the deformed tubes manufactured with cold mandrel after axial cutting is shown in Figure (5.8b) for the $[90°]_6$ tube, in Figure (5.8c) for the $[\pm 85°]_3$ tube, in Figure (5.8d) for the $[\pm 55°]_3$ tube and in Figure (5.8e) for the $[0°]_6$ tube.

Unidirectional tubes, like the $[90°]_6$ tube and the $[0°]_6$ tube, have no shear stresses, so the twist offset is not present (see Figure (5.8b) and Figure (5.8e)). The bending moment induced in the cold mandrel $[90°]_6$ tube is larger (in modulus) with respect to the hot mandrel tube (see Table (5.1)), therefore the cold mandrel $[90°]_6$ tube closes more (see Table (5.2)). The same thing happens for the $[\pm 85°]_3$ cold mandrel tube (Figure (5.8c)) which closes more compared to the hot mandrel one. The circumferential direction of the $[90°]_6$ tube is dominated completely by the elastic fibers behavior, therefore in this direction its stiffness is bigger with respect to the $[\pm 85°]_3$ tube. Indeed, even if the bending moments induced in the $[90°]_6$ tube are bigger with respect to the bending moments induced in the $[\pm 85°]_3$, the circumferential relative displacement is lower, as detailed in Table (5.2). The manufacturing process induce a shear stress distribution in the $[\pm 85°]_3$ tube which causes, after the axial cut, a twist offset (Figure (5.8c)).

The bending moments induced in the $[\pm 55°]_3$ tube by the manufacturing processes with cold and hot mandrel are both negative (see Table (5.1)) resulting in the closure of both tubes (see Figure (5.8d)).

The circumferential relative displacements after the axial cut in the $[90°]_6$ and $[\pm 85°]_3$ tubes simulated with the cold mandrel are bigger in

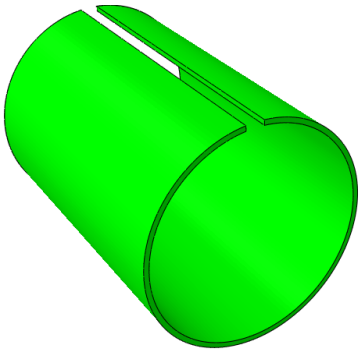

(a) Cut tube before deformation.

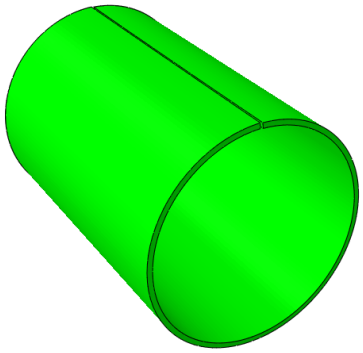

(b) Distortions of $[\pm 90°]_6$ tube manufactured with a cold mandrel using a deformation scale factor of 1.3.

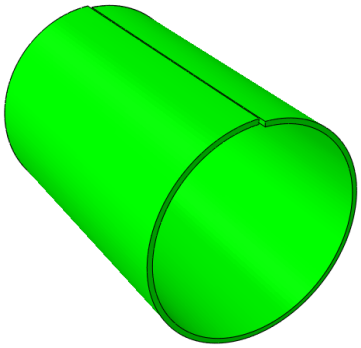

(c) Distortions of $[\pm 85°]_3$ tube manufactured with a cold mandrel using a deformation scale factor of 1.3.

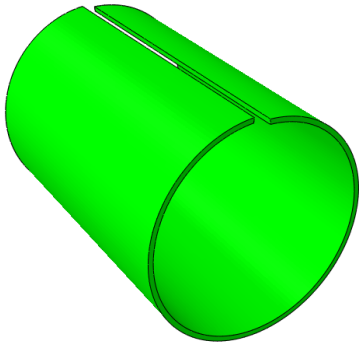

(d) Distortions of the $[\pm 55°]_3$ tube manufactured with a cold mandrel using a deformation scale factor of 1.3.

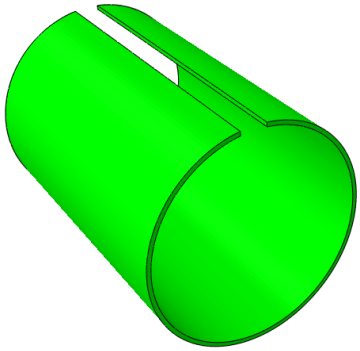

(e) Distortions of the $[0°]_6$ tube manufactured with a cold mandrel using a deformation scale factor of 10.

Figure 5.8: Geometric distortions after axial cutting of cold mandrel manufactured tubes.

modulus with respect to the circumferential relative displacement induced in the same tubes by the LATP manufacturing process with the hot mandrel (see Table (5.2)). Conversely, the circumferential relative displacement induced in the $[\pm 55^\circ]_3$ tube simulated with cold mandrel is slightly lower with respect to the circumferential relative displacement induced in the same tube by the LATP manufacturing process with the hot mandrel (see Table (5.2)). This highlights the effects of the temperature gradients in the tube's circumferential direction, which has an opposite trend to that shown by the geometry and anisotropy.

The temperature gradients effects in the transverse direction of a unidirectional composite plate was shown in Chapter 3 (Figure (3.15)), where the outer surfaces of the plate, which cool down faster, are put under compression by the core of the plate, which cools down more slowly and is subjected to traction. The sequential layer deposition (Barnes and Byerly, 1994) which characterizes the Laser Assisted Tape Placement manufacturing process, works similarly, because the incoming hot layer cools down over the substrate, which is already cold (as the substrate is colder than the incoming ply). For this reason, the incoming ply is subjected to traction while the substrate in compression. The direct consequence of the strong thermal gradients of the cold mandrel manufacturing process is that the $[\pm 55^\circ]_3$ tube develops lower bending moment than the $[\pm 55^\circ]_3$ tube manufactured with the hot mandrel (as detailed in Table (5.1)). In the $[\pm 55^\circ]_3$ tube, this effect is barely visible because the thermal gradients must overcome the combined effect of geometry and anisotropy, as well as the effect of the viscoelastic matrix with the boundary conditions imposed by the mandrel. Therefore, one of the perspectives of the present work is to implement a more severe thermal history in order to observe a more significant tube response with temperature.

The positive bending moment associated with the circumferential stress distribution induced by the manufacturing process with the cold mandrel in the $[0^\circ]_6$ tube leads to the tube opening (Figure (5.8e)). In this particular case, in the circumferential direction where the effect of the geometry and the anisotropy is negligible, the effect of the temperature gradients induced by the cold mandrel thermal history is predominant and causes the inner portion of the tube to be under compression and the outer portion of the tube to be under tension (in Figure (5.6a)). The hot mandrel $[0^\circ]_6$ tube presents almost null bending moment, because the temperature gradients induced by the hot mandrel manufacturing process are negligible compared to the temperature gradients induced by the cold mandrel manufacturing process.

To summarize the effects of the factors considered on the opening

and closing of the simulated tubes, we can say that:

- the combined effect of anisotropy and geometry is to close the tube, as we have seen for the $[90°]_6$, $[\pm 85°]_3$ and $[\pm 55°]_3$ tubes;
- the viscoelastic behavior and the mandrel boundary condition tend to intensify the effect of geometry and anisotropy through strains adaptation in the viscous phase, as we have seen for the $[90°]_6$ and $[\pm 85°]_3$ tubes (see Figure (5.4a) and Figure (5.5a));
- the effect of strong thermal gradients, due to viscoelasticity, tend to open the tube, as seen for the $[0°]_6$ tube (see Figure (5.6a) and Table (5.2)). In the case of $[\pm 55°]_3$ tube, this effect is not clearly visible, but it can be seen that the tube simulated with cold mandrel tends to close slightly less than the tube simulated with hot mandrel (see Table (5.2));
- the stacking sequence explains the tube twisting, as seen for the $[\pm 85°]_3$ and $[\pm 55°]_3$ tubes. In particular, considering also the viscoelastic behavior, the relaxation of the shear stresses as well as the circumferential ones is shown (see Figure (5.5d) for the $[\pm 85°]_3$ tube and Figure (5.7a) and Figure (5.7d) for the shear and circumferential stresses for the $[\pm 55°]_3$ tube respectively).

5.3.1 . Comparison of numerical and experimental results

CETIM manufactured $[\pm 85°]_3$ and $[\pm 55°]_3$ Carbon/PEEK tubes with the LATP technique using the cold and hot mandrel, as explained in Chapter 2). These tubes are the same as the ones simulated in this Chapter.

The numerical and experimental measures of the circumferential relative displacements and the twist offsets are reported in Table (5.3) for each tube and for each manufacturing process.

Table 5.3: Experimental and numerical results for the $[\pm 85°]_3$ and $[\pm 55°]_3$ tubes manufactured with hot and cold mandrel: circumferential relative displacement and twist offset.

Tube	Mandrel	Num. circ. rel. disp. [mm]	Exp. circ. rel. disp. [mm]	Num. twist offset [mm]	Exp. twist offset [mm]
$[\pm 85°]_3$	Hot	-1.877	-2.70	0.734	1.35
$[\pm 85°]_3$	Cold	-2.324	-2.86	0.770	0.21
$[\pm 55°]_3$	Hot	-1.249	-0.95	1.289	2.93
$[\pm 55°]_3$	Cold	-1.162	1.81	1.276	1.50

From the Table (5.3), the tubes simulated behave qualitatively like the CETIM tubes, except for the $[\pm 55°]_3$ tube manufactured with the cold mandrel, for which an opening displacement was observed in the experimental case.

The modeling tools develped in this work are able to qualitatively predict the closure and the twist of the manufactured tubes with both cold and hot mandrel. In order to result in the opening of the $[\pm 55°]_3$ tube, the thermal history of the cold mandrel tube needs to overcome the effect of the geometry and the transverse isotropy in the circumferential direction. The cold mandrel thermal history implemented in the UTEMP (in Figure (5.2) top, derived based on the discussion made in Chapter 4), involves significant heating of the underlying layers in the substrate as well. Indeed, in the thermal history presented in Figure (5.2) top for the cold mandrel, the heat penetrates very deeply in the laminate, and at least three layers are re-heated above the glass transition temperature during the consolidation phase of a given ply. This is typically true when the fibers are homogeneously distributed in the cross-section of the composite tape, since they are primarily responsible for heat conduction through the thickness of the structure. On the other hand, a completely different thermal history could occur if the fibers are not homogeneously distributed in the cross-section of the composite tape and the tape surfaces are richer in polymeric matrix, which is a very poor heat conductor. In this scenario, the LATP heating phase would be much more localized and the heat conduction through the structure thickness, in the consolidation phase, would be obstructed, leading to a higher temperature gradients. The modeling of such thermal history means the introduction of a heterogeneous heat conduction profile through the thickness, for instance including thermal contact resistances between layers. This would lead to a much more complex thermal model, which requires a numerical resolution. One could imagine to simulate an extreme artificial thermal history by means of the UTEMP, in which only the layer that has to be placed is involved by the cooling during the consolidation process, while the other layers of the substrate remain at constant temperature, generating a strong thermal gradient. Moreover, in this way each layer of the structure will have experienced only one thermal history at the end of the fabrication process.

The correct prediction of the tubes responses trends is the most important result of the present work.

The experimental measurements of the tubes twist offset show a strong dependence from the manufacturing process with hot and cold mandrel (which is not highlighted in the numerical results presented).

The numerical results of the twist offsets, and also the shear stresses distributions (as shown in Figure (5.5d) and (5.7d)), are almost unaffected by the thermal history induced by the manufacturing process. The different experimental twist offsets shown by the tubes manufactured with hot and cold mandrels could be related to the crystallization kinetics of the polymeric matrix, which was not addressed in the present work. The PEEK matrix, for example, crystallizes when the temperature is higher than the glass transition temperature, generating an hydrostatic shrinkage that can be model in the same fashion as the thermal strain presented in Chapter 3 in Equation (3.50). The crystallization shrinkage can explain, for instance, the difference between the experimental and numerical twist offset results, especially for the tubes manufactured with a hot mandrel LATP. The crystallization rate is deeply affected by the thermal history of the manufacturing process, which could induce strong and complex crystallization gradients within the structure, leading to a different tube response (Tierney and Gillespie, 2004). The hydrostatic shrinkage by crystallization would also increase the combined effect of the geometry and anisotropy, leading to a more significant closure for the $[\pm 85°]_3$ tube.

The $[\pm 55°]_3$ tube manufactured with a hot mandrel closes after the axial cut, and the numerical results in the circumferential direction are in good agreement with the experimental results. On the other hand, the $[\pm 55°]_3$ tube manufactured with cold mandrel opens instead of closing, showing how the temperature gradients induced during the manufacturing process are so severe as to change completely the tube responses. The numerical simulation does not predict the opening of the cold mandrel $[\pm 55°]_3$ tube, nevertheless the cold mandrel $[\pm 55°]_3$ tube closes less than the hot mandrel $[\pm 55°]_3$ tube, suggesting that the temperature gradients associated to the cold mandrel thermal history tend to open the tube. The cold mandrel thermal history trend to open the tube is clearly visible in the cold mandrel $[0°]_6$ tube, where the circumferential stress distribution depicted in Figure (5.6a) generates a positive bending moment (Table (5.1)).

5.4 . Conclusions and perspectives

In this chapter, thermo-mechanical simulations of cold and hot mandrel manufacturing processes were performed in Abaqus on several tubes. The thermal histories induced by the two manufacturing processes were derived following the considerations made in Chapter 4 and implemented in a users-subroutine UTEMP. In particular, the cold mandrel LATP thermal history is characterized by higher temperature

gradients with respect to the hot mandrel one. At the end of the placement process and after mandrel removal, an axial cutting of the tubes was simulated.

The circumferential, the radial and the axial stresses were assessed for the $[90°]_6$, $[\pm 85°]_3$, $[\pm 55°]_3$ and $[0°]_6$ tubes, while shear stresses were found (as expected) only for $[\pm 85°]_3$ and $[\pm 55°]_3$ tubes. The bending moments associated to the circumferential stresses distributions were determined. A negative bending moment was obtained for every tube simulated except for the $[0°]_6$ cold mandrel tube, where a positive bending moment was obtained. In particular, for the $[90°]_6$ and $[\pm 85°]_3$ tubes simulated with the cold mandrel, the resultant bending moment was found higher with respect to the hot mandrel simulations. This was attributed to the role of the mandrel boundary condition, which was removed at different temperatures in the hot mandrel and cold mandrel simulations. The opposite scenario was found for the $[\pm 55°]_3$ tube, where the higher bending moment comes from the simulation with the hot mandrel. This suggests that the severe temperature gradients associated to the cold mandrel thermal history tend to have an opposite effect compared to the combined effect of the geometry and the transverse isotropy. The opposite trend of the temperature gradients in terms of bending moment was confirmed by the positive bending moment assessed in the $[0°]_6$ cold mandrel tube simulation.

The bending moment represents a constraint reaction due to the material continuity in the circumferential direction of the tube. Cutting the tube along the axial direction, the geometrical constraint is released and residual strains appear. Residual strains results in the tube closing or opening, and in a twist when shear stresses distributions are presents within the structure. In particular, a negative bending moment means that the tube is closing. After the placement process and the mandrel removal, an axial cut was simulated for each of the tubes and the residual strains were assessed. Comparing the experimental and numerical residual strains, a good qualitative agreement was found, except for the $[\pm 55°]_3$ tube manufactured with cold mandrel, which opens in the experiment while it closes in the simulation.

The experimental twist offsets are strongly stacking sequences dependent and temperature gradients dependent. The numerical twist offsets, on the other hand, seem to be affected only by the stacking sequences, since the hot and cold mandrel thermal histories give almost the same twist offsets. The effects of the thermal gradients on the shear stresses distributions are negligible, since the deviatoric response of the matrix can relax completely in the viscous domain, as discussed in Chapter 3. The missing element which is highly affected

by the thermal gradients, not modelled in the present work, is the crystallization kinetics of the polymeric matrix which generates, for temperatures higher than the glass-transition temperature, an hydrostatic matrix shrinkage in addition to the existing thermal strain.

The circumferential direction of the $[\pm 85°]_3$ tube is dominated by the elastic behavior of the fibers. The difference in the amplitude of the tube closure between experimental and numerical results could be due to the crystallization matrix shrinkage which, in this scenario, would increase the tube closing.

The experimental observations show that the $[\pm 55°]_3$ tube closes, for the tube manufactured by hot mandrel, and opens, for the tube manufactured with cold mandrel. In this scenario, the temperature gradients induced by the cold mandrel thermal history change completely the tube responses. The numerical observations for both $[\pm 55°]_3$ hot and cold mandrel tubes show that both tubes close, even if the $[\pm 55°]_3$ cold mandrel tube closes less than the hot mandrel tube, as evidence of the fact that the temperature gradients induced by the cold mandrel thermal history tend to open the tube.

The temperature gradients effects are clearly visible for the $[0°]_6$ cold mandrel tube simulated which, after the axial cut, opens instead of closing (see Figure (5.8e) right).

To improve the prediction of the initial state of a composite structure manufactured by the LATP manufacturing process, the perspectives of this work are the following:

- based on the mechanical framework introduced in Chapter 3, the development of a constitutive model that accounts for viscoelastic relaxation also in the hydrostatic stress relative to the transverse isotropic plane, which would accentuate the effect of strong thermal gradients on tube opening;
- implementation of a thermal history characterized by more severe thermal gradients;
- the modeling of crystallization shrinkage based on the mechanical framework introduced in Chapter 3, which would increase the circumferential and shear stresses hence the closure and twist of the tubes.

Conclusions and perspectives

The goal of the present thesis work was to model and simulate the initial state of a thermoplastic matrix composite structure manufactured by the Laser Assisted Tape Placement.

This issue is extremely important, especially because composite materials are widely used in the aerospace and automotive industries with a view to reducing the weight of structures and thus reducing carbon-dioxide emissions, as pointed out in the Introduction.

In Chapter 1, a state of the art was presented in order to highlight the possible sources of residual stresses and strains at different scales and in relation with the phenomena involved in the LATP manufacturing process. Generally, residual stresses develop in order to accommodate incompatible strains of different origins (for example, thermal dilatation/contraction) and are associated to different types of constraints within the structure. Due to the complexity of the LATP technique and the numerous sources of residual stresses and strains involved, the present work focused on the evaluation of the main physical mechanisms at the meso- and the macro-scale underlying the build-up of the initial state within the composite structure caused by the manufacturing process. The following Chapters evaluate the effects of each mechanism addressed.

The mechanism present only at the macro-scale is the geometry and the anisotropy of the composite part, and it was addressed first (in Chapter 2). An unconstrained composite circular section tube with the fibers oriented along the circumferential direction subjected to a uniform cooling process shows residual thermal stresses. Indeed, the curved geometry couples the radial direction, which is dominated by the matrix behavior, with the circumferential direction, which is dominated by the fibers behavior: an incompatible thermal strains field is thus generated, which causes residual thermal stresses within the tube. This effect was also evaluated in Chapter 2 with an analytical structural model in 1D.

In Chapter 3, a temperature-dependent visco-elastic constitutive model was developed in order to take into account the stresses relaxation with temperature during the manufacturing process. Of the two constituents of the composite, fibers and matrix, only the second displays a viscoelastic response in the considered temperature range, resulting in a complex viscoelastic behavior of the composite. A particular decomposition for the stress and strain tensors was proposed in order to highlight the contributions of fibers and matrix on the consti-

tutive behavior of the composite material at the meso-scale. The decomposition leads to uncoupled material parameters, and the linear viscoelasticity was introduced through the generalized Maxwell model only on the material parameters strongly affected by the deviatoric response of the matrix. The stresses relaxation with temperature was introduced by the Williams Landel and Ferry law in order to take into account the effects of high temperature gradients induced by the LATP manufacturing process.

The localized laser heating during LATP induces high thermal gradients, which can in turn generate residual stresses and strains. The three-dimensional temperature field induced by the LATP would require modeling the trajectory that the LATP machine needs to follow in the tape placement process, which would be too expensive in terms of computational time. However, high temperature gradients occur mainly through the thickness of the structure. Assuming a null initial state for the incoming layer, a one-dimensional heat transient transfer model was used to describe the temperature history induced by the consolidation phase of the LATP, and its analytical solution was presented in Chapter 4. Mixed boundary conditions were used in order to take into account the thermal effects of the mandrel (considered as a heat sink) and the ambient. The initial condition of the present thermal model corresponds to the initial temperature distribution induced by the laser in the LATP heating phase, which was not modelled in Chapter 4. Therefore, a literature research on the LATP heating phase models was carried out in order to derive the initial condition to be used in the analytical thermal model. Considerations were made in Chapter 4, where the thermal history of the whole LATP manufacturing process was proposed.

The temperature-dependent visco-elastic constitutive model presented in Chapter 3 and the analytical thermal model proposed in Chapter 4 were implemented in users-subroutines respectively UMAT and UTEMP to perform thermo-mechanical structural simulations on Abaqus.

The LATP manufacturing processes with both cold and hot mandrel were simulated in Chapter 5 on different tubes in order to assess the residual stresses induced in the manufactured structure. A cut along the axial direction of the tube was simulated to release the residual stresses generated by the LATP and to assess the geometrical distortions induced. The numerical displacements were compared with the experimental measurements provided by CETIM. It is important to note that the elements developed in this work are based on the physical mechanisms underlying each phenomenon. In particular, the viscoelastic model for the composite was developed supposing that the

polymer matrix relaxes stresses mainly in the deviatoric part. Similarly, the thermal model developed to describe the thermal history of LATP was constructed taking into account the numerical and experimental results in the literature. In addition, all the material parameters used for the carbon/PEEK composite were also taken from the literature. No adjustment of the modeling hypotheses or on the mechanical and thermal material parameters were made to achieve the numerical results discussed here.

The simulations were capable to predict the closure and the twist of the tubes, in qualitative agreement with the experimental results, except for the $[\pm 55^\circ]_3$ tube manufactured with cold mandrel, whose opening was not predicted by the simulations. The $[\pm 55^\circ]_3$ tube in the circumferential direction is affected by the effects of the high temperature gradients induced by the manufacturing process, which change completely the tube response. The lack of agreement between the experimental and the numerical results in this case may be related to the simulated thermal history, which may not be severe enough to highlight the change in response, or to the lack of modeling of other effects, such as the effect of the crystallisation shrinkage.

The first perspective of this thesis work is to further investigate the LATP thermal history. By acting, for example, directly on the initial condition of the thermal model presented in Chapter 4 the temperature at the interface can be raised, thus simulating a more localized heating. Another way to exacerbate the thermal history is to introduce thermal contact resistances between composite layers to the one-dimensional thermal problem. In this scenario, the thermal model would need to be solved numerically.

As we saw in Chapter 3 through the analytical homogenization in Section 3.3, the shear modulus of the matrix affects not only the shear moduli of the composite but also, to a lesser extent, the hydrostatic part related to the transverse isotropic plane. Therefore, another perspective of the present work is to introduce the viscoelastic relaxation also on the hydrostatic stress of the transverse isotropic plane. This could lead to a different tube response with thermal gradients.

The kinetics of crystallization of the polymer matrix is another important aspect that was not addressed in the present work. High temperature gradients induce crystallization gradients that could affect the response of the fabricated structure. The mechanical framework introduced in Chapter 3 is well suited to include the crystallization shrinkage of the matrix. Therefore, another perspective of this work is to model the crystallization kinetics under highly non-isothermal conditions. These topics were addressed by another doctoral thesis car-

ried out by Anna-Maria El Bayssary of Nantes Université. Indeed, the two theses are a part of the work carried out by the research group within the joint laboratory, "Comp' Innov", between CETIM, École Normale Supérieure Paris-Saclay, Nantes Université and the CNRS. The results obtained by Anna Maria in her work underline the importance of the modeling of crystallization kinetics for the prediction of residual stresses and deformations.

A - Proof of modes orthogonality for the one-dimensional thermal model

The details of the proof of orthogonality of the modes $X_m(z)$ for the solution of the one-dimensional thermal model of Chapter 4 are given here.

The model equations are recalled here:

$$\frac{\partial w(z,t)}{\partial t} = k\frac{\partial^2 w(z,t)}{\partial z^2}, \qquad 0 < z < l \tag{A.1a}$$

$$-\frac{\partial w(0,t)}{\partial z} + H_1 w(0,t) = 0, \qquad z = 0 \tag{A.1b}$$

$$\frac{\partial w(l,t)}{\partial z} + H_2 w(l,t) = 0, \qquad z = l \tag{A.1c}$$

$$w(z,0) = f(z) - u(z), \qquad t = 0, \qquad 0 < z < l, \tag{A.1d}$$

as well as the separate variables form of the solution, already accounting for the boundary condition Equation (A.1b):

$$w(z,t) = \sum_{n=1}^{\infty} w_n^z(z) w_n^t(t) = \sum_{n=1}^{\infty} A_n e^{-k\alpha_n^2 t}\left(\cos(\alpha_n z) + \frac{H_1}{\alpha_n}\sin(\alpha_n z)\right) = \\ = \sum_{n=1}^{\infty} A_n e^{-k\alpha_n^2 t} X_n(z). \tag{A.2}$$

We want to prove that

$$\int_0^l X_m X_n dz = 0 \quad \text{for} \quad n \neq m \tag{A.3a}$$

$$\int_0^l X_n^2 dz = \frac{1}{2\alpha_n^2}\left(H_2\left(\frac{\alpha_n^2 + H_1^2}{\alpha_n^2 + H_2^2}\right) + H_1 + \left(\alpha_n^2 + H_1^2\right) l\right) \quad \text{for} \quad n = m, \tag{A.3b}$$

Since it is solution of Equation (A.1a), X_n satisfies the following:

$$X_n = -\frac{1}{\alpha_n^2}\frac{d^2 X_n}{dz^2}. \tag{A.4}$$

Because of the boundary conditions in Equations (A.1b) and (A.1c), we have:

$$\frac{dX_n}{dz} = H_1 X_n \quad \text{at} \quad z = 0, \tag{A.5a}$$

$$\frac{dX_n}{dz} = -H_2 X_n \quad \text{at} \quad z = l \tag{A.5b}$$

In order to prove Equation (A.3a), we introduce:

$$\left(\alpha_m^2 - \alpha_n^2\right) \int_0^l X_m X_n dz = \alpha_m^2 \int_0^l X_m X_n dz - \alpha_n^2 \int_0^l X_m X_n dz. \tag{A.6}$$

From the condition in Equation (A.4) follows:

$$\alpha_m^2 \int_0^l X_m X_n dz - \alpha_n^2 \int_0^l X_m X_n dz = \int_0^l \left(X_m \frac{d^2 X_n}{dz^2} - X_n \frac{d^2 X_m}{dz^2} \right) dz. \tag{A.7}$$

Integrating by parts we obtain:

$$\int_0^l \left(X_m \frac{d^2 X_n}{dz^2} - X_n \frac{d^2 X_m}{dz^2} \right) dz = \left(X_m \frac{dX_n}{dz} - X_n \frac{dX_m}{dz} \right)_{z=0}^{z=l}, \tag{A.8}$$

which is null due to the boundary conditions in Equations (A.5a) and (A.5b). Since $(\alpha_m^2 - \alpha_n^2) \neq 0$ for $n \neq m$, then Equation (A.3a) is proven.

Following similar steps as for the previous case, now we shall prove (A.3b). For $n = m$, we introduce

$$\alpha_n^2 \int_0^l X_n^2 dz \tag{A.9}$$

Applying Equation (A.4) to Equation (A.9) we have:

$$\alpha_n^2 \int_0^l X_n^2 dz = - \int_0^l X_n \frac{d^2 X_n}{dz^2} dz, \tag{A.10}$$

and integrating by parts we obtain:

$$\alpha_n^2 \int_0^l X_n^2 dz = - \int_0^l X_n \frac{d^2 X_n}{dz^2} dz = - \left(X_n \frac{dX_n}{dz} \right)_{z=0}^{z=l} + \int_0^l \left(\frac{dX_n}{dz} \right)^2 dz. \tag{A.11}$$

Applying the boundary conditions in Equation (A.5a) and Equation (A.5b), it follows:

$$\begin{aligned} \alpha_n^2 \int_0^l X_n^2 dz = & - \left(X_n \frac{dX_n}{dz} \right)_{z=0}^{z=l} + \int_0^l \left(\frac{dX_n}{dz} \right)^2 dz = \\ & = H_2 \, X_n^2 \big|_{z=l} + H_1 \, X_n^2 \big|_{z=0} + \int_0^l \left(\frac{dX_n}{dz} \right)^2 dz. \end{aligned} \tag{A.12}$$

Now, recalling the form of $X_n(z)$:

$$X_n(z) = \cos\left(\alpha_n z\right) + \frac{H_1}{\alpha_n} \sin\left(\alpha_n z\right), \tag{A.13}$$

we can also write:

$$\frac{dX_n}{dz} = H_1 \cos(\alpha_n z) - \alpha_n \sin(\alpha_n z) \tag{A.14}$$

From Equations (A.13) and (A.14), it follows that

$$\alpha_n^2 X_n(z)^2 + \left(\frac{dX_n}{dz}\right)^2 = H_1^2 + \alpha_n^2. \tag{A.15}$$

At $z = 0$, from Equation (A.5a) and Equation (A.15), we have:

$$X_n^2 \left(H_1^2 + \alpha_n^2\right) = H_1^2 + \alpha_n^2 \quad \Rightarrow \quad X_n^2 = 1. \tag{A.16}$$

At $z = l$, from Equation (A.5b) and Equation (A.15), we have:

$$X_n^2 = \frac{\alpha_n^2 + H_1^2}{\alpha_n^2 + H_2^2}. \tag{A.17}$$

Furthermore, integrating Equation (A.15) between 0 and l, we obtain:

$$\alpha_n^2 \int_0^l X_n^2 dz + \int_0^l \left(\frac{dX_n}{dz}\right)^2 dz = \left(H_1^2 + \alpha_n^2\right) l. \tag{A.18}$$

Substituting Equations (A.16), (A.17) and (A.18) in (A.12), we obtain

$$\alpha_n^2 \int_0^l X_n^2 dz = H_2 \frac{\alpha_n^2 + H_1^2}{\alpha_n^2 + H_2^2} + H_1 + \left(H_1^2 + \alpha_n^2\right) l - \alpha_n^2 \int_0^l X_n^2 dz, \tag{A.19}$$

it becomes

$$\int_0^l X_n^2 dz = \frac{1}{2\alpha_n^2} \left(H_2 \frac{\alpha_n^2 + H_1^2}{\alpha_n^2 + H_2^2} + H_1 + \left(H_1^2 + \alpha_n^2\right) l \right), \tag{A.20}$$

which proves Equation (A.3b).

Bibliography

ABAQUS/Standard User's Manual, Version 6.11. Dassault Systèmes Simulia Corp, United States, 2011.

Airbus. Composites: Airbus continues to shape the future — Airbus. https://www.airbus.com/en/newsroom/news/2017-08-composites-airbus-continues-to-shape-the-future, 2017. [Online; accessed December-2021].

V. Balbi, T. Shearer, and W. J. Parnell. A modified formulation of quasi-linear viscoelasticity for transversely isotropic materials under finite deformation. *Proc. R. Soc. A.*, 474(2217), 2018. ISSN 23318422.

I. Baran, K. Cinar, N. Ersoy, R. Akkerman, and J. H. Hattel. A Review on the Mechanical Modeling of Composite Manufacturing Processes. *Archives of Computational Methods in Engineering*, 24(2):365–395, 2017. ISSN 18861784. doi: 10.1007/s11831-016-9167-2.

E. J. Barbero, J. N. Reddy, and J. L. Teply. General two-dimensional theory of laminated cylindrical shells. *AIAA Journal*, 28(3):544–553, 1990. ISSN 00011452. doi: 10.2514/3.10426.

J. A. Barnes and G. E. Byerly. The formation of residual stresses in laminated thermoplastic composites. *Composites Science and Technology*, 51(4):479–494, 1994. ISSN 02663538. doi: 10.1016/0266-3538(94)90081-7.

Ben Skuse. The untapped potential in formula 1 composite manufacture — CompositesWorld. https://www.compositesworld.com/articles/the-untapped-potential-in-formula-1-composite-manufacture, 2020. [Online; accessed December-2021].

A. Bertram and J. Olschewski. Anisotropic creep modelling of the single crystal superalloy srr99. *Computational Materials Science*, 5, 1996. doi: 10.1016/0927-0256(95)00053-4. URL http://gen.lib.rus.ec/scimag/index.php?s=10.1016/0927-0256(95)00053-4.

E. P. Beyeler and S. I. Guceri. Thermal analysis of laser- composite tape consolidation. *Journal of Heat Transfer*, 110(May 1988):424–430, 1988.

M. W. Biegler and M. M. Mehrabadi. An energy-based constitutive model for anisotropic solids subject to damage. *Mechanics of Materials*, 19:151–164, 1995.

A. Björnsson, M. Jonsson, and K. Johansen. Automation of composite manufacturing using off-the-shelf solutions, three cases from the aerospace industry. In *Proceedings of the 20th International Conference on Composite Materials :*, 2015.

J.-P. Boehler. *Application of tensor functions in solid mechanics*. CISM Courses and Lectures. Springer-Verlag, Wien, 1987.

F. Campbell. *Structural Composite Materials*. ASM International, nov 2010. ISBN 978-1-62708-314-0. doi: 10.31399/asm.tb.scm.9781627083140. URL https://dl.asminternational.org/handbooks/book/143/Structural-Composite-Materials.

F. C. Campbell. *Manufacturing Processes for Advanced Composites*. Elsevier, 2004. ISBN 9781856174152. doi: 10.1016/B978-1-85617-415-2.X5000-X. URL https://linkinghub.elsevier.com/retrieve/pii/B9781856174152X5000X.

H. S. Carslaw and J. C. Jaeger. *Conduction of Heat in Solids*. Oxford University Press, London, UK, second edi edition, 1959.

P. Casari, F. Jacquemin, and P. Davies. Characterization of residual stresses in wound composite tubes. *Composites Part A: Applied Science and Manufacturing*, 37(2):337–343, 2006. ISSN 1359835X. doi: 10.1016/j.compositesa.2005.03.026.

T. J. Chapman, J. W. Gillespie, R. B. Pipes, J. A. Manson, and J. C. Seferis. Prediction of Process-Induced Residual Stresses in Thermoplastic Composites. *Journal of Composite Materials*, 24(6):616–643, 1990. ISSN 1530793X. doi: 10.1177/002199839002400603.

A. H. Cheng, J. J. Rencis, and Y. Abousleimanc. Generalized plane strain elasticity problems. *Transactions on Modelling and Simulation*, 10, 1995.

F. N. Cogswell. *Thermoplastic aromatic polymer composites: a study of the structure, processing and properties of carbon fibre reinforced polyetheretherketone and related materials*. 1992. doi: 10.1179/095066094790326185.

Collins Aerospace. Advanced structural materials & manufacturing technology — Collins Aerospace. https://www.collinsaerospace.

com/what-we-do/Commercial-Aviation/Aerostructures/Advanced-Structural-Materials, 2020a. [Online; accessed December-2021].

Collins Aerospace. Thermoplastic composites — Collins Aerospace. https://www.collinsaerospace.com/what-we-do/Commercial-Aviation/Aerostructures/Advanced-Structural-Materials/Thermoplastic-Composites, 2020b. [Online; accessed December-2021].

J. Colton and D. Leach. Processing parameters for filament winding thick-section PEEK/carbon fiber composites. *Polymer Composites*, 13 (6):427–434, 1992. ISSN 15480569. doi: 10.1002/pc.750130605.

S. C. Dai and L. Ye. GF/PP tape winding with on-line consolidation. *Journal of Reinforced Plastics and Composites*, 21(1):71–90, 2002. ISSN 07316844. doi: 10.1106/073168402024283.

Y. Dai, M. Feng, and M. Zhao. Topology optimization of laminated composite structures with design-dependent loads. *Composite Structures*, 167:251–261, may 2017. ISSN 02638223. doi: 10.1016/j.compstruct.2017.01.069. URL http://dx.doi.org/10.1016/j.compstruct.2017.01.069https://linkinghub.elsevier.com/retrieve/pii/S0263822316320943.

J. C. de Kruijk. Automated composite manufacturing using robotics lowers cost, lead- time and scrap rate. *Future of Manufacturing for Military Applications*, pages 1–14, 2018. URL https://www.sto.nato.int/publications/STOMeetingProceedings/Forms/MeetingProceedingsDocumentSet/docsethomepage.aspx?ID=43360&FolderCTID=0x0120D5200078F9E87043356C409A0D30823AFA16F602008CF184CAB\7588E468F5E9FA364E05BA5&List=7e2cc123-6186-4c30-8082-1ba0.

B. Desmorat, M. Olive, N. Auffray, R. Desmorat, and B. Kolev. Computation of minimal covariants bases for 2d coupled constitutive laws, 2020.

R. Desmorat and R. Marull. Non-quadratic Kelvin modes based plasticity criteria for anisotropic materials. *International Journal of Plasticity*, 27(3):328–351, 2011. ISSN 07496419. doi: 10.1016/j.ijplas.2010.06.003. URL http://dx.doi.org/10.1016/j.ijplas.2010.06.003.

R. Desmorat, A. Mattiello, and J. Cormier. A tensorial thermodynamic framework to account for the γ' rafting in nickel-based single crystal

superalloys. *International Journal of Plasticity*, 95:43 – 81, 2017. ISSN 0749-6419. doi: https://doi.org/10.1016/j.ijplas.2017.03.010.

L. Di Gennaro, F. Daghia, M. Olive, F. Jacquemin, and D. Espinassou. A new mechanism-based temperature-dependent viscoelastic model for unidirectional polymer matrix composites based on Cartan decomposition. *European Journal of Mechanics, A/Solids*, 90(July):104364, 2021. ISSN 09977538. doi: 10.1016/j.euromechsol.2021.104364. URL https://doi.org/10.1016/j.euromechsol.2021.104364.

A. Dicarlo, P. Podio-Guidugli, and W. O. Williams. Shells with thickness distension. *International Journal of Solids and Structures*, 38(6-7):1201–1225, 2001. ISSN 00207683. doi: 10.1016/S0020-7683(00)00082-2.

S. Dutton, D. Kelly, and A. Baker. *Composite Materials for Aircraft Structures, Second Edition*, volume 43. American Institute of Aeronautics and Astronautics, Reston ,VA, oct 2004. ISBN 978-1-56347-540-5. doi: 10.2514/4.861680. URL https://arc.aiaa.org/doi/book/10.2514/4.861680.

R. F. Eduljee and J. W. Gillespie. Elastic response of post- and in situ consolidated laminated cylinders. *Composites Part A: Applied Science and Manufacturing*, 27(6):437–446, jan 1996. ISSN 1359835X. doi: 10.1016/1359-835X(95)00063-8. URL https://linkinghub.elsevier.com/retrieve/pii/1359835X95000638.

K. Friedrich and A. A. Almajid. Manufacturing Aspects of Advanced Polymer Composites for Automotive Applications. *Applied Composite Materials*, 20(2):107–128, apr 2013. ISSN 0929-189X. doi: 10.1007/s10443-012-9258-7. URL http://link.springer.com/10.1007/s10443-012-9258-7.

W. Fulton and J. Harris. *Representation theory*, volume 129 of *Graduate Texts in Mathematics*. Springer-Verlag, New York, 1991. ISBN 0-387-97527-6; 0-387-97495-4. A first course, Readings in Mathematics.

H. Ghiasi, D. Pasini, and L. Lessard. Optimum stacking sequence design of composite materials Part I: Constant stiffness design. *Composite Structures*, 90(1):1–11, sep 2009. ISSN 02638223. doi: 10.1016/j.compstruct.2009.01.006. URL http://dx.doi.org/10.1016/j.compstruct.2009.01.006https://linkinghub.elsevier.com/retrieve/pii/S026382230900018X.

H. Ghiasi, K. Fayazbakhsh, D. Pasini, and L. Lessard. Optimum stacking sequence design of composite materials Part II: Variable stiffness design. *Composite Structures*, 93(1):1–13, dec 2010.

ISSN 02638223. doi: 10.1016/j.compstruct.2010.06.001. URL http://dx.doi.org/10.1016/j.compstruct.2010.06.001https://linkinghub.elsevier.com/retrieve/pii/S0263822310001947.

Ginger Gardiner. Is the bmw 7 series the future of autocomposites? — CompositesWorld. https://www.compositesworld.com/articles/is-the-bmw-7-series-the-future-of-autocomposites, 2016. [Online; accessed December-2021].

Ginger Gardiner. Automated preforming, part 1: Numbers and landscape — CompositesWorld. https://www.compositesworld.com/articles/automated-preforming-the-numbers-and-landscape, 2017. [Online; accessed December-2021].

Ginger Gardiner. Composites end markets: Pressure vessels (2022) — CompositesWorld. https://www.compositesworld.com/articles/the-markets-pressure-vessels-2022, 2021. [Online; accessed December-2021].

M. Golubitsky, I. Stewart, and D. G. Schaeffer. *Singularities and groups in bifurcation theory. Vol. II*, volume 69 of *Applied Mathematical Sciences*. Springer-Verlag, New York, 1988. ISBN 0-387-96652-8.

Grace Nehls. Ncc's all-composite type v tank demonstrates future composite space tank technology — CompositesWorld. https://www.compositesworld.com/news/nccs-all-composite-type-v-tank-demonstrates-future-\composite-space-tank-technology, 2021. [Online; accessed December-2021].

D. M. Grogan, C. M. Ó Brádaigh, J. P. McGarry, and S. B. Leen. Damage and permeability in tape-laid thermoplastic composite cryogenic tanks. *Composites Part A: Applied Science and Manufacturing*, 78:390–402, 2015. ISSN 1359835X. doi: 10.1016/j.compositesa.2015.08.037. URL http://dx.doi.org/10.1016/j.compositesa.2015.08.037.

W. Grouve. *Weld strength of laser-assisted tape-placed thermoplastic composites*. PhD thesis, University of Twente, 2012. URL http://purl.org/utwente/doi/10.3990/1.9789036533928.

S. M. Grove. Thermal modelling of tape laying with continuous carbon fibre-reinforced thermoplastic. *Composites*, 19(5):367–375, 1988. ISSN 00104361. doi: 10.1016/0010-4361(88)90124-3.

H. Hahn and N. Pagano. Curing Stresses in Composite Laminates. *Journal of Composite Materials*, 9(1):91–106, jan 1975. ISSN 0021-9983. doi: 10.1177/002199837500900110. URL http://journals.sagepub.com/doi/10.1177/002199837500900110.

Hannah Mason. Bmw rolls out multi-material carbon cage with 2022 ix vehicle line — CompositesWorld. https://www.compositesworld.com/articles/bmw-rolls-out-multi-material-carbon-cage-with-2022-ix-vehicle-line, 2021a. [Online; accessed 30-November-2021].

Hannah Mason. Composites end markets: Renewable energy (2022) — CompositesWorld. https://www.compositesworld.com/articles/composites-end-markets-renewable-energy-2022, 2021b. [Online; accessed 30-November-2021].

Z. Hashin. Complex moduli of viscoelastic composites - I. General theroy and application to particulate composites. *International Journal of Solids and Structures*, 6:539–552, 1970a.

Z. Hashin. Complex moduli of viscoelastic composites - II. Fiber reinforced materials. *International Journal of Solids and Structures*, 6:797–807, 1970b.

Z. Hashin and B. W. Rosen. The elastic moduli of fiber-reinforced materials. *Journal of Applied Mechanics*, 31(2):223–232, 1964.

N. Hassan, J. E. Thompson, R. C. Batra, A. B. Hulcher, X. Song, and A. C. Loos. A heat transfer analysis of the fiber placement composite manufacturing process. *Journal of Reinforced Plastics and Composites*, 24 (8):869–888, 2005. ISSN 07316844. doi: 10.1177/0731684405047773.

R. Hill. Theory of mechanical properties of fibre-strengthened materials: I. Elastic behaviour. *Journal of the Mechanics and Physics of Solids*, 12:199–212, 1964.

G. A. Holzapfel and T. C. Gasser. A viscoelastic model for fiber-reinforced composites at finite stains: Continuum basis, computational aspects and applications. *Computer Methods in Applied Mechanics and Engineering*, 190(34):4379–4403, 2001. ISSN 00457825. doi: 10.1016/S0045-7825(00)00323-6.

S. M. Hosseini, I. Baran, M. van Drongelen, and R. Akkerman. On the temperature evolution during continuous laser-assisted tape winding of multiple C/PEEK layers: The effect of roller deformation.

International Journal of Material Forming, 14(2):203–221, 2021. ISSN 19606214. doi: 10.1007/s12289-020-01568-7.

M. W. Hyer. Some Observations on the Cured Shape of Thin Unsymmetric Laminates. *Journal of Composite Materials*, 15(2):175–194, 1981. ISSN 1530793X. doi: 10.1177/002199838101500207.

M. W. Hyer and C. Q. Rousseau. Thermally Induced Stresses and Deformations in Angle-Ply Composite Tubes. *Journal of Composite Materials*, 21(5):454–480, 1987. ISSN 1530793x. doi: 10.1177/002199838702100504.

M. W. Hyer, D. E. Cooper, and D. Cohen. Stresses and deformations in cross-ply composite tubes subjected to a uniform temperature change. *Journal of Thermal Stresses*, 9(2):97–117, 1986. ISSN 1521074X. doi: 10.1080/01495738608961891.

IEA. Net Zero by 2050: A Roadmap for the Global Energy Sector. *International Energy Agency*, page 224, 2021.

F. X. Irisarri, T. Macquart, C. Julien, and D. Espinassou. A novel design method for the fast and cost-effective manufacture of composite parts employing the Quilted Stratum Process. *Composites Part B: Engineering*, 158(September 2018):364–372, 2019. ISSN 13598368. doi: 10.1016/j.compositesb.2018.09.070. URL https://doi.org/10.1016/j.compositesb.2018.09.070.

Jaguar and Land Rover et al. Lighter, faster, further: Jaguar land rover's groundbreaking advanced composites project. https://www.jaguarlandrover.com/news/2021/01/lighter-faster-further-jaguar-land-rovers-groundbreaking\-advanced-composites-project, 2021. [Online; accessed 30-November-2021].

J.C. Simo. On a fully three-dimensional finite-strain viscoelastic damage model: formulation and computational aspects. *Computer Methods in Applied Mechanics and Engineering*, 60:153–173, 1987.

Jeff Sloan. A400m wing assembly: Challenge of integrating composites — CompositesWorld. https://www.compositesworld.com/articles/a400m-wing-assembly-challenge-of-integrating-composites, 2012. [Online; accessed December-2021].

Jeff Sloan. Composites end markets: Aerospace (2022) — CompositesWorld. https://www.compositesworld.com/articles/the-markets-aerospace-2022, 2021a. [Online; accessed 3-December-2021].

Jeff Sloan. Composites end markets: Automotive (2022) — CompositesWorld. https://www.compositesworld.com/articles/composites-end-markets-automotive-2022, 2021b. [Online; accessed 2-December-2021].

G. Jeronimidis and A. Parkyn. Residual Stresses in Carbon Fibre-Thermoplastic Matrix Laminates. *Journal of Composite Materials*, 22(5):401–415, may 1988. ISSN 0021-9983. doi: 10.1177/002199838802200502. URL http://journals.sagepub.com/doi/10.1177/002199838802200502.

Justin Hale. Boeing 787 from the ground up — Boeing. https://www.boeing.com/commercial/aeromagazine/articles/qtr_4_06/article_04_2.html, 2008. [Online; accessed December-2021].

M. Kaliske. A formulation of elasticity and viscoelasticity for fibre reinforced material at small and finite strains. *Computer Methods in Applied Mechanics and Engineering*, 185:225–243, 2000.

M. Kaliske and H. Rothert. Formulation and implementation of three-dimensional viscoelasticity at small and finite strains. *Computational Mechanics*, 19(3):228–239, 1997. ISSN 01787675. doi: 10.1007/s004660050171.

P. Kelly. *Solid Mechanics part I: an introduction to solid mechanics*. University of Auckland, 2013.

T. Kok. *On the consolidation quality in laser assisted fibre placement The role of the heating phase*. PhD thesis, University of Twente, 2018.

R. Lakes. *Viscoelastic Materials*. Cambridge University Press, 2009. ISBN 9780521885683. URL https://books.google.fr/books?id=BH6f2hWWBkAC.

M. Lamontia, S. Funck, M. Gruber, R. Cope, B. Waibel, and N. Gopez. Manufacturing flat and cylindrical laminates and built up structure using automated thermoplastic tape laying, fiber placement, and filament winding. *Sampe Journal*, 39:30–38, 03 2003.

M. V. Lubarda and V. A. Lubarda. A note on the compatibility equations for three-dimensional axisymmetric problems. *Mathematics and Mechanics of Solids*, 25(2):160–165, 2020. ISSN 17413028. doi: 10.1177/1081286519861682.

D. H. Lukaszewicz, C. Ward, and K. D. Potter. The engineering aspects of automated prepreg layup: History, present and future. *Composites Part B: Engineering*, 43(3):997–1009, 2012. ISSN 13598368. doi: 10.1016/j.compositesb.2011.12.003. URL http://dx.doi.org/10.1016/j.compositesb.2011.12.003.

A. Macke, B. F. Schultz, P. K. Rohatgi, and N. Gupta. *Advanced Composite Materials for Automotive Applications*. John Wiley & Sons Ltd, Chichester, UK, oct 2013. ISBN 9781118535288. doi: 10.1002/9781118535288. URL http://doi.wiley.com/10.1002/9781118535288.

P. Mallick. *Fiber-Reinforced Composites: Materials, Manufacturing, and Design, Third Edition*. Mechanical Engineering. Taylor & Francis, 2008. ISBN 9780849342059. URL https://books.google.fr/books?id=kZgkAQAAMAAJ.

J.-A. E. Manson and J. C. Seferis. Process Simulated Laminate (PSL) : A Methodology to Internal Stress Characterization in Advanced Composite Materials. *Journal of Composite Materials*, 26(3):405–431, mar 1992. ISSN 0021-9983. doi: 10.1177/002199839202600305. URL http://journals.sagepub.com/doi/10.1177/002199839202600305.

I. Martin, D. Saenz Del Castillo, A. Fernandez, and A. Güemes. Advanced thermoplastic composite manufacturing by in-situ consolidation: A review. *Journal of Composites Science*, 4(4):1–36, 2020. ISSN 2504477X. doi: 10.3390/jcs4040149.

A. Mattiello, R. Desmorat, and J. Cormier. Rate dependent ductility and damage threshold: Application to nickel-based single crystal cmsx-4. *International Journal of Plasticity*, 10 2018. doi: 10.1016/j.ijplas.2018.09.006. URL http://gen.lib.rus.ec/scimag/index.php?s=10.1016/j.ijplas.2018.09.006.

J. D. D. Melo and D. W. Radford. Elastic Properties of PEEK/IM7 Related to Temperature. *Journal of Reinforced Plastics and Composites*, 22(12):1123–1139, aug 2003. ISSN 0731-6844. doi: 10.1177/0731684403027613. URL http://journals.sagepub.com/doi/10.1177/0731684403027613.

J. Merodio and R. W. Ogden. Mechanical response of fiber-reinforced incompressible non-linearly elastic solids. *International Journal of Non-Linear Mechanics*, 40(2-3):213–227, 2005. ISSN 00207462. doi: 10.1016/j.ijnonlinmec.2004.05.003.

P. Michaleris. Modeling metal deposition in heat transfer analyses of additive manufacturing processes. *Finite Elements in Analysis and Design*, 86:51–60, sep 2014. ISSN 0168874X. doi: 10.1016/j.finel.2014.04.003. URL http://dx.doi.org/10.1016/j.finel.2014.04.003https://linkinghub.elsevier.com/retrieve/pii/S0168874X14000584.

L. Mishnaevsky, K. Branner, H. Petersen, J. Beauson, M. McGugan, and B. Sørensen. Materials for Wind Turbine Blades: An Overview. *Materials*, 10(11):1285, nov 2017. ISSN 1996-1944. doi: 10.3390/ma10111285. URL http://www.mdpi.com/1996-1944/10/11/1285.

J. A. Nairn and P. Zoller. Matrix solidification and the resulting residual thermal stresses in composites. *Journal of Materials Science*, 20(1): 355–367, jan 1985. ISSN 0022-2461. doi: 10.1007/BF00555929. URL http://link.springer.com/10.1007/BF00555929.

B. Nedjar. An anisotropic viscoelastic fibre-matrix model at finite strains: Continuum formulation and computational aspects. *Computer Methods in Applied Mechanics and Engineering*, 196(9-12):1745–1756, 2007. ISSN 00457825. doi: 10.1016/j.cma.2006.09.009.

B. Nedjar. A time dependent model for unidirectional fibre-reinforced composites with viscoelastic matrices. *International Journal of Solids and Structures*, 48:2333–2339, 2011.

M. N. G. Nejhad, R. D. Cope, and S. I. Guceri. Thermal Analysis of in-situ Thermoplastic Composite Tape Laying. *Journal of Thermoplastic Composite Materials*, 4:20–45, 1991.

R. H. Nelson and D. S. Cairns. Prediction of Dimensional Changes in Composite Laminates During Cure. *34th International SAMPE Symposium and Exhibition*, 1989.

L. Nicholson. The role of molecular weight and temperature on the elastic and viscoelastic properties of a glassy thermoplastic polyimide. *International Journal of Fatigue*, 24(2-4):185–195, apr 2002. ISSN 01421123. doi: 10.1016/S0142-1123(01)00072-X. URL https://linkinghub.elsevier.com/retrieve/pii/S014211230100072X.

N. J. Pagano, J. C. Halpin, and J. M. Whitney. Tension Buckling of Anisotropic Cylinders. *Journal of Composite Materials*, 2(2):154–167, 1968. ISSN 07316844. doi: 10.1177/073168449401301101.

N. J. Pagano, N. J. Pagano, J. M. Whitney, and J. M. Whitney. Geometric Design of Composite Cylindrical Characterization Specimens. *Journal of Composite Materials*, 4(3):360–378, 1970. ISSN 1530793X. doi: 10.1177/002199837000400307.

P. P. Parlevliet, H. E. Bersee, and A. Beukers. Residual stresses in thermoplastic composites-A study of the literature-Part I: Formation of residual stresses. *Composites Part A: Applied Science and Manufacturing*, 37(11):1847–1857, 2006. ISSN 1359835X. doi: 10.1016/j.compositesa.2005.12.025.

P. P. Parlevliet, H. E. Bersee, and A. Beukers. Residual stresses in thermoplastic composites—A study of the literature—Part II: Experimental techniques. *Composites Part A: Applied Science and Manufacturing*, 38(3):651–665, mar 2007a. ISSN 1359835X. doi: 10.1016/j.compositesa.2006.07.002. URL https://linkinghub.elsevier.com/retrieve/pii/S1359835X06002223.

P. P. Parlevliet, H. E. Bersee, and A. Beukers. Residual stresses in thermoplastic composites – a study of the literature. Part III: Effects of thermal residual stresses. *Composites Part A: Applied Science and Manufacturing*, 38(6):1581–1596, jun 2007b. ISSN 1359835X. doi: 10.1016/j.compositesa.2006.12.005. URL https://linkinghub.elsevier.com/retrieve/pii/S1359835X07000061.

H. E. Pettermann and A. DeSimone. An anisotropic linear thermo-viscoelastic constitutive law. *Mechanics of Time-Dependent Materials*, 22:4210433, 2018.

R. Pitchumani, S. Ranganathan, R. C. Don, J. W. Gillespie, and M. A. Lamontia. Analysis of transport phenomena governing interfacial bonding and void dynamics during thermoplastic tow-placement. *International Journal of Heat and Mass Transfer*, 39(9):1883–1897, 1996. ISSN 00179310. doi: 10.1016/0017-9310(95)00271-5.

K. R. Rajagopal and A. S. Wineman. Response of anisotropic nonlinearly viscoelastic solids. *Mathematics and Mechanics of Solids*, 14(5):490–501, 2009. ISSN 10812865. doi: 10.1177/1081286507085377.

N. Ranaivomiarana. *Simultaneous optimization of topology and material anisotropy for aeronautic structures*. PhD thesis, Engineering Sciences [physics]. Sorbonne Universite, 2019.

J. N. Reddy. Bending of laminated anisotropic shells by a shear deformable finite element. *Fibre Science and Technology*, 17(1):9–24, 1982. ISSN 00150568. doi: 10.1016/0015-0568(82)90058-6.

J. N. Reddy. *Mechanics of Laminated Composite Plates and Shells Theory and Analysis*. CRC PRESS Boca, second edi edition, 2004. ISBN 0849315921.

M. Schäkel, S. A. Hosseini, H. Janssen, I. Baran, and C. Brecher. Temperature analysis for the laser-assisted tape winding process of multi-layered composite pipes. *Procedia CIRP*, 85: 171–176, 2019. ISSN 22128271. doi: 10.1016/j.procir.2019.09.003. URL https://doi.org/10.1016/j.procir.2019.09.003https://linkinghub.elsevier.com/retrieve/pii/S2212827119312636.

R. Schledjewski. Thermoplastic tape placement process - In situ consolidation is reachable. *Plastics, Rubber and Composites*, 38(9-10):379–386, 2009. ISSN 14658011. doi: 10.1179/146580109X12540995045804.

M. Schlottermüller, H. Lü, Y. Roth, N. Himmel, R. Schledjewski, and P. Mitschang. Thermal Residual Stress Simulation in Thermoplastic Filament Winding Process. *Journal of Thermoplastic Composite Materials*, 16(6):497–519, 2003. ISSN 08927057. doi: 10.1177/089270503035407.

J. C. Simo and T. J. R. Hughes. *Computational Inelasticity*, volume 7 of *Interdisciplinary Applied Mathematics*. Springer-Verlag, New York, 1998. ISBN 0-387-97520-9. doi: 10.1007/b98904. URL http://link.springer.com/10.1007/b98904.

F. O. Sonmez and H. T. Hahn. Modeling of heat transfer and crystallization in thermoplastic composite tape placement process. *Journal of Thermoplastic Composite Materials*, 10(3):198–240, 1997a. ISSN 08927057. doi: 10.1177/089270579701000301.

F. O. Sonmez and H. T. Hahn. Analysis of the on-line consolidation process in thermoplastic composite tape placement. *Journal of Thermoplastic Composite Materials*, 10(6):543–572, 1997b. ISSN 08927057. doi: 10.1177/089270579701000604.

F. O. Sonmez, H. T. Hahn, and M. Akbulut. Analysis of Process-Induced Residual. *Journal of Thermoplastic Composite Materials*, 15(November 2002):525–544, 2002. doi: 10.1106/089270502023207.

J. Sorvari and J. Hämäläinen. Time integration in linear viscoelasticity - a comparative study. *Mechanics of Time-Dependent Materials*, 14:307–328, 2010.

A. J. M. Spencer. *Continuum theory of the mechanics of fibre-reinforced composites*, volume 282 of *CISM Courses and Lectures*, chapter Constitutive theory for strongly anisotropic solids. Springer-Verlag Wien Gmbh, 1984.

C. M. Stokes-Griffin and P. Compston. A combined optical-thermal model for near-infrared laser heating of thermoplastic composites in an automated tape placement process. *Composites Part A: Applied Science and Manufacturing*, 75:104–115, 2015a. ISSN 1359835X. doi: 10.1016/j.compositesa.2014.08.006. URL http://dx.doi.org/10.1016/j.compositesa.2014.08.006.

C. M. Stokes-Griffin and P. Compston. The effect of processing temperature and placement rate on the short beam strength of carbon fibre-PEEK manufactured using a laser tape placement process. *Composites Part A: Applied Science and Manufacturing*, 78:274–283, 2015b. ISSN 1359835X. doi: 10.1016/j.compositesa.2015.08.008. URL http://dx.doi.org/10.1016/j.compositesa.2015.08.008.

C. M. Stokes-Griffin, P. Compston, T. I. Matuszyk, and M. J. Cardew-Hall. Thermal modelling of the laser-assisted thermoplastic tape placement process. *Journal of Thermoplastic Composite Materials*, 28(10): 1445–1462, 2015. ISSN 15307980. doi: 10.1177/0892705713513285.

R. L. Taylor, K. S. Pister, and G. L. Goudreau. Thermomechanical analysis of viscoelastic solids. *International Journal for Numerical Methods in Engineering*, 2:45–59, 1970.

J. Tierney and J. W. Gillespie. Modeling of Heat Transfer and Void Dynamics for the Thermoplastic Composite Tow-placement Process. *Journal of Composite Materials*, 37(19):1745–1768, 2003. ISSN 00219983. doi: 10.1177/002199803035188.

J. J. Tierney and J. W. Gillespie. Crystallization kinetics behavior of PEEK based composites exposed to high heating and cooling rates. *Composites Part A: Applied Science and Manufacturing*, 35(5):547–558, 2004. ISSN 1359835X. doi: 10.1016/j.compositesa.2003.12.004.

Y. M. Toso, P. Ermanni, and D. Poulikakos. Thermal phenomena in fiber-reinforced thermoplastic tape winding process: Computational simulations and experimental validations. *Journal of Com-*

posite Materials, 38(2):107–135, 2004. ISSN 00219983. doi: 10.1177/0021998304038651.

N. Tutuncu and S. J. Winckler. Stresses and deformations in thick-walled cylinders subjected to combined loading and a temperature gradient. *Journal of Reinforced Plastics and Composites*, 12(2):198–209, 1993. ISSN 07316844. doi: 10.1177/073168449301200206.

I. Ward and J. Sweeney. *An Introduction to the Mechanical Properties of Solid Polymers*. Wiley, 2004. ISBN 9780471496267. URL https://books.google.fr/books?id=CjYxgGejjHAC.

T. Weiler, M. Emonts, L. Wollenburg, and H. Janssen. Transient thermal analysis of laser-assisted thermoplastic tape placement at high process speeds by use of analytical solutions. *Journal of Thermoplastic Composite Materials*, 31(3):311–338, 2018. ISSN 15307980. doi: 10.1177/0892705717697780.

J. M. Whitney. On the Use of Shell Theory for Determining Stresses in Composite Cylinders. *Journal of Composite Materials*, 5(July):340–353, 1971.

Williams Advanced Engineering. Fw-evx. https://wae.com/project/fw-evx/, 2021. [Online; accessed 30-November-2021].

W. Zhenye and L. Shiping. The generalized plane strain problem and its application in three-dimensional stress measurement. *International Journal of Rock Mechanics and Mining Sciences and*, 27(1):43–49, 1990. ISSN 01489062. doi: 10.1016/0148-9062(90)90007-O.

M. A. Zocher, S. E. Groves, and D. H. Allen. A three-dimensional finite element formulation for thermoviscoelastic orthotropic media. *International Journal for Numerical Methods in Engineering*, 40:2267–2288, 1997.

université PARIS-SACLAY
ÉCOLE DOCTORALE
Sciences mécaniques et énergétiques, matériaux et géosciences (SMEMAG)

Titre: Modélisation et simulation de l'état initial d'une structure en composite à matrice thermoplastique fabriquée par placement de tape automatisé et consolidation laser

Mots clés: placement de tape automatisé avec consolidation laser, composites à matrice thermoplastique, contraintes résiduelles, modélisation, simulation

Résumé: Au cours des dernières décennies, l'utilisation croissante de matériaux composites dans les industries automobile et aérospatiale a fait appel à des techniques de production modernes et automatisées telles que le placement de bande assisté par laser (LATP), qui assurent des taux de production élevés mais induisent des contraintes et des déformations résiduelles dans les structures fabriquées. En raison de la complexité et des nombreuses sources de contraintes et de déformations résiduelles impliquées dans le processus de fabrication LATP, le présent travail s'est concentré sur l'évaluation des principaux mécanismes physiques à l'échelle méso et macro qui sous-tendent l'accumulation de l'état initial dans la structure composite causée par le processus de fabrication. Selon l'état de l'art, l'effet combiné de la géométrie et de l'anisotropie de la pièce composite est une source importante de contraintes et de déformations résiduelles que l'on retrouve à l'échelle macro. La géométrie courbe couple la cinématique dans le plan avec la cinématique hors du plan tandis que, pour l'anisotropie du composite, le comportement dans le plan est généralement différent par rapport au comportement hors du plan. Par conséquent, le champ de contraintes thermiques incompatibles généré pendant le traitement provoque des contraintes résiduelles au sein de la structure. Pour traiter les effets de l'histoire thermique complexe induite par le LATP pendant la fabrication, un nouveau modèle constitutif viscoélastique dépendant de la température adapté aux composites à matrice polymère renforcés par des fibres unidirectionnelles est développé. Ce modèle est construit à l'échelle du pli isotrope transverse homogénéisé, mais il tient compte des propriétés des constituants sous-jacents. Une décomposition des tenseurs de contrainte et de déformation est proposée, ce qui permet de distinguer plus facilement la contribution des fibres et de la matrice au comportement du matériau composite homogénéisé. En supposant une réponse viscoélastique déviatorique de la matrice et des fibres élastiques, le modèle viscoélastique linéaire est appliqué uniquement sur certains termes de la décomposition. Pour les simulations numériques, le modèle viscoélastique est implémenté dans une sous-routine utilisateur UMAT Abaqus. Une équation transitoire de transfert de chaleur unidimensionnelle est utilisée pour décrire de manière simplifiée l'histoire thermique induite par la phase de consolidation du processus de fabrication du LATP. Les conditions aux limites mixtes considèrent les flux de chaleur avec le mandrin et l'ambiance, tandis que la condition initiale est la distribution de température dans l'épaisseur de la structure générée par la phase de chauffage du LATP. La solution analytique du modèle thermique est développée et implémentée dans une sous-routine utilisateur UTEMP Abaqus. Des simulations thermo-mécaniques sont réalisées sur des tubes à l'aide du logiciel commercial d'éléments finis Abaqus pour évaluer les effets des sources de contraintes et de déformations résiduelles prises en compte dans le présent travail. La technique de modélisation de la fabrication additive est utilisée pour réaliser un modèle simplifié du processus de stratification automatisé du LATP. Dans ce scénario, les contraintes résiduelles sont évaluées et ensuite libérées en simulant une coupe le long de la direction axiale des tubes. Les contraintes résiduelles numériques sont comparées aux résultats expérimentaux fournis par le CETIM.

Title: Modeling and simulation of the initial state of a thermoplastic matrix composite structure manufactured by laser assisted tape placement

Keywords: laser assisted tape placement, residual stresses, thermoplastic matrix composites, modeling, simulation

Abstract: In the last decades, the increasing use of composite materials in the automotive and aerospace industries involved modern and automated production techniques like the Laser Assisted Tape Placement (LATP), which assure high production rates but induce residual stresses and strains in the manufactured structures. Because of the complexities and the numerous sources of residual stresses and strains involved in the LATP manufacturing process, the present work focused on the evaluation of the main physical mechanisms at the meso- and the macro-scale underlying the build-up of the initial state within the composite structure caused by the manufacturing process. From the state of the art, the combined effect of the composite part's geometry and anisotropy is an important source of residual stresses and strains that can be found at the macro-scale. The curved geometry couples the in-plane kinematics with the out-of-plane kinematics while, for the anisotropy of the composite, the in-plane behavior is generally different with respect to the out-of-plane behavior. Therefore, the incompatible thermal strains field generated during processing causes residual stresses within the structure. A new viscoelastic constitutive model suited for unidirectional composite is developed to address the effects of the complex thermal history induced by the LATP. A decomposition of the stress and strain tensors is proposed, making it easier to distinguish the contribution of the fibers and the matrix to the constitutive behavior of the composite material. Assuming a viscoelastic deviatoric response of the matrix and elastic fibers, the linear viscoelastic model is applied only on certain terms of the decomposition. For numerical simulations, the viscoelastic model is implemented in a UMAT Abaqus user subroutine. A one-dimensional heat transfer transient equation is used to describe in a simplified way the thermal history induced by the consolidation phase of the LATP manufacturing process. The mixed boundary conditions consider the heat fluxes with the mandrel and the ambient, while the initial condition is the temperature distribution in the structure thickness generated by the heating phase of the LATP. The analytical solution of the thermal model is developed and implemented in a UTEMP Abaqus user subroutine. Thermo-mechanical simulations are performed on tubes using the commercial finite element software Abaqus to evaluate the effects of the sources of residual stresses and strains accounted in the present work. The additive manufacturing modeling technique is used to achieve a simplified model of the automated layup process of the LATP. In this scenario, residual stresses are assessed and then released by simulating a cut along the axial direction of the tubes. The numerical residual strains are compared with the experimental results provided by CETIM.